DISSERTATION

submitted to the

Combined Faculties of the Natural Sciences and Mathematics

of the Ruperto-Carola-University of Heidelberg. Germany

for the degree of

Doctor of Natural Sciences

Put forward by

Qing Sun

born in Shaanxi, China

Oral examination: 10.12.2019

Investigation of Stability and Reproducibility of Perovskite Solar Cells

Referees:
Prof. Dr. Yana Vaynzof
Prof. Dr. Giulia Grancini

Untersuchung der Stabilität und Reproduzierbarkeit von Perowskit-Solarzellen

Im vergangenen Jahrzehnt konnte die Effizienz von Photovoltaik Bauteilen auf Basis von Bleihalogenoid-Perowskit Materialien erheblich gesteigert werden. Die Stabilität und Reproduzierbarkeit von Perowskit-Solarzellen sind jedoch nach wie vor zwei der größten Herausforderungen und stehen ihrer Einführung als kostengünstige und effiziente Nachfolgegeneration für Photovoltaik Bauteile im Weg. Diese Doktorarbeit zielt darauf ab, diese beiden Aspekte in drei Teilen zu untersuchen. Zunächst veranschaulichen wir die Bedeutung der Mikrostruktur beim Abbau von Methylammonium-Blei-Triiodid-Perowskit-Filmen unter kontrollierter Atmosphäre mit variablem Sauerstoffgehalt und kontinuierlicher Beleuchtung. $CH_3NH_3PbI_3$-Filme mit kleinen, unregelmäßig geformten Kristallkörnern und hoher Defektdichte werden deutlich schneller und stärker abgebaut, als Filme mit großen, gleichmäßig geformten Kristallkörnern und besseren elektronischen Eigenschaften. Im zweiten Teil dieser Arbeit wird gezeigt, dass das Vorhandensein von großflächigen Inhomogenitäten in der chemischen Zusammensetzung sowie den elektronischen Eigenschaften von $CH_3NH_3PbI_3$-Filmen ein häufig auftretendes Problem ist. Des weiteren wird eine Möglichkeit vorgestellt, dieses Problem durch Verbesserung des Herstellungsprozesses zu mindern und eine Perowskitschicht mit einheitlicher Oberflächenzusammensetzung und einheitlichen elektronischen Eigenschaften zu erhalten. Der letzte Abschnitt zielt darauf ab, die Reproduzierbarkeit von Dreifachkationen-Perowskit-Bauteilen ($Cs_{0.05}(MA_{0.17}FA_{0.83})_{0.95}Pb(I_{0.9}Br_{0.1})_3$) durch Optimierung des 'Antisolvent'-Verfahrens zu verbessern. Mit Hilfe von Rasterelektronenmikroskopie und photovoltaischen Messungen wird die Beziehung zwischen Antisolvent-Typ und Tropfgeschwindigkeit ermittelt und deren Effekte auf die Perowskitfilmbildung sowie die Leistungsfähigkeit der Bauteile untersucht.

Investigation of Stability and Reproducibility of Perovskite Solar Cells

Last decade has witnessed a remarkable increase in the efficiency of photovoltaic devices based on lead halide perovskite materials. However, the stability and reproducibility of perovskite solar cells remain two of the biggest challenges impeding their application as the next generation of low-cost and efficient photovoltaics. This thesis aims to investigating these two issues in three parts. First, we reveal the important role of microstructure in the degradation processes of methylammonium lead triiodide perovskite films in controlled oxygen atmospheres under continuous illumination. $CH_3NH_3PbI_3$ films with small, irregular grains and high defect density degrade much faster and more severely than films with large uniform grains and better electronic properties. The second part of this thesis demonstrates that the presence of large-scale chemical compositional and electronic inhomogeneities in $CH_3NH_3PbI_3$ films is a common issue, and suggests one way to mitigate this problem by improving the fabrication process to obtain a perovskite layer with a uniform surface composition and electronic properties. The last section aims to improve the reproducibility of triple cation perovskite ($Cs_{0.05}(MA_{0.17}FA_{0.83})_{0.95}Pb(I_{0.9}Br_{0.1})_3$) devices by optimizing the antisolvent treatment procedure. Scanning electron microscopy and photovoltaic measurements elucidate the relationship between antisolvent type and dripping speed on perovskite film formation and device performance.

Contents

1 Introduction 4

2 Theoretical Background of Hybrid Organic-Inorganic Metal Halide Perovskite Solar Cells 7
- 2.1 Overview . . . 7
- 2.2 Introduction to Solar Cells . . . 7
  - 2.2.1 What is a Solar Cell? . . . 7
  - 2.2.2 The Solar Spectrum . . . 8
  - 2.2.3 Characteristic Performance Parameters . . . 9
  - 2.2.4 External Quantum Efficiency . . . 12
  - 2.2.5 Efficiency Limits . . . 13
- 2.3 Perovskite Solar Cells . . . 15
  - 2.3.1 What is Perovskite? . . . 15
  - 2.3.2 Evolution of Perovskite Solar Cells . . . 15
  - 2.3.3 Material Properties and Compositional Advances . . . 17
  - 2.3.4 Fabrication Methods . . . 20
  - 2.3.5 Device Architecture and Charge Selective Contacts . . . 23
  - 2.3.6 Device Stability and Degradation . . . 26

3 Experimental Methods 29
- 3.1 Overview . . . 29
- 3.2 Film and Device Fabrication . . . 29
  - 3.2.1 Substrates . . . 29
  - 3.2.2 Hole Transport Layers . . . 29
  - 3.2.3 Perovskite Layers . . . 30
  - 3.2.4 Electron Transport Layers . . . 33
  - 3.2.5 Materials . . . 33
- 3.3 Film and Device Characterization . . . 35
  - 3.3.1 Profilometery . . . 35
  - 3.3.2 Atomic Force Microscopy (AFM) . . . 35
  - 3.3.3 Scanning Electron Microscopy (SEM) . . . 36
  - 3.3.4 X-Ray Diffraction (XRD) . . . 37
  - 3.3.5 UV-vis Spectroscopy (UV-vis) . . . 37
  - 3.3.6 Photothermal Deflection Spectroscopy (PDS) . . . 37
  - 3.3.7 Photoemission Spectroscopy . . . 38
  - 3.3.8 XPS and UPS Mapping . . . 40
  - 3.3.9 Photoluminescence Quantum Efficiency (PLQE) . . . 41
  - 3.3.10 Solar Simulator and J-V measurement Setup . . . 42

3.3.11 External Quantum Efficiency (EQE) 43
3.3.12 Environmental Rig 43

4 Oxygen and Light Induced Photodegradation 45
4.1 Overview 45
4.2 Introduction 45
4.3 Degraded Films in Oxygen under Illumination 46
4.3.1 Optical Properties 46
4.3.2 Surface Compositional Properties 48
4.4 Photovoltaic Performance of Degraded films 53
4.5 Discussion—Role of Microstructure 55
4.5.1 Evolution of Microstructure in Degradation 56
4.5.2 Role of Grain Boundaries 57
4.6 Conclusions 58

5 Effects of Large-Scale Compositional and Electronic Inhomogeneities on Device Performance 59
5.1 Overview 59
5.2 Introduction 59
5.3 XPS and UPS Mapping 61
5.3.1 I/Pb Maps 61
5.3.2 IP maps 63
5.3.3 Influence of Storage Conditions 65
5.3.4 Possible Causes for the Surface Inhomogeneities 66
5.4 Effect on Device Performance 67
5.5 Conclusions 68

6 The Relationship between Antisolvent Type and Dripping Speed, Determining the Device Performance 69
6.1 Overview 69
6.2 Introduction 69
6.3 The Relationship between Antisolvent type and Dripping Speed . . . 70
6.3.1 Device Performance 70
6.3.2 Surface Chemical Composition 72
6.3.3 Microstructure 74
6.4 Discussion 76
6.5 Conclusions 81

7 Conclusions and Future Work 82

Appendices 84

Appendix A Figures 85

Appendix B Tables 106

Appendix C Calculate the PbI_2 Amount from SEM Images 112

Appendix D Abbreviations 115

References 117

List of my Publications 135

Acknowledgements 136

1 Introduction

As an important source of renewable energy, solar energy has been harnessed in various ways, one of which is photovoltaics that convert the energy of sunlight into electricity by the photovoltaic effect. The great potential of photovoltaic devices, or solar cells, was foreseen by Werner von Siemens in 1885, commenting on the discovery of the photovoltaic effect: ‘However great the scientific importance of this discovery may be, its practical value will be no less obvious when we reflect that the supply of solar energy is both without limit and without cost, and that it will continue to pour down upon us for countless ages after all the coal deposits of the earth have been exhausted and forgotten.’ [1]

Crystalline silicon solar cells, as the first generation photovoltaic devices, still dominate more than 90 % of the commercial market, despite the long payback period. The second generation is the thin-film solar cell, produced by depositing semiconducting materials (such as gallium arsenide (GaAs), cadmium telluride (CdTe), copper indium gallium diselenide (CIGS) and silicon) on a substrate. The world record of the highest efficient single junction solar cell is held by GaAs thin film solar cells at 29.1 % [2]. The third generation of solar cells (i.e., organic solar cells, dye-sensitized solar cells(DSSCs), perovskite solar cells and quantum dot solar cells), often also described as ‘emerging photovoltaics’, are promising to achieve high efficiency at lower production cost. These materials are still under development, with full commercialization promising in the near future.

Perovskite solar cells originated as dye-sensitized solar cells (DSSCs), and only held an efficiency of 3.8 % when discovered in 2009 [3]. Its efficiency was increased to 9.7 % in 2012 by replacing the liquid with a solid hole transporting material [4]. Almost at the same time, perovskite was shown to be able to transport both electrons and holes, and reached an efficiency of 10.9 % [5]. Since then, the following years witnessed a rapid growth of perovskite photovoltaic studies. The breakthrough of an efficiency exceeding 20 % was achieved by Seok’s group in 2015 [6] employing intramolecular exchange, which was later applied to the fabrication of advantageous mixed cation perovskites [7]. In 2016, Saliba et al. reported a ‘triple cation’ perovskite, yielding an efficiency of 21.1 % and improved stability [8]. As of August 2019, the record efficiency of 25.2 % was reported by the Korean Research Institute of Chemical Technology (KRICT) and Massachusetts Institute of Technology (MIT), certified by the National Renewable Energy Laboratory (NREL) [2].

Despite a decade of research, many problems still remain unsolved. One of the biggest challenge is the poor stability of the perovskite solar cell, which has been reported to degrade under various operating conditions such as moisture, oxygen, light, heat and electrical stress. In addition, large variations in the photovoltaic performance have been reported by different research groups, but the origin is merely discussed. Furthermore, some high-functioning perovskite solar cells are fabricated using an ‘antisolvent’ treatment, but the requirements of a ‘good’ antisolvent that results in a high-quality perovskite film remain unclear, although a wide range of different solvents have been reported to produce good perovskite solar cells. In this thesis, we will investigate these issues.

In Chapter 2, a brief background of perovskite materials and their application in solar cells is presented. First, an introduction to solar cells is given, followed by the characteristic parameters of solar cells and their efficiency limits. In the second section, a brief introduction to perovskite materials and its development in the application of solar cells are briefly reviewed, followed by summaries of the material properties, fabrication methods, selective contacts and the stability issues.

Chapter 3 presents the experimental methods used in this work. The film and device fabrication methods and procedures are described, followed by an explanation of the techniques used for characterizing perovskite films and devices. These techniques are Profilometery, Atomic Force Microscopy (AFM), Scanning Electron Microscopy (SEM), X-ray Diffraction (XRD), UV-vis Spectroscopy (UV-vis), Photothermal Deflection Spectroscopy (PDS), X-Ray Photoemission Spectroscopy (XPS), Ultra-Violet Photoemission Spectroscopy (UPS), XPS and UPS Mapping, Photoluminescence Quantum Efficiency (PLQE) measurements, Solar Cell measurements (current density-voltage (J-V) and External Quantum Efficiency (EQE)) and Enviromental Rig set-up.

Chapter 4 focuses on oxygen-induced degradation of $CH_3NH_3PbI_3$ perovskite films with different microstructures under continuous illumination. We find that the microstructure of perovskite films has a tremendous effect on the oxygen and light induced degradation. Perovskite films with small, irregular grains and high defect density degrade much faster and more severely than films with large uniform grains and better electronic properties.

Chapter 5 presents the large-scale chemical compositional and electronic inhomogeneities of $CH_3NH_3PbI_3$ perovskite films. We demonstrate that these inhomogeneities are not limited to certain fabrication methods, and are commonly observed by other research groups. We find that variations of photovoltaic performance parameters across the entire sample are related to the extent of the observed inhomogeneities, which explains the wide spread of device performance reported in the literature.

Chapter 6 demonstrates the relationship between antisolvent type and dripping speed, and their effects on photovoltaic performance of triple cation perovskite ($Cs_{0.05}(MA_{0.17}FA_{0.83})_{0.95}Pb(I_{0.9}Br_{0.1})_3$) devices. We find that the solubility of organic precursors in the antisolvent has a tremendous effect on the perovskite formation, microstructure, and consequently, the final device performance. Additionally, we present that using certain antisolvents which possess a low solubility of organic precursors is able to improve device reproducibility by widening the dripping speed ‘window’.

Finally, Chapter 7 presents the conclusions of this work and discusses briefly the future directions of research.

2 Theoretical Background of Hybrid Organic-Inorganic Metal Halide Perovskite Solar Cells

2.1 Overview

The first part of this Chapter briefly describes the working principles of a solar cell, followed by an explanation of the characteristic parameters of solar cells. Lastly, the theoretical efficiency limits of a single junction solar cell are described.

In the second part, an introduction to the perovskite material and its development in photovoltaic applications are briefly reviewed. Next, perovskite material properties and advances in the perovskite composition are presented. Following this, fabrication methods of the perovskite film are introduced, together with a short review of device architectures and the selective contacts used in this work. Finally, the device stability is reviewed and two major degradation processes are briefly discussed.

2.2 Introduction to Solar Cells

2.2.1 What is a Solar Cell?

A solar cell is an electrical device that is capable of converting solar energy into electricity by the photovoltaic effect. Firstly, photons of the sunlight are absorbed by the active semiconducting material, generating bound electron-hole pairs (excitons). Next, the electron-hole pairs dissociate to form two separate unbound charge carriers. Lastly, the free electrons and holes are transported and extracted at respective contacts by an external load.

The inorganic semiconductor solar cell is configured as a p-n junction. When an n-type material (i.e., an intrinsic semiconductor doped with an electron donor element) is brought into contact with a p-type material (i.e., an intrinsic semiconductor doped with an electron acceptor element), free electrons diffuse from the n-type material across the junction and recombine with holes on the p-type side. Likewise, holes are also diffused and recombined with electrons on the n-type side. Due to the diffusion of the majority charge carriers (electrons for the n-type material and holes for the p-type semiconductor), a depletion region is formed near the junction interface, with an electric field that counteracts the diffusion (Figure 2.1). If a positive voltage (forward bias) is applied between the two ends of the p-n junction, electrons in

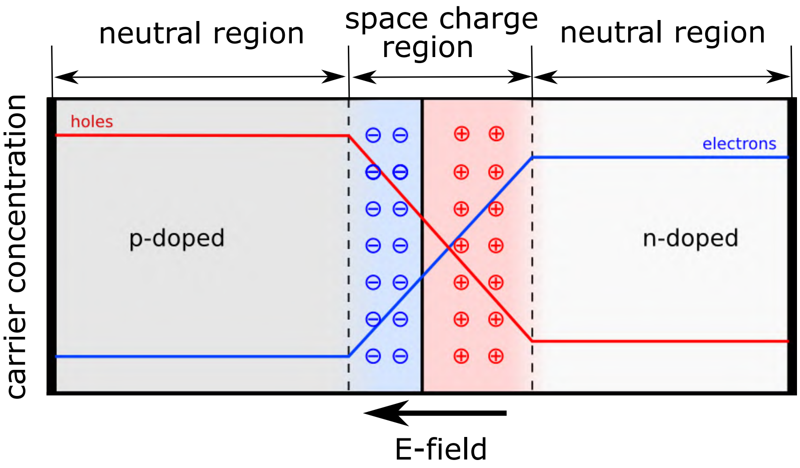

Figure 2.1: Schematic of a p-n junction in equilibrium without an external circuit. Adapted with permission from [9]. Copyright TheNoise, licensed under Creative Commons Attribution-Share Alike 3.0 Unported license.

the n-type region (and holes in the p-type region) are pushed towards the junction, neutralizing the depletion region and further generating a current flow.

Organic semiconductor solar cells usually are constructed in a bulk heterojunction consisting of mixed donor (p-type) and acceptor (n-type) organic materials, in order to facilitate charge separation and compensate the short exciton diffusion length of many organic material systems to improve their device performance.

The most commonly used material for perovskite solar cells is methylammonium lead halide, which has a tunable band gap controlled by the halide content [10, 11], and exhibits an electron-hole diffusion length over one micrometer [12]. The exciton binding energy in this material system has been reported to be low enough [13, 14] that free electrons and holes are present at room temperature. These excellent properties enable the perovskite material to function efficiently as an intrinsic active layer in a thin-film device.

2.2.2 The Solar Spectrum

The total solar irradiation received at the earth's surface depends on the length of light travelling through the atmosphere, which is quantified by air mass (denoted by AM). Air mass is defined as the direct optical length through the earth's atmosphere at a given location, and has value 1 for the normal incidence. To compensate for the variation over seasons, the solar spectrum is standardized by the American Society for Testing and Materials (ASTM). As illustrated in Figure 2.2a, AM 0 spectrum describes the extraterrestrial solar spectral irradiance distribution outside the earth's atmosphere and is given by the ASTM E-490. AM 1.5G spectrum describes the total terrestrial spectral irradiance distribution arriving at the surface of earth after passing through 1.5 times a standard air mass at zenith angle of 48.2°, while AM 1.5D represents only the direct contribution to the total global spectrum. Both

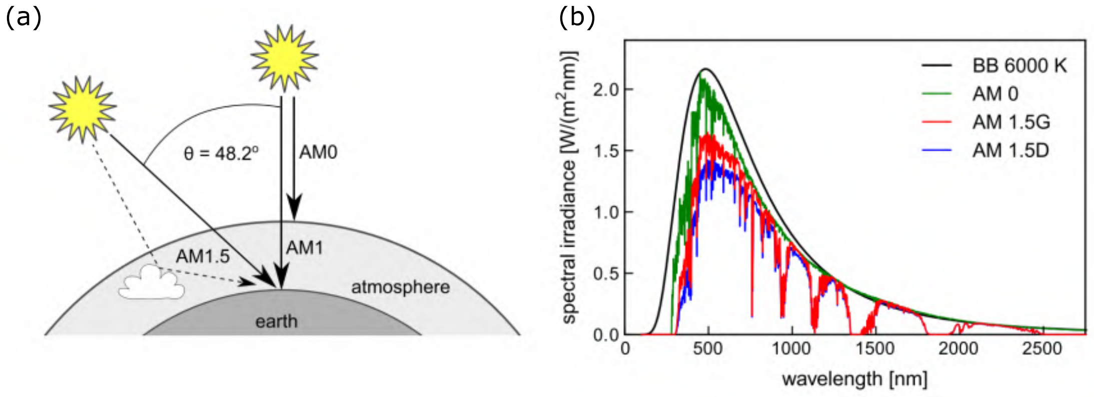

Figure 2.2: (a) Schematic representation of the solar spectral irradiance outside the earth's atmosphere (AM 0), and two terrestrial solar spectral irradiance on the earth's surface (AM 1.5D (the direct normal spectrum, solid arrow) and AM 1.5G (the total global spectrum, solid and dashed arrows)). (b) Spectral irradiance of AM 0, AM 1.5D and AM 1.5G, in comparison to the black body spectrum with a surface temperature of 6000 K used by Shockley and Queisser (BB 6000K). Reproduced with permission form [15]. Copy right 2016 Elsevier Ltd.

spectra are given by the ASTM G-173-03. Figure 2.2b demonstrates the spectra of AM 0, AM 1.5G, AM 1.5D and a black body emission with a surface temperature of 6000 K. The Standard Test Conditions (STC) specifies a standard testing condition of solar cells: under AM 1.5G illumination (with an irradiance of 100 mW/cm^2) at 25 °C.

2.2.3 Characteristic Performance Parameters

The current of a solar cell consists of three components, a dark generation current I_0, a recombination current I_{rec}, and a photocurrent I_{ph}. Divided by the illuminated active area on a solar cell, the current is converted to the current density ($J = I/A$ with A representing the illuminated area). Therefore, the total current density of a solar cell is:

$$J = J_{ph} + J_0 - J_{rec} \tag{2.1}$$

The difference between the dark generation current density and the recombination current density equals the current density injected to a solar cell in the dark, which can be described with the Shockley diode equation [16]:

$$J_{dark} = J_0 - J_{rec} = J_0 \cdot (exp(\frac{qV}{nK_BT}) - 1) \tag{2.2}$$

with the parameter n being the ideality factor, describing the specific exponential voltage dependence of the current.

Figure 2.3 shows a typical current density-voltage (J-V) characteristic of a solar cell (for $V > 0$) with the following expression derived from equation 2.1 and 2.2:

$$J = J_{ph} - J_0 \cdot (exp(\frac{qV}{nK_BT}) - 1) \tag{2.3}$$

Open-circuit and short-circuit are two important operating conditions of a solar cell. The open-circuit voltage (V_{OC}) and the short-circuit current density (J_{SC}) under illumination are described by the expressions derived from equation 2.3:

$$V_{OC} = V(J = 0) = \frac{nK_BT}{q} \cdot ln(\frac{J_{ph}}{J_0} + 1) \tag{2.4}$$

$$J_{SC} = J(V = 0) = J_{ph} \tag{2.5}$$

The electrical power density output of a solar cell is the product of current density and voltage. The maximum power density is achieved at the maximum power point (MPP), with current density J_{MPP} and the voltage V_{MPP}.

The third important parameter is the fill factor (FF), defined as the ratio of the maximum power density at the MPP (dark green rectangle in Figure 2.3) and the theoretical maximum power density (light green rectangle in Figure 2.3), which is the product of V_{OC} and J_{SC}.

$$FF = \frac{J_{MPP} \cdot V_{MPP}}{J_{SC} \cdot V_{OC}} \tag{2.6}$$

The fourth characteristic parameter is the power conversion efficiency (PCE), which describes the maximum efficiency of a solar cell converting the incoming photon energy to the electrical power at the MPP.

$$PCE = \frac{P_{MPP}}{P_{in}} = \frac{FF \cdot J_{SC} \cdot V_{OC}}{I_E^{AM1.5G}} \tag{2.7}$$

with P_{in} being the incoming photon power density, $I_E^{AM1.5G} = 100\,\mathrm{mW/cm^2}$ the integrated power density of AM 1.5G spectrum.

The equivalent circuit of a real solar cell is shown in Figure 2.4a, which consists of a photocurrent source $\mathrm{I_{ph}}$, a series resistance $\mathrm{R_s}$, a shunt resistance $\mathrm{R_{sh}}$ and a diode. The influence of these two resistances on the J-V curve is simulated in Figure 2.4b and c. The series resistance represents the contact resistance between electrodes and adjacent layers, mainly causing the loss in the fill factor. When $\mathrm{R_{sh}} \rightarrow \infty$, FF drops for a larger $\mathrm{R_s}$, whereas $\mathrm{V_{OC}}$ is unaffected. The shunt resistance represents the possible alternative pathways, such as pinholes in the active layer, and is responsible for the low fill factor and $\mathrm{V_{OC}}$ in the solar cell. When $\mathrm{R_s} = 0$, $\mathrm{V_{OC}}$ and FF decrease with $\mathrm{R_{sh}}$, while $\mathrm{J_{SC}}$ remains intact.

Derived from the equation 2.3, the J-V characteristics of a real solar cell can be described as:

$$J = J_{ph} - J_0 \cdot (exp(\frac{q(V + JR_s)}{nK_BT}) - 1) + \frac{V + JR_s}{R_{sh}} \tag{2.8}$$

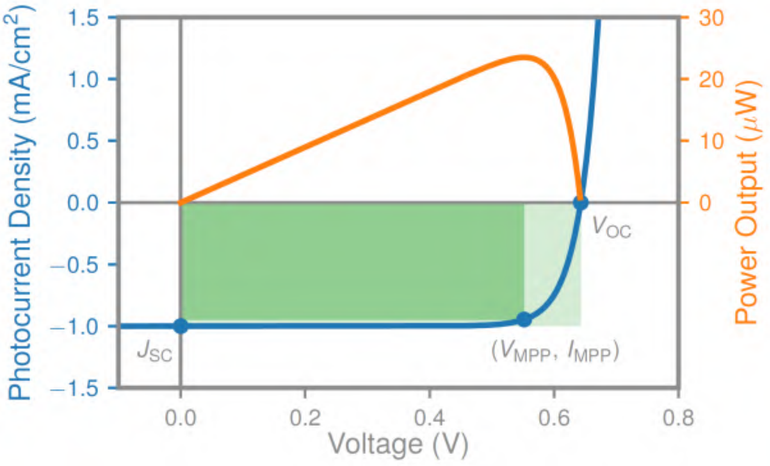

Figure 2.3: A typical J-V curve (blue line) and electrical power output (orange line) of a solar cell. Open-circuit voltage and short-circuit current conditions are denoted. The power is calculated as the product of current and voltage with an illuminated area ($A = 4.5\,\mathrm{mm}^2$), whose maximum occurs at the maximum power point (MPP). Adapted from [17] with permission.

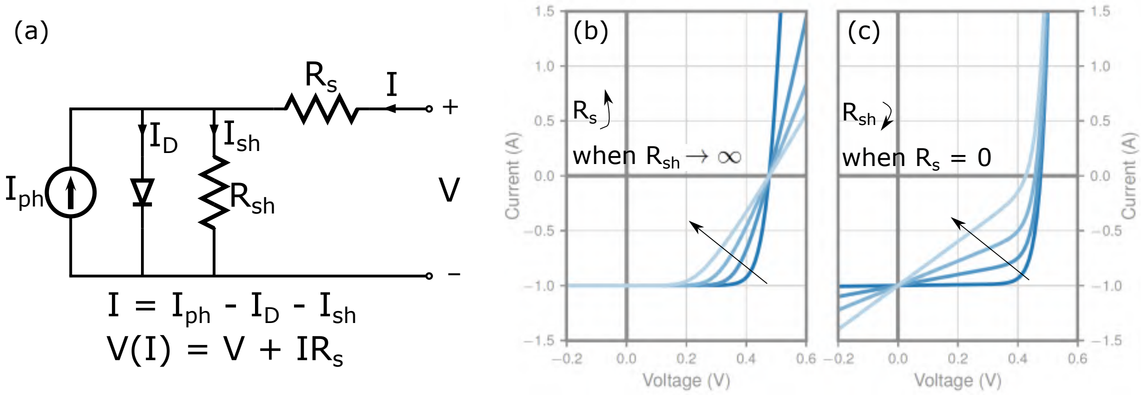

Figure 2.4: (a) An equivalent circuit of a solar cell with a photocurrent source I_{ph}, a diode, a series resistance R_s and a shunt resistance R_{sh}. (b-c) Modelling of the effect of two resistances on the J-V curve. The J-V curve changes from dark to light blue, when (b) R_s increases with $R_{sh} \to \infty$, and (c) R_{sh} decreases with $R_s = 0$. Adapted from [17] with permission.

2.2.4 External Quantum Efficiency

Another important parameter describing the efficiency of a photovoltaic device is the external quantum efficiency (EQE), which is defined as the ratio of the number of extracted charge carriers collected at the electrodes of a solar cell to the number of photons incident on the device:

$$EQE = \frac{\text{\# of extracted charge carriers}}{\text{\# of incident photons}} \tag{2.9}$$

It is obtained by measuring the short-circuit current density under illumination by monochromatic light as a function of wavelength λ:

$$EQE(\lambda) = \frac{J_{SC}(\lambda)/q}{\Phi(\lambda)} = \frac{J_{SC}(\lambda)/q}{P_{in}/E_{ph}(\lambda)} \tag{2.10}$$

where $\Phi(\lambda)$ is the photon flux (numbers of photons per second per m^2) incident on the device at a wavelength λ, $E_{ph}(\lambda) = \frac{hc}{\lambda} = q \cdot \frac{1240}{\lambda_(nm)}$ is the energy of a single photon at a given wavelength λ (with c and h being the velocity of light and plank constant, respectively). Hence, EQE can be written as:

$$EQE(\lambda) = \frac{hc}{q\lambda} \cdot \frac{J_{SC}(\lambda)}{P_{in}} = \frac{1240}{\lambda_(nm)} \cdot \frac{J_{SC}(\lambda)}{P_{in}} \tag{2.11}$$

The spectral response (denoted by SR(λ)) is defined as the ratio of photocurrent generated by a solar cell to the incident light power at a given wavelength:

$$SR(\lambda) = \frac{J_{SC}(\lambda)}{P_{in}} \tag{2.12}$$

It can be described in terms of EQE:

$$SR(\lambda) = \frac{q\lambda}{hc} \cdot EQE(\lambda) = 0.808 \cdot \lambda(\mu m) \cdot EQE(\lambda) \tag{2.13}$$

The theoretical estimated short circuit current is obtained by integrating the product of EQE and photon flux over all relevant wavelength and described as:

$$J_{SC}^{predicted} = q \cdot \int EQE(\lambda) \cdot \Phi_{AM1.5}(\lambda)\, \mathrm{d}\lambda \tag{2.14}$$

with $\Phi_{AM1.5}$ being the photon flux under AM 1.5G spectrum.

If the predicted short-circuit current density $J_{SC}^{predicted}$ derived from the EQE measurement does not match the $\mathrm{J_{SC}}$ obtained by the J-V measurement, the light intensity of the solar simulator should be adjusted to one sun intensity (100 mW/cm^2) according to the spectral mismatch correction factor.

Spectral Mismatch Correction Factor

It is important to note that solar simulators do not produce the exact AM 1.5G spectrum. Therefore, corrections are made with a spectral mismatch factor M to correct for the light intensity differences between lamp spectrum and AM 1.5G at the given wavelengths, in order to standardize the measurements among different labs. It is calculated with four terms [18]:

$$M = \frac{J_{ref}^{AM1.5}}{J_{dev}^{AM1.5}} \cdot \frac{J_{dev}^{Sim}}{J_{ref}^{Sim}} \tag{2.15}$$

where the four short-circuit current densities are calculated by multiplying the spectral response of the device (denoted by dev) and a calibrated reference diode (denoted by ref) with the spectral irradiance of the AM 1.5G (denoted by AM1.5) and the solar simulator (denoted by Sim):

$$J_{ref}^{AM1.5} = \int SR_{ref}(\lambda) \cdot I_{AM1.5}(\lambda)\,\mathrm{d}\lambda \tag{2.16}$$

$$J_{dev}^{AM1.5} = \int SR_{dev}(\lambda) \cdot I_{AM1.5}(\lambda)\,\mathrm{d}\lambda \tag{2.17}$$

$$J_{ref}^{Sim} = \int SR_{ref}(\lambda) \cdot I_{Sim}(\lambda)\,\mathrm{d}\lambda \tag{2.18}$$

$$J_{dev}^{Sim} = \int SR_{dev}(\lambda) \cdot I_{Sim}(\lambda)\,\mathrm{d}\lambda \tag{2.19}$$

Dividing the measured short-circuit current density of the test device by the mismatch factor M, the real $\mathrm{J_{SC}}$ is obtained.

2.2.5 Efficiency Limits

The theoretical maximum power conversion efficiency of a single junction solar cell is known as the Shockley-Queisser limit (SQ limit) or the detailed balance limit, presented in 1961 by William Shockley and Hans-Joachim Queisser, where they used the emission of a black body with a surface temperature of 6000 K as the approximated solar spectrum [21]. Using the standard AM 1.5G spectrum, Ruehle calculated a maximum efficiency of 33.7 % at a band gap of 1.34 eV [15], still referred to as the Shockley-Queisser limit (black curve in Figure 2.5a). Up to now, the highest efficiency for a single junction solar cell is 29.1 %, achieved with the thin film GaAs [2], reaching more than 85 % of its limit (∇ symbol in Figure 2.5a). The record

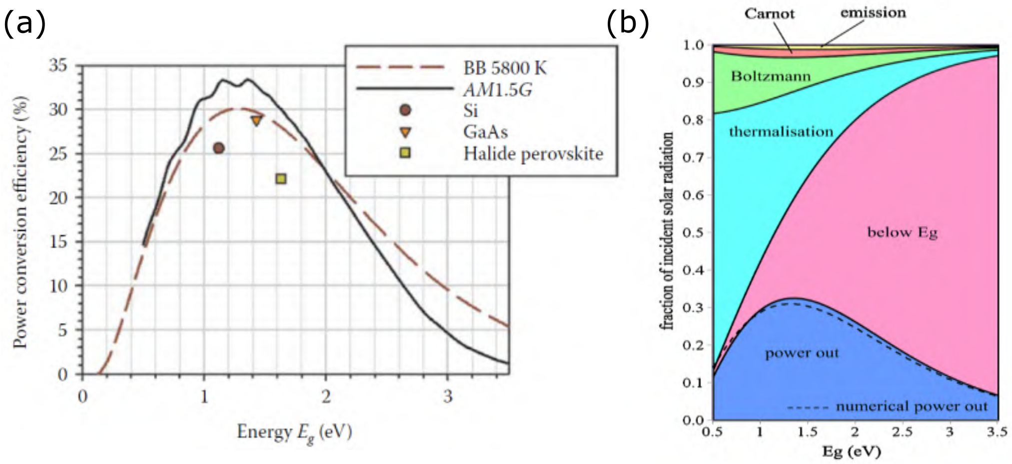

Figure 2.5: (a) The maximum PCE limit for a single junction solar cell operated at 298.15 K and illuminated with the AM 1.5G (solid curve) spectral irradiance and a black body radiation with a surface temperature of 5800 K (dashed curve) as a function of the band gap energy. The denoted points are the efficiency records for Si, GaAs and halide perovskite solar cells in 2018. Adapt with permission from [19] (b) Intrinsic losses of a solar cell. Power out is dependent on the band gap E_g. Adapt from [20] with permission. Copyright 2010 John Wiley & Sons, Ltd.

efficiency of the single junction perovskite solar cell is 25.2 % [2], improved nearly by 3 % since 2018 (□ symbol presented in Figure 2.5a).

Figure 2.5b illustrates five types of intrinsic losses occurring in a single junction solar cell. The non-absorption of photons with energy below the band gap and the emission loss (i.e., absorbers are also emitters according to Kirchhoff's law) limit the maximum current of a solar cell, while the thermalisation (i.e., excited carriers relaxing to the band gap edge), Boltzmann and Carnot losses cause reductions in the maximum voltage [20]. In addition, the calculation of the SQ limit did not take non-radiative recombination into consideration, which also reduces the maximum efficiency [15]. There are two types of non-radiative recombination pathways in semiconductors, namely Auger and Shockley-Read-Hall (SRH) recombination. The latter is also known as trap-assisted recombinations. This occurs when localised energy states (i.e., trap states) are created within the band gap by dopants or defects, where the charge carriers are trapped and then recombine non-radiatively with energy exchanged in the form of lattice vibration. Auger recombination involves a third charge carrier, which is excited to a higher energy level and then losses its excess energy to thermal vibrations after the recombination.

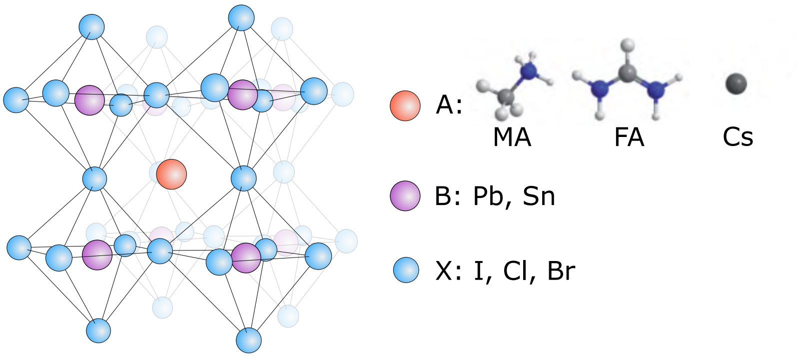

Figure 2.6: Sketch of a cubic ABX_3 perovskite structure. Courtesy of Dr. Alex Taylor. The atomic structures of the A site cations are reproduced with permission from [11]. Copyright 2014, The Royal Society of Chemistry.

2.3 Perovskite Solar Cells

2.3.1 What is Perovskite?

The name 'perovskite' is used to describe any materials with the same crystal structure as calcium titanium oxide ($CaTiO_3$), which is well known as the perovskite structure. It is first discovered by Gustav Rose in 1839 and named after the Russian mineralogist L. A. Perovski. In general, the chemical formula of perovskite material is ABX_3, with A and B being two different cations with different radii, and X an anion bonding to both.

The perovskite material employed in solar cell application is commonly the hybrid organic-inorganic metal halide perovskite, where A is usually an organic cation (such as methylammonium ($CH_3NH_3^+$ or MA^+) and formamidinium ($CH_3(NH_2)_2^+$ or FA^+), B a divalent metal (e.g. Pb^{2+}, Sn^{2+}, etc.), and X a halide anion (i.e., Cl^-, Br^- and I^-) (Figure 2.6). In this work, we focus on two representative types of the organolead halide perovskite. One is the mostly employed $CH_3NH_3PbI_3$ ($MAPbI_3$) perovskite (Chapter 4 and 5), and the other is the 'triple cation' perovskite $Cs_{0.05}(MA_{0.17}FA_{0.83})_{0.95}Pb(I_{0.9}Br_{0.1})_3$ (CsMAFA) (Chapter 6).

2.3.2 Evolution of Perovskite Solar Cells

Miyasaka's group were the first to report the use of organic-inorganic halide perovskite in photovoltaic devices with an efficiency of 3.8 % [3], where an organic electrolyte solution was used as the hole transporting material. Following their work, Park and co-workers doubled the efficiency to 6.5 % in 2011 [23], by optimizing perovskite coating procedure and electrolyte composition. However, the liquid electrolyte was believed to cause stability issues, and therefore, the research focus turned to preparing solid state perovskite-sensitized solar cells.

In 2012, Park, Grätzel and co-workers boosted the efficiency to 9.7 % [4] by introducing Spiro-OMeTAD (2,20,7,70-Tetrakis[N,N-di(4-methoxyphenyl)amino]-9,90-spi-

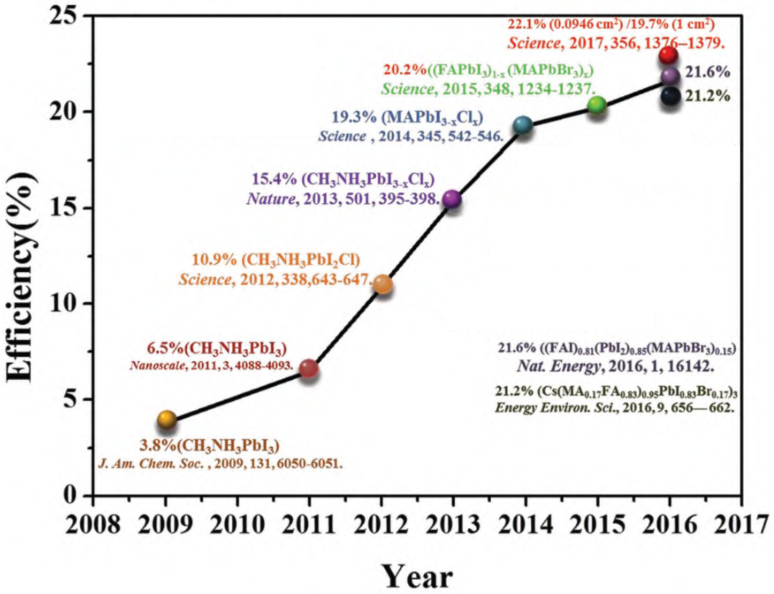

Figure 2.7: Efficiency development of perovskite solar cells from 2008 to 2017. Adapted with permission from [22]. Copyright 2018 John Wiley & Sons, Ltd.

robifluorene) as a solid state hole transporting material, avoiding the problem of dissolving perovskite in the liquid-based solar cells. This is the first prototype of the mesoporous architecture. At about the same time, Snaith and colleagues reported a 10.9 % mixed halide $CH_3NH_3PbI_{3\text{-}x}Cl_x$ device also using Spiro-OMeTAD as the hole transporting material [5]. They replaced the nanoporous TiO_2 with a non-conducting Al_2O_3 scaffold layer, improved the V_{OC} by a few hundred millivolts and boosting the efficiency to over 10 %. This demonstrated that perovskite is able to harvest light and transport both electrons and holes, revealing a border application of perovskite than just as sensitizers in the dye-sensitized solar cells. This study paved the path for a brand new device structure without any metal oxide scaffolds.

In 2013, Snaith's group reported a planar perovskite solar cell via a co-evaporation technique, exhibiting a PCE of 15.4 % [24]. They also managed to achieve a device with 11.4 % PCE by solution deposition in a planar structure [25]. Both studies demonstrated that the mesoporous oxide layer is not necessary.

In the same year, Chen's group for the first time reported a perovskite solar cell in the inverted architecture with a PCE of 3.9 % [26], where PEDOT:PSS (poly (3, 4-ethylenedioxythiopene)-poly (styrenesulfonate)) was used as the hole transporting material at the transparent conductive oxide side and an electron transporting layer was deposited between the perovskite layer and the metal cathode. PCEs of photovoltaic devices employing this architecture were boosted to over 16 % by improving the perovskite film quality [27–29]. So far, three types of perovskite solar cell architectures, namely mesoporous, planar and inverted structures, have been reported.

(Details are described in the Section 2.3.5).

The breakthrough in the PCE exceeding 20 % was achieved by Seok's group in 2015 [6], where $CH(NH_2)_2PbI_3$ ($FAPbI_3$) films were deposited via intramolecular exchange of dimethyl sulfoxide (DMSO) molecules intercalated in PbI_2 with $CH(NH_2)_2I$ (FAI). This methodology was later applied to the fabrication of advantageous mixed cation/mixed halide perovskite $(FAPbI_3)_{0.85}(MAPbBr_3)_{0.85}$ [7]. In 2016, Saliba et al. reported a triple cation perovskite $Cs_{0.05}(MA_{0.17}FA_{0.83})_{0.95}Pb(I_{0.83}Br_{0.17})_3$ by adding 5 % caesium (Cs) to the mixed cation/mixed halide perovskite, yielding a PCE of 21.1 % with improved stability [8]. As of August 2019, the record efficiency of perovskite solar cells is 25.2 %, certified by the National Renewable Energy Laboratory (NREL)[2]. Figure 2.7 summarizes a brief history of the efficiency development of perovskite solar cells from 2008 to 2017 [22].

2.3.3 Material Properties and Compositional Advances

In general, the ABX_3 perovskite structure consists of a 3D BX_6^{4-} octahedral sublattice and A^+ cation filling the empty spaces and balancing the charges. The valence band maximum (VBM) and conduction band minimum (CBM) are determined by the BX_6^{4-} lattice, whereas the A^+ affects the band gap through the lattice expansion or contraction caused by its size variation [30].

The hybrid organic-inorganic metal halide perovskite has a strong optical absorption over the visible spectrum [31], and a tunable band gap from 1.1 eV to 2.3 eV, altered by interchanging the cations [6, 32], metals [33] and halides [10, 11].

$CH_3NH_3PbI_3$ Perovskite

The band gap of $CH_3NH_3PbI_3$ perovskite is around 1.55 eV [34], close to the optimal band gap of a solar cell, which yields a maximum efficiency of 33.7 % at 1.34 eV, estimated by the Shockley-Queisser efficiency limit.

It has been reported that $CH_3NH_3PbI_3$ perovskite has a relatively low exciton binding energy on the order of 16 meV at low temperatures, and even a few millielectronvoltages at room temperature [14, 35, 36], much smaller than the most organic semiconductors. Huang's group has shown the direct evidence for the non-excitonic nature of organolead trihalide perovskite [37], where they measured a giant dielectric constant of over 500 at 20 Hz for $CH_3NH_3PbI_3$. The low exciton binding energy and high dielectric constant enable instant exciton dissociation into free electrons and holes under illumination, and consequently contribute to the excellent photovoltaic performance. The charge carrier diffusion length in $CH_3NH_3PbI_3$ perovskite is at least 100 nm [12, 38] and can be improved to more than 1 μm by increasing Cl content in $CH_3NH_3PbI_{3-x}Cl_x$ [12], which can be attributed to the combination of high charge mobility and low bimolecular recombination [39]. This long diffusion length makes sure that the generated carriers reach the transporting layers before recombination.

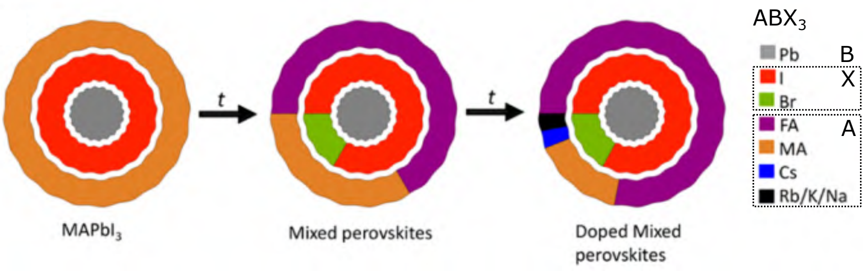

Figure 2.8: Illustration of the compositional trend toward better performing perovskites. Adapted with permission from [41]. Copyright 2018 American Chemical Society.

Mixed Halide Perovskite

The first mixed halide perovskite $CH_3NH_3PbI_{3\text{-}x}Cl_x$ was reported by Snaith's group, where they spin coated a mixture solution of CH_3NH_3I (MAI) and $PbCl_2$ (at a molar ratio of 3:1) [5]. Although the Cl^- substitution is allowed only at low concentrations ($x < 3\text{-}4\,\%$) [40], it increases the charge carriers mobility and diffusion length without changing the material's band gap or optical properties [12, 39, 40], and consequently enhances the photovoltaic performance [5, 12, 40]. In addition, it has shown to improve the environmental stability of the perovskite as well [5].

The incorporation of Br in $CH_3NH_3PbI_3$ changes the band gap dramatically and by the management of Br percentage in $CH_3NH_3Pb(I_{1\text{-}x}Br_x)_3$ ($0 \leq x \leq 1$), one can manipulate the band gap to cover nearly the entire visible spectrum (from 786 nm to 544 nm) [10].

From Single Cation to Mixed Cation

The effective radius of A^+ cation (in the ABX_3) influences perovskite's band gap by expanding or contracting the BX_6^{4-} octahedral cage, rather than determining the band structure [30]. The formability of the 3D perovskite is restricted by the geometric tolerance factor $t = \frac{r_A + r_B}{\sqrt{2}(r_B + r_X)}$ based on the effective ionic radii r_i of A, B and X [42]. Given a particular B and X, in most popular case $APbI_3$, the 'black phase' perovskite is formed for tolerance factors ranging from 0.8 to 1.0; only $MA^+(CH_3NH_3^+)$, $FA^+(CH_3(NH_2)_2^+)$ and Cs^+ meet this condition [43–45].

$MAPbI_3$ was reported to have three structural phases: a cubic phase (α-phase) above 330 K, a tetragonal phase (β-phase) from 160 K to 330 K, and an orthorhombic phase (γ-phase) below 160K [33, 46]. The phase transition from the tetragonal to cubic phase at 330 K (around 56 °C) does not affect the device performance [47]. However, the thermal decomposition of the cubic phase $MAPbI_3$ into PbI_2 at 85 °C (within the range of the operating temperature), even in inert conditions, hampers the long-term device stability [48, 49]. In addition, $MAPbI_3$ was shown to suffer inevitable degradation upon exposure to moisture, oxygen and light [47, 50–58]. (Details are described in the Section 2.3.6).

$FAPbI_3$ exhibits a photoinactive yellow hexagonal phase (δ-phase) at room temperature, and a black polymorph α-phase which requires a higher annealing temperature (150 °C) to form, and is retained after cooling down to room temperature [11]. Unfortunately, this black polymorph phase is unstable especially in an ambient humid atmosphere [33, 59]. Nevertheless, $FAPbI_3$ is a promising candidate to improve the J_{SC}, due to a reduced band bap of 1.48 eV and therefore an extended absorption edge of 840 nm, originating from the longer ionic radius of FA^+ in comparison to MA^+ [11, 59].

$CsPbI_3$, with a band gap of 1.73 eV, forms a photoinactive yellow phase at room temperature and only transforms to the black perovskite phase above 300 °C [60], making it not suitable for photovoltaic applications.

As a result of the environmental or structural instability of the single cation perovskite, numerous attempts have been carried out with mixed cations and halides, in order to achieve a more stable perovskite structure. For example, the undesirable δ-phase in the $FAPbI_3$ can be avoided by using a mixed-cation perovskite system. Pellet et al. [32] stabilized the perovskite crystal structure by substituting MA^+ with FA^+, and prevented the formation of the δ-phase by the dominating effect of MA^+ cation, due to the stronger interaction of MA^+ cation and PbI_6^{4-} octahedral cage [61]. Therefore, this double cation perovskite exhibits a reduced band gap with broader absorption range relative to $MAPbI_3$, and subsequently a boosted J_{SC} [32]. Furthermore, a similar approach with the incorporation of both mixed cations and mixed anions is developed to form $(FAPbI_3)_{0.85}(MAPbBr_3)_{0.15}$, resulting in a highly crystalline and stable perovskite without the formation of the δ-phase [7].

Furthermore, the partial substitution of Cs^+ for FA^+ in the $FAPbI_3$ is found to enhance the light and moisture stability along with photovoltaic performance. This can be attributed to the stabilized perovskite lattice structure by the enhanced FA-I interaction, due to the contraction of the unit cell [62], and also the favourable entropy gain [63]. In addition, Cs has been found to improve the stability of $MAPbI_3$ perovskite [64].

Therefore, Cs is introduced in the $(FAPbI_3)_{0.85}(MAPbBr_3)_{0.15}$ system and a PCE of 21.1 % is achieved by an optimized formulation of the triple cation perovskite $Cs_{0.05}(MA_{0.17}FA_{0.83})_{0.95}Pb(I_{0.83}Br_{0.17})_3$ (abbreviated as CsMAFA) [8]. Saliba et al. reported an improved device stability of this CsMAFA perovskite, retaining 85 % of its initial PCE after 250 hours under illumination operated at the maximum power point. Later, they incorporated the even smaller cation Rb^+ into the CsMAFA system, and found that the 'quadruple cation' perovskite RbCsMAFA exhibits a stabilized PCE of 21.6 % with a V_{OC} of 1.24 V at a band gap of 1.62 eV [65]. Moreover, the choice of A^+ has been further extended. For instance, Park's group reported an inorganic perovskite solar cell with potassium integration into the Cs-based perovskite [66]. Cations with larger radii ($r_i > r_{FA^+}$) were investigated, such as guanidinium (GA^+), which was reported to significantly suppress the nonradiative recombination [67].

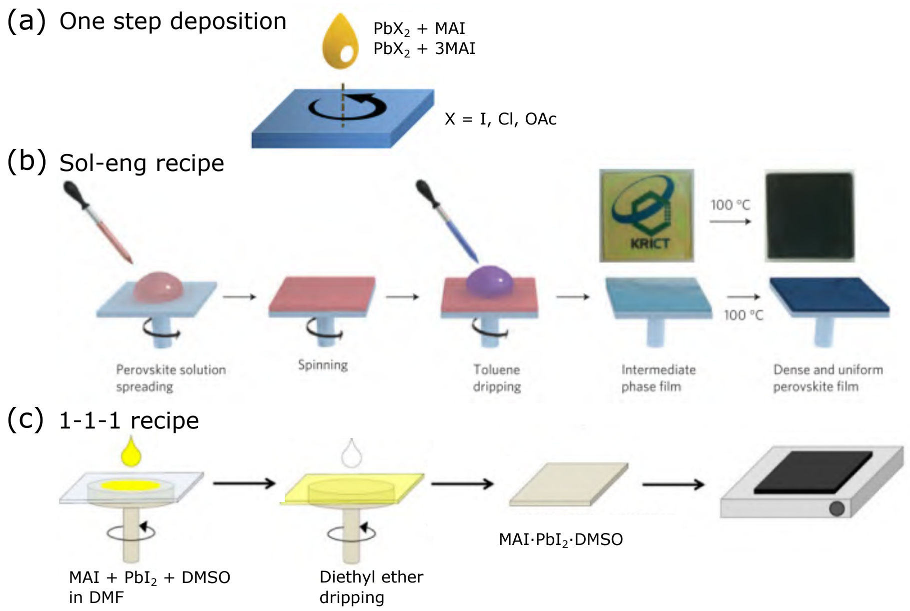

Figure 2.9: Schematic representation of different fabrication methods. (a) One step deposition. Adapted with permission from [73]. Copyright 2016 John Wiley & Sons, Ltd. (b) Sol-eng recipe. Toluene dripping during spin coating the perovskite precursor solution. Reproduced with permission from [74]. Copyright 2014 Macmillan Publishers Limited. (c) 1-1-1 recipe. Diethyl ether dripping during spin coating the perovskite precursor solution (equimolar MAI, PbI_2 and DMSO in DMF). Adapted with permission from [75]. Copyright 2015 American Chemical Society.

2.3.4 Fabrication Methods

Perovskite films can be fabricated by solution processing at low temperatures and also by solution-free processing (e.g. thermal co-evaporation from multiple perovskite precursors [24]). The simplest solution processing method is spin coating, which can be divided into different categories by the choice of perovskite precursors, deposition steps, and whether employing an antisolvent treatment. Other solution processing techniques (e.g. dip-coating [68], blade coating [69], and slot-die coating [70]) and printing techniques (such as ink-jet printing [71]), opens the door for upscaling of perovskite solar cells and modules for commercial application in industry [72].

In this work, we use the spin coating method with a one step recipe, where all the perovskite precursors are mixed together and dissolved in a high boiling point polar solvent (dimethylformamide (DMF), dimethyl sulfoxide (DMSO) or γ-butyrolactone (GBL)), or a mixture of thereof. This precursor solution is spin coated in a single step and the perovskite crystallizes during the thermal annealing process. We also employ the treatment of a droplet of the antisolvent on the wet film during the spin coating process to facilitate the fast formation of a high-quality perovskite film.

One Step Deposition

Early reports on the mesoporous perovskite solar cells were mostly prepared by the one step deposition [4, 5, 76]. However, it results in films with poor morphology when fabricated on planar substrates with a stoichiometric CH_3NH_3I:PbI_2 precursor solution, due to the presence of PbI_2 rod-shaped nanoparticles in the precursor solution. It is actually a colloidal dispersion in a mother solution, rather than a pure solution [77]. Yan et al. also showed that adding excess methylammonium halide reduces the colloidal size and improves the coverage and film morphology [77]. Petrov et al. presented that the CH_3NH_3I:PbI_2 ratio in the precursor solution determines the final perovskite film morphology, which correlates with the crystal shapes of different intermediate phases [78]. PbI_2-rich and stoichiometric solutions form a ribbon-like phase that produces a needle-like crystal shape, while the CH_3NH_3I-rich solution prevents the formation of these needle-like crystals, and hence, improves the final film morphology [78]. As a result, a molar ratio of 3:1 of CH_3NH_3I:PbX_2 ($X = I$, Cl, etc.) is commonly used for the single step deposition and the general reaction process is summarized as [79, 80]:

$$PbX_2 + 3CH_3NH_3I \rightarrow CH_3NH_3PbI_3 + 2CH_3NH_3X \tag{2.20}$$

The excess of organic cation is removed during perovskite formation by sublimation of the volatile by-product salt (i.e., CH_3NH_3X in Equation 2.20) [80, 81]. Therefore, the thermal property of this by-product salt CH_3NH_3X has a great impact on the annealing time and temperature required for perovskite crystallization, and on the film morphology [79, 80, 82].

In 2015, Zhang et al. introduced the non-halide lead source lead acetate trihydrate ($Pb(OAc)_2 \cdot 3H_2O$), which forms the by-product salt $CH_3NH_3(OAc)$ with volatility higher than CH_3NH_3I and CH_3NH_3Cl [82]. The hydration water in the $Pb(OAc)_2 \cdot 3H_2O$ improves the film morphology and subsequently photovoltaic performance due to the reduced nonradiative pathways [82, 83]. The acetate system reduces the activation energy for nucleination and crystal growth [80], resulting in a much faster crystallization and much smoother perovksite films with less pinholes [82]. Zhang et al. also demonstrated that the addition of hypophosphorous acid (HPA) into the perovskite solution assists the formation of high-quality perovskite films with much reduced non-radiative recombination centres, due to the retarding of I_2 back to I^-, which improves the stoichiometry and reduces the metallic lead species in the perovskite film [84]. Hence, this much improved film quality leads to an enhanced photoluminescence intensity and subsequently improved photovoltaic performance [84]. This method is abbreviated as the **$Pb(OAc)_2$ recipe** in the following discussion.

Using Antisolvent

The antisolvent treatment was first introduced by Xiao et al. [85] and Jeon et al. [74] in 2014. During spin coating of the perovskite precursor solution, a droplet of the antisolvent is dripped onto the rotating sample, resulting in a fast formation of the perovskite film upon annealing. Xiao et al. fabricated a uniform perovskite film with full coverage employing a fast deposition crystallization procedure, which introduces a high density of nucleation sites by dripping chlorobenzene during spin coating the perovskite precursor solution dissolved in DMF [85]. Jeon et al. reported a controlled crystallization of dense and uniform perovskite films using an antisolvent treatment during spin coating of perovskite precursors dissolved in a mixed solvent of DMSO and GBL [74] (Figure 2.9b). At the initial stage of spinning, the wet film is composed of CH_3NH_3I and PbI_2 dissolved in DMSO and GBL. With the rapid evaporation of GBL (GBL here works only as a solvent that evaporates faster than DMSO), the film components begin to concentrate. The dripping of an antisolvent (i.e., toluene) immediately removes the excess DMSO solvent and forms an intermediate phase of CH_3NH_3I-PbI_2-DMSO, with DMSO retarding the fast reaction between CH_3NH_3I and PbI_2 during solvent evaporation. After thermal annealing, this intermediate phase converts into a uniform crystalline perovskite film. This technique is denoted by the **sol-eng recipe**.

This method was further developed with a better understanding of the Lewis base adduct formation. Solvents with Lewis base properties such as DMSO donate a pair of free electrons to the Pb^{2+} ion, and form a Lewis adduct-PbI_2(DMSO) complex [86]. Iodide (I^-) in CH_3NH_3I also serves as a donor and forms a Lewis adduct with PbI_2, which explains the increased solubility of PbI_2 in the presence of CH_3NH_3I in DMF. Hence, Ahn et al. proposed a reproducible deposition method employing the Lewis adduct of $CH_3NH_3I{\cdot}PbI_2{\cdot}DMSO$ by spin coating equimolar CH_3NH_3I, PbI_2 and DMSO in DMF [75] (Figure 2.9c). A high-quality perovskite film is converted from this adduct film upon annealing due to the removal of volatile DMSO [86]. They compared different solvents and found diethyl ether to be the best in terms of reproducibility. Toluene and chlorobenzene are miscible with DMSO and will violate the stoichiometry of the $CH_3NH_3I{\cdot}PbI_2{\cdot}DMSO$ adduct, whereas diethyl ether selectively washes away only DMF and therefore forms a well-defined adduct. They also pointed out the importance to keep the stoichiometric ratio of DMSO, because excess DMSO leads to the formation of extra PbI_2 upon exposure to air, and therefore, results in less stable perovskite films. This method is abbreviated as the **1-1-1 recipe**.

Using the PbI_2(DMSO) complex, Yang et al. reported a deposition method to fabricate uniform perovskite films with full coverage by an intramolecular exchange between $CH(NH_2)_2I$ (FAI) and DMSO molecules intercalated in the PbI_2(DMSO) complex, due to the higher affinity of FAI toward PbI_2 relative to DMSO [6]. The smooth morphology of the perovskite film is confirmed by the uniform and dense film of pre-deposited PbI_2(DMSO) complex with unaltered inorganic PbI_2 frame. Later, this methodology is applied to the deposition of mixed cation/mixed halide perovskites, with a breakthrough in PCE of 21.1 % with a triple cation perovskite $Cs_{0.05}(MA_{0.17}FA_{0.83})_{0.95}Pb(I_{0.83}Br_{0.17})_3$, with chlorobenzene used as the antisolvent during spinning [8].

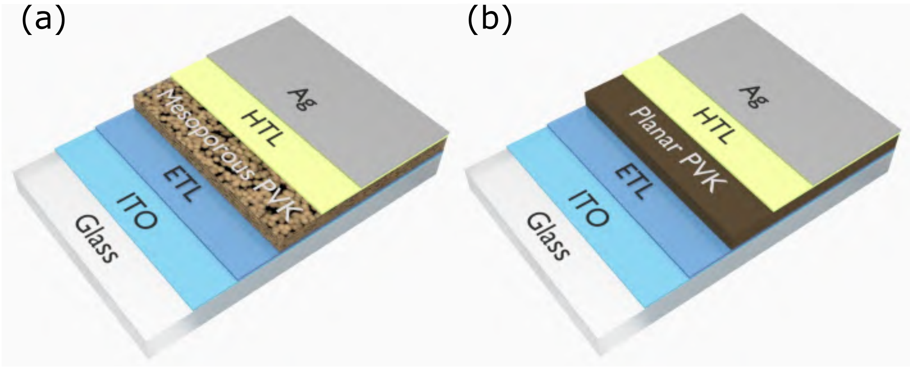

Figure 2.10: Schematic of n-i-p mesoporous (a) and n-i-p planar(b) architectures of perovskite solar cells.

Choice of Antisolvents

The choice of antisolvents in early times were always among toluene [74], diethyl ether[75] and chlorobenzene[8, 87]. Interestingly, these three solvents produce high-quality perovskite films with high photovoltaic efficiencies, despite their different physiochemical properties (such as boiling point and polarity (Table B5 in the Appendix)). In 2017, two reports compared a whole series of different solvents and presented two promising new candidates, namely ethyl acetate [88] and trifluorotoluene [89], which yielded champion efficiencies of 19.4 % and 20.3 %, respectively. One year later, Zhao et al. introduced anisole as an antisolvent for CsMAFA perovskite fabrication, and reached a champion PCE of 19.8 % [90]. The use of anisole as the antisolvent expanded the processing window with a dripping time ranging from 5 to 25 s, an antisolvent volume varying from 0.1 to 0.9 ml, and a DMF:DMSO volume ratio ranging from 6:4 to 9:1 [90]. Interestingly, even ‘poor’ solvents (traditionally considered for perovskite) can yield decent efficiencies. For example, xylene, immiscible with DMF and DMSO, produces a PCE of 17.8 % [89]. In addition, a mixed solvent system (‘good’ + ‘poor’ solvents) is able to produce a plausible PCE of 19.2 %, when 6 % isopropanol (also called 2-propanol) is added to chlorobenzene [91], whereas the isopropanol alone gives only 14.8 % PCE [88]. Nevertheless, there are no clear requirements for a ‘good’ antisolvent (such as high boiling point or strong polarity). Therefore, we will elucidate this issue with a systematic study comparing a large number of solvents in the Chapter 6.

2.3.5 Device Architecture and Charge Selective Contacts

The perovskite layer is sandwiched between an n-doped layer that functions as electron selective contact (ESC) and a p-doped layer working as hole selective contact (HSC), where the selectivity is achieved by the conductivity of only one type of the charge carriers and the matched energetic level. The n-i-p or p-i-n solar cells are named according to the layer stacking order, where incident light passes through the ESC or HSC first. The very first perovskite solar cells were fabricated by depositing

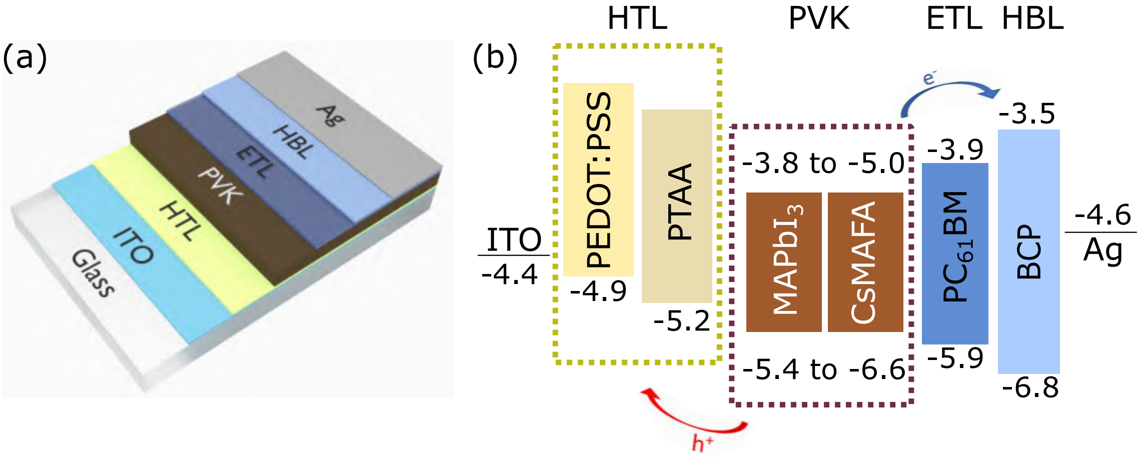

Figure 2.11: (a) Schematic of a planar p-i-n perovskite solar cell. (b) Energy diagram of the anode (i.e., indium tin oxide (ITO)), hole transporting layer (HTL), perovskite layer [92–97], electron transporting layer (ETL), hole blocking layer (HBL) [98] and cathode (i.e., Ag) used in the device architecture (a). [99, 100]

perovskite on a mesoporous electron transport layer (ETL) [3, 4, 23] or an ETL with a porous scaffold [5], whose structure is referred to as the n-i-p mesoporous architecture (Figure 2.10a). The n-i-p planar architecture (Figure 2.10b) describes the type of perovskite solar cells that the perovskite film is coated on a planar ETL.

In this work, we employ the planar p-i-n architecture (also known as the inverted device architecture), where the perovskite film is coated on a planar hole transporting layer (HTL), as illustrated in Figure 2.11a. This device structure originates from the regular architecture used in the organic photovoltaics (OPVs). Therefore, the charge transport materials that are well studied and widely used in OPVs can be utilised in perovskite solar cell as well. Figure 2.11b shows the energy diagram of the anode (i.e., indium tin oxide (ITO)), hole transporting layer (HTL), perovskite layer [92–97], electron transporting layer (ETL), hole blocking layer (HBL) [98] and cathode (i.e., Ag) in this planar p-i-n architecture [99, 100].

Hole Transport Layers (HTLs)

Although functioning HTL-free inverted perovskite cells have been reported [101], the photovoltaic performance is heavily hindered by poor hole extraction due to the mismatch of the work function (WF) between ITO and the valence band of perovskite [100, 102]. Therefore, HTLs are employed between the anode and perovskite layer for better hole extraction with a matched energy level near the valence band of perovskite.

The first inverted perovskite solar cell employed poly(3,4-ethylenedioxythiophene): poly(styrenesulfonate) (denoted by PEDOT:PSS) as the HTL, and had an efficiency of 3.9 % [26]. Recently, highly efficient photovoltaic devices with over 16 % PCE have been produced in the same architecture by improving the perovskite film quality [27–29]. The PEDOT:PSS film is deposited by spin coating followed by a low temperature annealing process, making it ideal for up-scaling and application on flexible substrates. However, it has a work function in a range from 4.9 to 5.2 eV (depending on the ratio of PEDOT to PSS) [103], lower than the literature reported ionization potential values of perovskite (5.4-6.6 eV [92–97]), limiting the V_{OC} of the inverted devices [103, 104]. Another possible reason for the V_{OC} loss for PEDOT:PSS based perovskite solar cells is non-radiative recombination at the PEDOT:PSS/perovskite interface [105, 106]. Moreover, the acidic and hygroscopic nature of the PEDOT:PSS corrodes the ITO electrode [107, 108], and it might react with perovskite, causing degradation and hindering the long-term device stability [109, 110].

Research to improve the V_{OC} of perovskite solar cells has been investigated in three approaches: modifying the PEDOT:PSS (e.g. by adding PSS-Na to the PEDOT:PSS to achieve a higher WF [111]), employing p-type metal oxides with a deep lying valence band (such as NiO_X [104, 110, 112]), and using p-type organic polymers [109, 113–115].

In this work, poly(bis(4-phenyl)(2,4,6-trimethylphenyl)amine) (PTAA) is employed as an alternative to PEDOT:PSS in Chapter 6. The boost of V_{OC} to 1.10 V is partially ascribed to a higher work function of PTAA than PEDOT:PSS [114]. More importantly, the non-wetting surface of the PTAA film results in enhanced grain quality of perovskite films with reduced grain boundaries. Therefore, charge recombination at the HTL/perovskite interface is much reduced, which is the dominating factor in the V_{OC} improvement [114, 115].

In order to overcome the coverage issue of the hydrophilic perovskite precursor solution on the surface of the hydrophobic PTAA layer, a amphiphilic interfacial compatibilizer poly [(9,9-bis(3'-(N,N-dimethylamino)propyl)-2,7-fluorene)-alt-2,7-(9,9–dioctylfluorene)] (PFN-P_2) is coated between the PTAA and perovskite layer [116]. This ultra thin PFN-P_2 layer modifies the surface energy of the PTAA layer, and facilitates the formation of a high-quality perovskite film without affecting the electronic properties of the perovskite.

Electron Transport Layers (ETLs)

[6,6]-phenyl C61 butyric acid methyl ester ($PC_{61}BM$) has already been used as ETL in the early reported inverted perovskite solar cells [26, 117] to facilitate electron extraction and transport. It has be demonstrated that the photocurrent hysteresis is significantly reduced by the incorporation of $PC_{61}BM$ between the perovskite layer and metal cathode in inverted solar cells [118–121]. Some attribute this reduced hysteresis to the fact that $PC_{61}BM$ passivates any charge trapping states at the surface and grain boundaries of the perovskite layer [118, 119]. Another reason might be the inhibited ion migration by $PC_{61}BM$ through chemically bonding with the under-coordinated atoms of the perovskite [121] or defective halides [119, 122]. In addition, Petrozza's group proposed that iodine ions that migrate to the $PC_{61}BM$ layer chemically dopes the $PC_{61}BM$, increasing its electron conductivity,

which further contributes to the stabilized photovoltaic output and hysteresis-free behaviour [123].

Hole Blocking Layers (HBLs)

With the incorporation of a hole blocking layer (HBL) such as bathocuproine (BCP) between the $PC_{61}BM$ layer and metal cathode, the leakage current is much reduced due to a smoother interface between the perovskite/$PC_{61}BM$ and cathode, which consequently increases the fill factor of the solar cell [124]. In addition, using metal oxides (such as ZnO) as the HBL prevents iodide infiltration into the metal electrode, and consequently hinders the iodide migration induced degradation of the electrode [125].

2.3.6 Device Stability and Degradation

Unencapsulated perovskite solar cells are reported to be stable up to 500 h under one sun illumination [4] and 1000 h under full sunlight [126] in ambient air, still far from practical and commercial standards. Various causes, such as moisture, oxygen, light, heat, and electric stress, are responsible for the instability and cause degradation. Here we briefly discuss two atmospheric causes - moisture and oxygen.

Moisture induced degradation

Although moisture induced degradation has been reported to cause unencapsulated perovskite to decompose and is responsible for the poor device stability [10], others claim that a proper humidity level (of 30 %-35 %) facilitates the perovskite crystallization, and therefore improves the film morphology [27, 127, 128]. Due to the hygroscopic nature of MAI [129], the absorption of moisture within grain boundaries helps to merge adjacent grains together, which significantly increases the grain size and suppresses the formation of pinholes, and consequently reduces the non-radiative recombination, enhancing the charge carrier life time and photovoltaic performance [27, 128].

At the initial stages of degradation (e.g. short time exposure to a low moisture concentration), monohydrate $MAPbI_3 \cdot H_2O$ is formed. This process is reversible once it is dehydrated [130]. With prolonged exposure to moisture or higher humidity, dihydrate $(MA)_4PbI_6 \cdot H_2O$ starts to form, often accompanied by the formation of PbI_2, which makes this process partially irreversible [130, 131]. Upon exposure to an even higher H_2O vapour pressure for longer periods, it further decomposes into PbI_2 and volatile MAI, becoming completely irreversible [132]. The three following equations describes these three stages of moisture-induced degradation [130, 132]:

$$CH_3NH_3PbI_3 + H_2O \rightleftharpoons CH_3NH_3PbI_3 \cdot H_2O \tag{2.21}$$

$$\begin{aligned}(4-n)CH_3NH_3PbI_3\cdot H_2O + nCH_3NH_3PbI_3\cdot H_2O + (2-n)H_2O \\ \rightleftharpoons (CH_3NH_3)_4PbI_6\cdot 2H_2O + 3PbI_2\end{aligned} \tag{2.22}$$

$$(CH_3NH_3)_4PbI_6\cdot 2H_2O \longrightarrow PbI_2 + 4CH_3NH_3I_3 + 2H_2O \tag{2.23}$$

The choice of the hole-transporting materials plays an important role in the device long-term stability [131]. For instance, hole-transporting materials that employ the hygroscopic lithium salt Li-TFSI (such as Spiro-OMeTAD) should be avoided, as it tends to absorb and introduce water to the perovskite, accelerating the degradation process [131–133]. Habisrentinger et al. presented that using a single-walled carbon nanotube (SWNT) wrapped with a monolayer of a hole-transporting molecular as the HTL dramatically increases the device stability and boosts its lifetime [50].

Oxygen (and Light) induced degradation

Oxygen induced degradation of perovskite has a detrimental effect on the device stability, and is found to degrade perovskite devices much faster (on time scales of minutes to a few hours) in comparison to degradation in humid nitrogen (85 % relative humidity) [55]. The oxygen induced degradation mechanism is first proposed by Aristidou et al. [53]. When $MAPbI_3$ is exposed to light and oxygen, superoxide (O_2^-) is generated through electron transfer from the photo-excited $MAPbI_3$ to molecular oxygen [53]. This reactive superoxide deprotonates the photo-excited $MAPbI_3$, leading to its decomposition into PbI_2, methylamine (CH_3NH_2), iodine and water, as described by the following equations [53]:

$$CH_3NH_3PbI_3 \xrightarrow{light} CH_3NH_3PbI_3^* \tag{2.24}$$

$$O_2 \xrightarrow{CH_3NH_3PbI_3^*} O_2^- \tag{2.25}$$

$$CH_3NH_3PbI_3^* + O_2^- \xrightarrow{deprotonation} CH_3NH_2 + PbI_2 + \frac{1}{2}I_2 + H_2O \tag{2.26}$$

In addition, their ab initio study demonstrates that the iodide vacancies are the energetically preferred sites for the superoxide species [134]. Depositing a layer of iodide salt onto the perovskite film significantly lowers the amount of superoxide species and increases the photoluminescence lifetime. Therefore, iodide salt are able to passivate the perovskite film and reduce the superoxide formation, and consequently improve the film and device stability [134]. Other reports have highlighted the importance of efficient electron extraction in reducing the formation of superoxide species [53–55, 135]. Device stability can be much improved if the photon-generated electrons are removed by an efficient ETL before their reaction with O_2 to form O_2^-. We demonstrated that devices using $PC_{61}BM$ as ETL degraded at similar speeds in dry air and nitrogen thanks to its efficient removal of electrons [125].

Aristidou et al. have also shown that light-induced superoxide species form much more on perovskite films with smaller grain size. Therefore, devices with poorer perovskite crystallinity degrade at a faster speed and are less stable [134]. In Chapter 4, we will reveal the correlation of the oxygen induced degradation and the microstructure and grain boundaries in the perovskite film.

3 Experimental Methods

3.1 Overview

This chapter describes the processes involved in fabricating perovskite solar cells: substrate cleaning, precursor solution preparation, film deposition via spin-coating, and thermal evaporation of anode. Then, the main techniques for characterizing perovskite films and devices are described.

3.2 Film and Device Fabrication

Spin coating was the main technique employed for thin film deposition in this thesis, where a small amount of solution with coating materials dissolved is applied on top of the sample, before its rotation at a certain speed. The centrifugal force from the rotation spreads the material evenly and forms a neat thin film following the thermal annealing process. Film thickness depends on rotation speed and solution concentration. Metal contacts were deposited by thermal evaporation. We only used Ag as our cathode.

3.2.1 Substrates

Indium-tin oxide (ITO) coated glass substrates were used for film and device fabrication. They were purchased from PsiOTec Ltd. and pre-patterned with one ITO stripe (7 mm × 12 mm) centred on the 12 mm × 12 mm soda-lime glass substrate. The ITO serves as anode in the inverted device and has a sheet resistance of 15 Ω/sq. On each substrate, eight pixels (3 mm × 1.5 mm) were fabricated, increasing the total number of solar cells taken into statistics. ITO substrates were cleaned sequentially with 2 % Hellmanex detergent, deionized water, acetone and 2-propanol in an ultrasonic bath. After drying with an N_2 gun, they were treated with oxygen plasma at 100 mW for 10 min.

3.2.2 Hole Transport Layers

PEDOT:PSS, short for poly (3, 4-ethylenedioxythiopene)-poly (styrenesulfonate): It was used as purchased. Before spin coating, it was sonicated and filtered with a 0.45 μm polyvinylidene difluoride (PVDF) filter. Cleaned and plasma-treated ITO substrates were covered with PEDOT:PSS solution, spin-coated at 4000 rpm for 30 s and annealed at 150 °C for 10 min in ambient air.

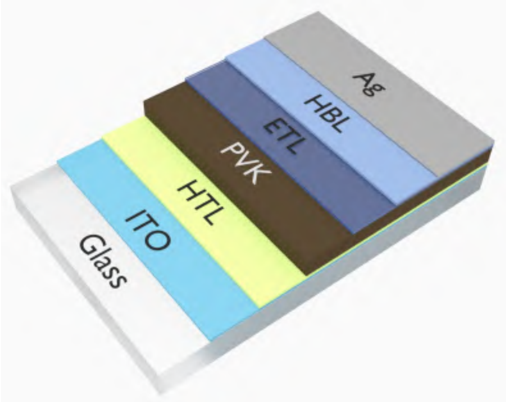

HTL: PEDOT:PSS or PTAA

ETL: $PC_{61}BM$

HBL: BCP

Figure 3.1: Schematic of an inverted perovskite solar cell used in this work.

PTAA, abbreviated for poly(triaryl amine), poly[bis(4-phenyl)(2,4,6-trimethylphenyl)amine]: It was dissolved in anhydrous toluene with a concentration of 1.5 mg/ml and stirred at 70 °C for 2-3 hours until fully dissolved. After cooling down to room temperature, 30 μl of PTAA solution was applied to clean substrates and spin-coated at 2000 rpm for 30 s. Samples were annealed at 100 °C for 10 min in a dry air filled glovebox.

PFN-P_2, short for poly [(9,9-bis(3'-(N,N-dimethylamino)propyl)-2,7-fluorene)-alt-2,7-(9,9–dioctylfluorene)]: It was used together with PTAA as a modifier for better wetting and higher voltage output. It was dissolved in anhydrous methanol with a concentration of 0.5 mg/ml and fully mixed by stirring overnight at room temperature. 30 μl of PFN-P_2 solution was spin coated onto PTAA-coated ITO substrates at 5000 rpm for 30 s in a dry air filled glovebox.

3.2.3 Perovskite Layers

Two types of perovskite were studied in the following chapters. One is methylammonium lead triiodine ($CH_3NH_3PbI_3$). The other is a 'triple cation' perovskite with the composition of $Cs_{0.05}(MA_{0.17}FA_{0.83})_{0.95}Pb(I_{0.9}Br_{0.1})_3$, containing three cations (i.e., Cs^+, MA^+ and FA^+) and two anions (i.e., Br^- and I^-). They were prepared by spin coating of the perovskite precursor solution and thermal annealing in a dry air filled glovebox (relative humidity $< 1.0\,\%$).

Single Cation Perovskite $CH_3NH_3PbI_3$

Three various fabrication methods were employed to prepare $CH_3NH_3PbI_3$ perovskite films in chapter 4 and 5.

$Pb(OAc)_2$ recipe

The perovskite precursor solution for the $Pb(OAc)_2$ recipe was prepared by dissolving lead acetate trihydrate ($Pb(OAc)_2{\cdot}3H_2O$) and methylammonium iodide (CH_3NH_3I) at a molar ratio of 1:3 in anhydrous dimethylformamide (DMF) with a weight concentration of 40 % and an addition of hypophosphorous acid 50 % aqueous solution (1.7 μl per 100 mg CH_3NH_3I). The perovskite solution was spin coated at 2000 rpm for 60 s. After drying at room temperature for 5 min, the as-spun films were annealed at 100 °C for 5 min.

sol-eng recipe

The perovskite precursor solution for the sol-eng recipe was prepared by dissolving PbI_2 and CH_3NH_3I at a molar ratio of 1:1 in a solution mixture of anhydrous γ-butyrolactone (GBL) and dimethylsulfoxide (DMSO) (7:3, v/v), with a weight concentration of 40 %, and stirring at 70 °C for 2-3 hours. The perovskite solution was spin coated first at 1000 rpm for 15 s and then at 4000 rpm for 25 s. During the second step, 600 μl of toluene was dripped onto the rotating sample 5 s before the end of the second spinning step. The as-spun films were annealed directly at 100 °C for 15 min.

1-1-1 recipe

The perovskite precursor solution for the 1-1-1 recipe was prepared by dissolving PbI_2, CH_3NH_3I and DMSO (1:1:1, molar ratio) in anhydrous DMF, with a weight concentration of 50 %, and stirring at 70 °C for 2-3 hours. The perovskite solution was spin coated at 2000 rpm for 25 s, and 500 μl of diethyl ether was dripped onto the rotating sample 3 s before the end of the spinning step. The as-spun films were annealed directly at 60 °C for 1 min and then at 100 °C for 2 min.

Triple Cation Perovskite $Cs_{0.05}(MA_{0.17}FA_{0.83})_{0.95}Pb(I_{0.9}Br_{0.1})_3$

The precursor solution for the triple cation perovskite contains five different powders of PbI_2, $PbBr_2$, CsI, methylammonium iodine (MAI) and formamidinium iodine (FAI) mixed at a specific molar ratio in a solution mixture of DMF and DMSO. In order to obtain the target stoichiometry and keep the preparation easy and reproducible, we prepared the stock solution as described in the following method. First, we prepared stock solutions of PbI_2 and $PbBr_2$ with an actual molarity of 1.155 M (1 M = 1 mol/L) in a solvent mixture of DMF and DMSO (4:1, v:v, denoted by DMF/DMSO). The solutions were heated at 180 °C for 3 min, resulting a fully dissolved clear solution. The CsI stock solution with a molarity of 1.155 M was prepared by adding CsI powder in DMSO and heating at 150 °C for 3 min. The amount of solvent added to obtain the target molarity is calculated by the following steps.

For convenience, we prepared the CsI solution with 2 mol CsI per L of DMSO, PbI_2 and $PbBr_2$ solutions with 2.5 mol per L in the DMF/DMSO mixture. The density of the stock solution was calculated from the weight of 100 μl of solution at around 25 °C. (Table 3.1) The molarity of the precursor solution can then be calculated from the densities of the solutions and the solvents by:

$$M_{solution} = \frac{mol_{powder}}{V_{solution}} = \frac{mol_{powder} \cdot d_{solution}}{Mw_{powder} \cdot mol_{powder} + V_{solvent} \cdot d_{solvent}} \tag{3.1}$$

where $M_{solution}$ is the molarity of the precursor solution; mol_{powder} is the number of moles of the precursor; $V_{solution}$ is the volume of the final solution; Mw_{powder} is the molecular weight of the precursor; $d_{solution}$ is the density of the precursor solution; and $V_{solution}$ is the volume of the added solvent.

After the addition of precursors, the volume of the stock solutions increased compared to the volume of added solvents and the extent of this expansion in volume is calculated by:

$$\gamma_{\mathrm{V}} = \frac{V_{solution}}{V_{solvent}} = \frac{a}{M_{eg}} \tag{3.2}$$

where γ_{V} is the volume factor listed in Table 3.1 and assumed to be constant in the following calculations; a is the number of moles of the precursor per L solvent, and in this case equals 2.5 for PbI_2 and $PbBr_2$ and 2.0 for CsI, respectively; M_{eg} is the molarity of the stock solution in Table 3.1.

The volume of solvent needed to be added to obtain the target molarity ($M_{solution}$, in this case 1.155 M) was calculated using the following formulae:

$$V_{solvent} = \frac{W_{powder}/Mw_{powder}}{M_{solution}} - V_{exp} \tag{3.3}$$

$$V_{exp} = \frac{W_{powder}/Mw_{powder}}{a} \cdot (\gamma_{\mathrm{V}} - 1) \tag{3.4}$$

where a equals 2.5 for PbI_2 and $PbBr_2$ and 2.0 for CsI, respectively; W_{powder} is the weight of the precursor solid and Mw_{powder} is the molecular weight of the precursor.

Table 3.1: Densities, molarities and volume factors of the solvents and examples of stock solutions.

Solvent	-	Density (g/ml)	-	-
DMSO	-	1.100 ± 0.001	-	-
DMF/DMSO (4:1, v:v)	-	0.975 ± 0.001	-	-
Solution	Moles per L	Density (g/ml)	Molarity (mol/L)	Volume Factor (γ_{V})
CsI (DMSO)	2	1.440 ± 0.001	1.778	1.124
PbI_2 (DMF/DMSO)	2.5	1.810 ± 0.001	2.127	1.176
$PbBr_2$ (DMF/DMSO)	2.5	1.664 ± 0.001	2.198	1.137

The final inorganic stock solution (1.1 M $Cs_{0.05}PbI_{1.75}Br_{0.3}$) was obtained by mixing the 1.155 M PbI_2, $PbBr_2$ and CsI stock solutions with a volume ratio of 0.85 : 0.15 : 0.05.

Methylammonium iodine (MAI) and formamidinium iodine (FAI) powders were weighted out into two separate vials. To obtain the solutions with the stoichiometric formulae of $Cs_{0.05}MA_{0.95}PbI_{2.7}Br_{0.3}$ and $Cs_{0.05}FA_{0.95}PbI_{2.7}Br_{0.3}$, the volume of the

$Cs_{0.5}PbI_{1.75}Br_{0.3}$ stock solution to add was calculated by this formula:

$$V_{stocktoadd} = \frac{W_{powder}/Mw_{powder}}{M_{organic/Pb} \cdot M_{Pb}} \tag{3.5}$$

where $M_{organic/Pb}$ is the molar ratio of FA or MA to Pb and equals 0.95; M_{Pb} is the molar concentration of Pb and equals 1.10. It is important to note that the volume factors of FAI and MAI dissolving in the inorganic stock solution calculated by Equation 3.2 are approximately the same (Table B1, Appendix).

Finally, the perovskite solution with the stoichiometric formula of $Cs_{0.05}(MA_{0.17}FA_{0.83})_{0.95}PbI_{2.7}Br_{0.3}$ was obtained by mixing the $Cs_{0.05}MA_{0.95}PbI_{2.7}Br_{0.3}$ and $Cs_{0.05}FA_{0.95}PbI_{2.7}Br_{0.3}$ solutions in a 1:5 volume ratio.

The perovskite solution was spin coated first at 1000 rpm for 12 s and then at 6000 rpm for 28 s. During the second step, 200 µl of antisolvent was dripped onto the rotating sample 5 s before the end of the spinning step. The as-spun films were annealed directly at 100 °C for 30 min. Solvents used as antisolvent are listed in Table 3.2.

3.2.4 Electron Transport Layers

$PC_{61}BM$, short for [6,6]-phenyl C61 butyric acid methyl ester: It was dissolved in anhydrous chlorobenzene with a concentration of 20 mg/ml and stirred at 70 °C for 2-3 hours until fully dissolved. After cooling down to room temperature, the $PC_{61}BM$ solution was filtered through a 0.25 µm polytetrafluoroethylene (PTFE) filter before use. 20 µl was then dynamically spin coated on the perovskite films at 2000 rpm. Afterwards, the samples were annealed at 100 °C for 10 min in a N_2 filled glovebox.

BCP, short for bathocuproine: It was dissolved in anhydrous 2-propanol with a concentration of 0.5 mg/ml and stirred at 70 °C overnight. The solution was prepared and stored in the N_2 filled glovebox. BCP solution was dynamically spin coated at 4000 rpm after $PC_{61}BM$ deposition.

3.2.5 Materials

We listed all materials and solvents used in this thesis in Table 3.2.

Table 3.2: List of all chemicals, together with the producer, CAS and product number.

Chemical	Producer	CAS	Product number
Perovskite Precursors			
CH_3NH_3I (MAI)	Greatcell Solar	14965-49-2	MS101000
$CH(NH_2)_2I$ (FAI)	Greatcell Solar	879643-71-7	MS150000
CsI	abcr GmbH	7789-17-5	AB207757
$Pb(OAc)_2 \cdot 3H_2O$	Sigma-Aldrich	6080-56-4	316512
PbI_2	TCI Deutschland	10101-63-0	L0279
$PbBr_2$	TCI Deutschland	10031-22-8	L0288
Solvents for Perovskite Solution			
Dimethylformamide (DMF)	Sigma-Aldrich	68-12-2	227056
Dimethyl sulfoxide (DMSO)	Sigma-Aldrich	67-68-5	276855
γ-Butyrolactone (GBL)	Sigma-Aldrich	96-48-0	B103608
Solvents used as Antisolvent			
Anisole	Sigma-Aldrich	100-66-3	296295
1-Butanol	Sigma-Aldrich	71-36-3	281549
Butyl acetate	Sigma-Aldrich	123-86-4	287725
Chlorobenzene	Sigma-Aldrich	108-90-7	284513
Chloroform	Sigma-Aldrich	67-66-3	288306
Diethyl ether	Sigma-Aldrich	60-29-7	346136
1,2-Dichlorobenzene	Sigma-Aldrich	95-50-1	240664
Ethanol	Sigma-Aldrich	64-17-5	32205
Ethyl acetate	Sigma-Aldrich	141-78-6	270989
Methanol	Sigma-Aldrich	67-56-1	322415
2-Propanol	Sigma-Aldrich	67-63-0	278475
Toluene	Sigma-Aldrich	108-88-3	244511
Trifluorotoluene	Sigma-Aldrich	98-08-8	547948
p-Xylene	Sigma-Aldrich	106-42-3	296333
Organic Polymers			
PEDOT:PSS	Heraeus	-	Clevios P VPAI 4083
PTAA	Sigma-Aldrich	1333317-99-9	702471
PFN-P_2	1-Material	889672-99-5	OS0995
$PC_{61}BM$	Solenne BV	160848-22-6	-
Bathocuproine (BCP)	Sigma-Aldrich	4733-39-5	699152
Others			
Hypophosporous acid (HPA)	Sigma-Aldrich	6303-21-5	1046330500

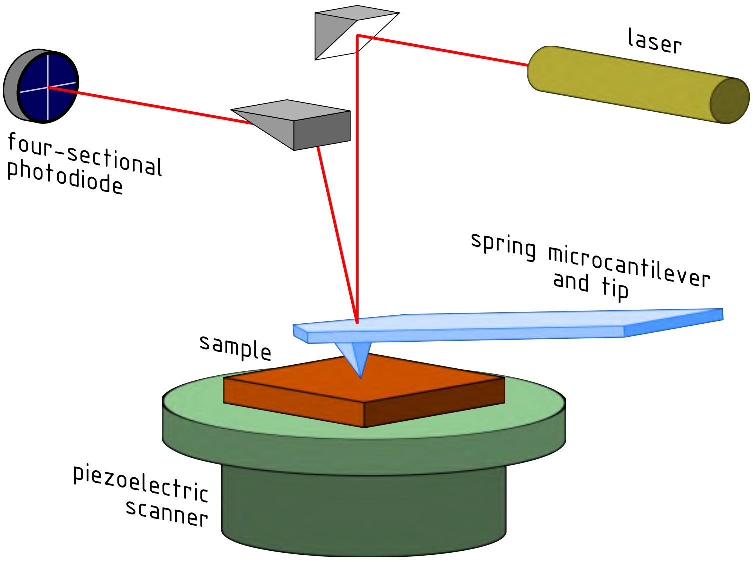

Figure 3.2: Schematic of an AFM. Reproduced with permission from [136]. Copyright GregorioW, licensed under Creative Commons Attribution-Share Alike 3.0 Unported license.

3.3 Film and Device Characterization

3.3.1 Profilometery

Layer thicknesses were measured with a Veeco Dektak 150 profilometer. A diamond stylus with a diameter of 12.5 μm comes into contact with a sample, and then scans the surface with specified contact force (1-15 mg) in a specified direction. The profilometer then records the vertical position of the stylus, which is then tracked and displayed in absolute values. In order to measure the thickness of a film on the substrate, the film was scratched without any damage to the substrate. Film thickness was determined by scanning the stylus across this scratch.

3.3.2 Atomic Force Microscopy (AFM)

AFM was performed with a Bruker MultiMode microscope in tapping mode in air with silicon tips (Bruker NTESPA) to study the surface morphology of the perovskite films. A cantilever with a very small radius tip is scanned over the sample surface within certain distance, where the cantilever is first attracted by Van-der-Waals forces and then repelled due to Pauli-principle. In the tapping mode, the cantilever is driven to oscillation by a piezo crystal close to its resonance frequency. When the tip rasters across the sample, affected by the attractive and repulsive forces, the resonance frequency of the cantilever is reduced. Consequently, the oscillation amplitude at the constant driving frequency is attenuated. The movement of the cantilever is monitored by the reflection of a laser off of the top of the cantilever by

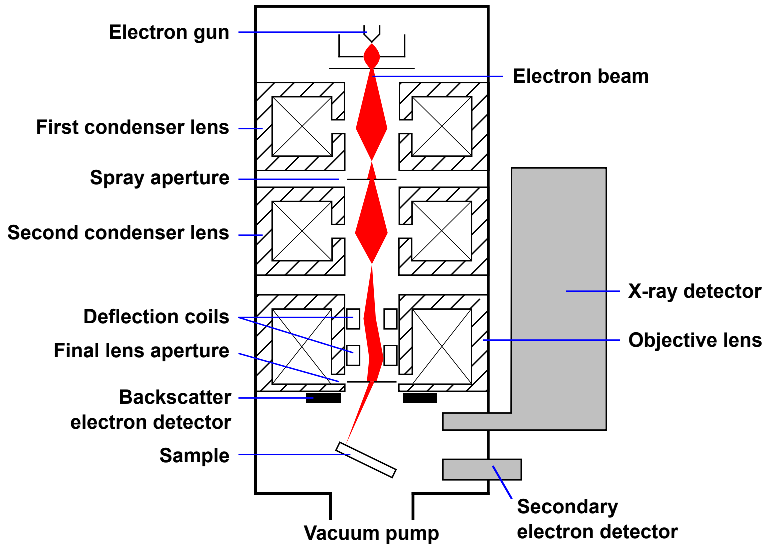

Figure 3.3: Schematic of an SEM. Reproduced with permission from [137]. Copyright Steff, ARTE and MarcoTolo, licensed under Creative Commons Attribution-Share Alike 1.0 Generic license.

a segmented photo diode, and fed back to the cantilever to maintain constant force (Figure 3.2). The average grain size of perovskite films in Chapter 5 was estimated using the software Gwyddion.

3.3.3 Scanning Electron Microscopy (SEM)

In typical scanning electron microscopy (SEM), a thermionically emitted electron beam generated from an electron gun is focused on the sample by one or two magnetic condenser lenses to a spot about 0.4 to 5 nm in diameter. The interaction of the electron beam with the sample results in reflected and backscattered high-energy electrons (BSE), emission of low-energy secondary electrons (SE), characteristic X-rays and light (cathodoluminescence), which can be detected by specialised detectors. The SEs originate from the inelastic scattering of beam electrons with the conduction, or valence, band of the atoms, and has lower energy than the BSE, which is a result of elastic collisions of electrons and specimen atoms. Due to its low energy, SEs emerge from within a few nanometers below the sample surface, and provide high-resolution topographic images of the sample.

The SEM images in this work is taken in the secondary electron imaging mode. The SEM measurements in Chapter 4 were performed by Dr. Paul Fassl, using an Ultra FE-SEM Gemini Ultra 55 (Zeiss) microscope with a working distance of 3 mm and an acceleration voltage of 1.6 kV. The SEM measurements in Chapter 5 were carried out by Dr. Paul Fassl, using an JSM-7610F FEG-SEM (Jeol) with a working distance of 2 mm and an acceleration voltage of 1.5 kV. The SEM measurements in Chapter 6 were performed by Dr. Fabian Paulus, using an JSM-7610F FEG-SEM

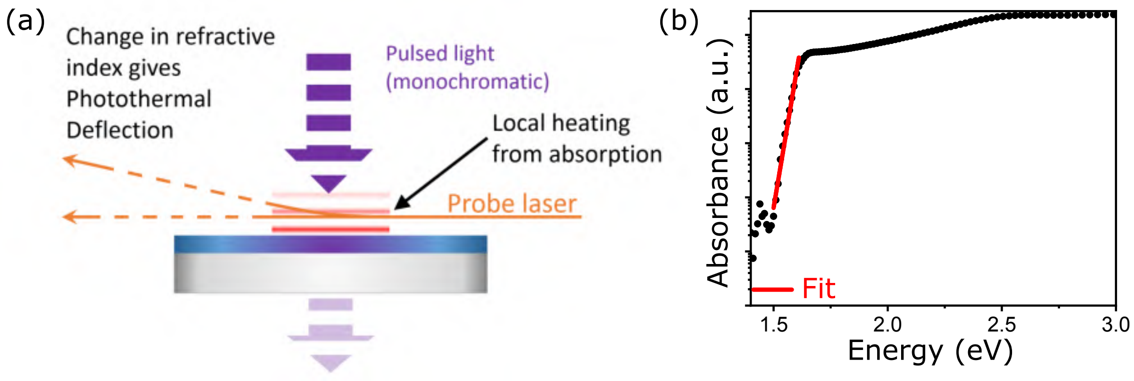

Figure 3.4: (a) Schematic of working principle of PDS. Courtesy of Dr. Paul Hopkinson. (b) Absorption spectra of a pristine $CH_3NH_3PbI_3$ perovskite sample. The absorption edge near the band gap is fitted linearly (red line) to estimate the Urbach energy.

(Jeol) with a working distance of 2 mm and an acceleration voltage of 1.5 kV.

3.3.4 X-Ray Diffraction (XRD)

X-ray diffraction (XRD) measurements were conducted by Bruker, Karlsruhe as part of demonstration measurements on a D8 ADVANCE DaVinci diffractometer equipped with a PILATUS3-100K detector. 2D-XRD measurements of thin perovskite films were collected in a stepwise $\theta/2\theta$ scan from 0-30°. After combining the individual frames to a full 2D diffraction map, a central slit profile was used to obtain the 1D diffraction profile, followed by background correction and stripping the K_β line using the Bruker DIFFRAC.EVA Software.

3.3.5 UV-vis Spectroscopy (UV-vis)

Optical absorption spectra were measured using a Jasco UV-660 spectrophotometer. The monochromated light passes through the sample, partly absorbed, and the transmitted light is then detected by a photodiode. A baseline correction was performed prior to measurements, where the absorption of substrate was subtracted.

3.3.6 Photothermal Deflection Spectroscopy (PDS)

Photothermal deflection spectroscopy (PDS) employs a mirage-like effect to very precisely measure absorption of thin films. The refractive index adjacent to the sample surface changes due to heating of the sample by absorption of light. Light radiated by a 150 W Xenon short-arc lamp (Ushio) is sent through a monochromator (Cornerstone 260 Oriel) to generate a monochromatic pump beam, which is absorbed by the sample and generates a pulsed heat wave. The heat changes the refractive index of an inert liquid (Fluorinert, FC-770 (IoLiTec)) surrounding the sample, and consequently causes a deflection of a probe He-Ne-laser (REO) close to the sample surface (Figure 3.4a). This deflection was monitored by a position-sensitive-detector (Thorlabs, PDP90A) and a lock-in amplifier (Amatec SR 7230).

Spectrosils from UQG Optics were used as substrates for all PDS measurements. In Chapter 4, PDS was employed to determine Urbach energies of the perovskite films. The Urbach energy E_U can be estimated by fitting the exponential Urbach tail in the range of the measured absorption edge near the band gap (Figure 3.4b).

$$A(E) = V \cdot exp(\frac{E}{E_U}) \tag{3.6}$$

where A is the absorption, V is a normalisation factor and the slope of the absorption edge in the semi-log is the inverse Urbach energy E_U.

The PDS measurements in Chapter 4 were performed by David Becker-Koch and Alexandra Bausch. The experimental setup was built by Stefan Lannig and David Becker-Koch [138, 139].

3.3.7 Photoemission Spectroscopy

Photoemission spectroscopy (PES) is based on the photoelectric effect, where electrons can be emitted when photons with the right amount of energy strike a material. Depending on the ionization energy, PES is divided into X-ray photoemission spectroscopy (XPS) and ultra-violet photoemission spectroscopy (UPS). Regardless of the incident photon beam, the PES is carried out in a ultra high-vacuum (10^{-10} mbar) system (Thermo Scientific ESCALAB 250Xi).

X-Ray Photoemission Spectroscopy (XPS)

XPS measurements were performed by irradiating the sample with an X-Ray beam generated by XR6 monochromated Al Kα source ($h\nu = 1486.6$ eV) with a pass energy of 20 eV. The kinetic energy of the emitted electrons from the core levels of specimen atoms is measured. Each element has a characteristic XPS spectrum, with peaks at certain binding energies corresponding to the configuration of electrons in the atoms, where the peak intensity (i.e., the number of detected photoelectrons at the specified peak) is related to amount of the element within the sampling region. To determine the chemical composition, the atomic percentage of each element is calculated by fitting the respective peak with a convolution of Gaussian and Lorentzian functions, and corrected by the relative sensitivity factor (RSF) (except for hydrogen, as it cannot be detected). The photoelectrons undergo inelastic collisions before escaping the sample and being detected, which exponentially attenuates the number of escaped photoelectrons with depth. Therefore, XPS is a surface-sensitive technique and only detects the top 10 nm of the sample.

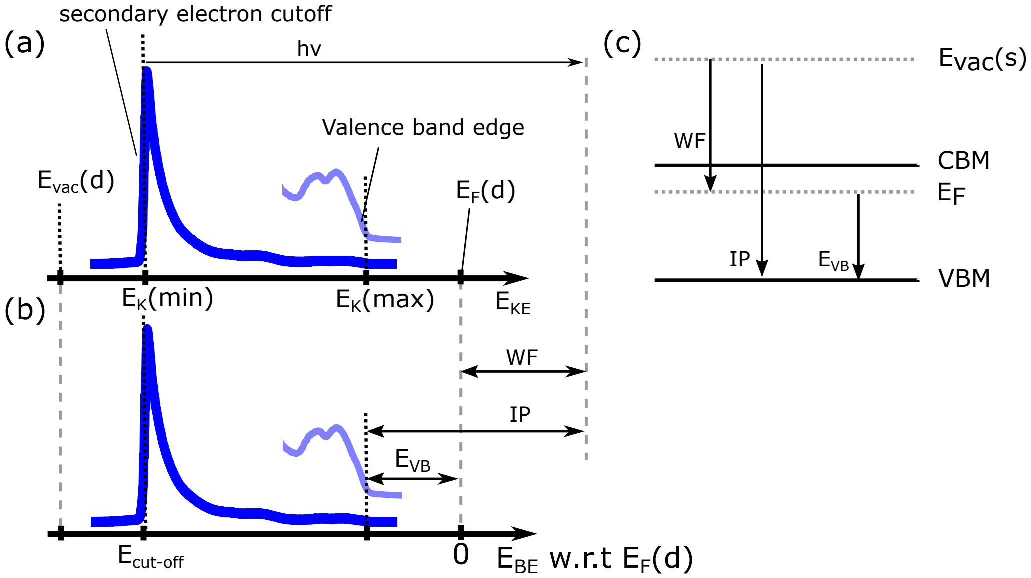

Figure 3.5: UPS spectrum of a pristine $CH_3NH_3PbI_3$ sample illustrated (a) in the scale of kinetic energy, (b) in the scale of binding energy with respect to the Fermi level. (c) Schematic of an energy band diagram illustrating the relevant energies.

Ultra-Violet Photoemission Spectroscopy (UPS)

UPS measurements were carried out using an He discharge lamp ($h\nu = 21.2\,\text{eV}$, He $I\alpha$) and a pass energy of 2 eV. The UPS spectrum shows the density of states, from which the work function (WF) and the ionization potential (IP) can be determined.

UPS measures the kinetic energy of the emitted electrons that are excited from the valence band. Electrons that have enough energy to escape the specimen, are emitted with a kinetic energy of vacuum level of the sample or above. Electrons that just escape the sample have the lowest kinetic energy (E_K(min)), which is the secondary electron cutoff (SECO) measured by the detector. Therefore, E_K(min) is determined by the difference of the vacuum level of the sample E_{vac}(s) and that of the detector E_{vac}(d). In comparison to the primary electrons, secondary electrons undergo inelastic scattering before leaving the sample surface and produce a peak above the SECO in the emitted spectrum. The maximum kinetic energy E_K(max) is the energy of electrons at the Fermi level for metals, or at the valence band maximum (VBM) for semiconductors.

In order to include this SECO in the spectrometer response, the sample is usually biased by applying a negative voltage (e.g. -10 V). This negative biasing ensures that the vacuum level of the sample lies above the vacuum level of the detector. Typically, the Fermi level of the detector E_F(d) is obtained by measuring the Fermi edge of a clean metal sample (e.g. 31.2 eV for -10 V bias), and set to zero in the scale of binding energy. The conversion from the kinetic energy to binding energy is described as:

$$E_{BE} = h\nu - E_{KE} - E_F(d) \tag{3.7}$$

The WF is determined as the energy difference between the vacuum level and the Fermi level of the detector. The IP is obtained by the sum of the WF and the difference between Fermi level and the valence band edge E_{VB}, determined from the x-intercept of the linear fit of valence band onset (Figure 3.5b).

$$WF = h\nu - (E_F(d) - E_k(min)) \tag{3.8}$$

$$IP = WF + E_{VB} \tag{3.9}$$

The UPS measurement collects the kinetic energy of the photoemitted electrons at some distance away from the sample surface. In order to avoid the dependence on the measurement system or the applied bias, the UPS spectra are normally plotted in the scale of binding energy with respect to (w.r.t) the Fermi level, as shown in Figure 3.5b and 3.6d.

3.3.8 XPS and UPS Mapping

In Chapter 5, XPS and UPS mapping were performed on $CH_3NH_3PbI_3$ films deposited on ITO/PEDOT:PSS substrates across the centre area of the samples. Total mapping area is 7.2 mm × 7.2 mm, and contains the active areas of the eight pixels of the final device (Figure A10b, Appendix). The measurements were performed in the dark and all samples had the same exposure time to vacuum and X-ray or UV light.

In order to generate an XPS map with surface compositional information, a serial acquisition of 324 XPS measurements is carried out, with an X-ray spot size of 400 μm and a step size of 400 μm. At each measurement point, Pb 4f and I 3d spectra are collected, and the I/Pb ratio is then calculated from the ratio of the atomic percentages of iodine and lead. An I/Pb map summarizes the distribution of the I/Pb ratio across the sampled area as a two-dimensional colour contour plot, with x- and y- axes representing the probed position and the colour difference representing the changes in surface composition.

UPS mapping experiments were performed in a similar fashion to the XPS mapping. UPS spectra are collected across the sample with a measurement spot size of around 400 μm. At each probed spot, spectra containing information about the secondary electron cutoff and the valence band edge are collected, and the work function and IP are calculated in the way explained in Section 3.3.7. An IP map (two-dimensional colour contour plot with colour changes representing the IP variations) depicts electronic structure distribution across the sampled area.

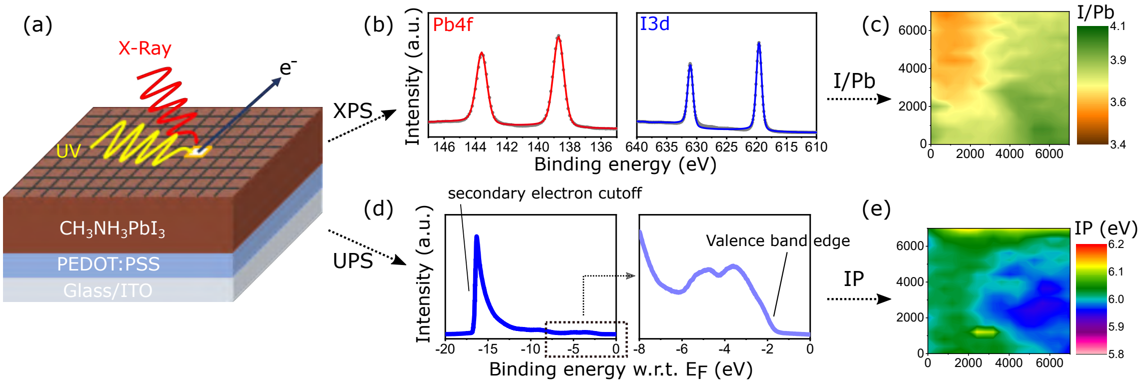

Figure 3.6: (a) Illustration of the experimental approach of XPS and UPS mapping. (b) Pb 4f and I 3d spectra collected at each point. (c) I/Pb map, a two-dimensional plot of iodine to lead (I/Pb) ratio calculated by dividing the atomic percentage of iodine by the atomic percentage of lead for all measured points over the entire sample. (d) UPS spectra collected at each point. (e) IP map, a two-dimensional plot of ionization potential (IP) for all measured points over the entire sample. Adapted with permission from [140]. Copyright 2018, American Chemical Society.

3.3.9 Photoluminescence Quantum Efficiency (PLQE)

Photoluminescence quantum efficiency (PLQE) was measured using an integrating sphere to collect all emitted light. An integrating sphere (also known as an Ulbricht sphere) is a hollow sphere with its interior covered with a white diffuse coating. Light rays incident on the inner surface are scattered multiple times and redistributed isotropically, regardless of the original directions. Hence, light scattered from different locations on the inside of the sphere contributes equally to the measured spectrum. The experimental set up introduced by de Mello et.al.[141], is shown in Figure 3.7. A laser at a wavelength of 532 nm and a spot size of 2 mm is directed into the sphere, and all light is collected by an optical fiber that connects to a spectrometer. Directly in front of the fibre is a baffle coated with the same diffuse material, to prevent direct illumination of incident light.

Three measurements are made using the sphere. The first measurement (Figure 3.7a) measures the laser intensity in the empty sphere. For the second measurement ('off-axis'), the sample placed inside the sphere is out of the laser incoming path and only absorbs the scattered light (Figure 3.7b). For the third measurement ('on-axis'), the laser beam is now directed on to the sample (Figure 3.7c). There are two types of light striking the sample: direct and scattered light from the inner sphere which are reflected or transmitted by the sample. The PLQE can then be calculated with the following formula [141]:

$$\eta = \frac{P_{on} - (1-A) \cdot P_{off}}{L_{empty} \cdot A} \tag{3.10}$$

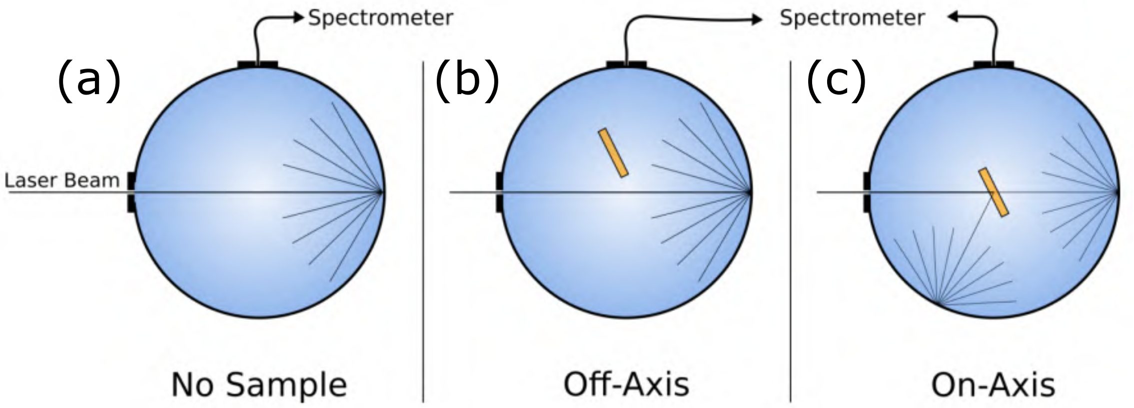

Figure 3.7: Schematic illustration of three configurations of the sphere for the PLQE measurement introduced by [141]. Reproduced with permission from [142]

with

$$A = 1 - \frac{L_{on}}{L_{off}} \tag{3.11}$$

where A is the fraction of the incident light absorbed by the sample in the on-axis measurement; L_{empty}, L_{off} and L_{on} are the areas under the laser peaks for empty, off-axis and on-axis measurements, respectively; P_{off} and P_{on} are the areas under the PL emission peaks for off-axis and on-axis measurements.

The atmosphere in the sphere can be changed by continuously flushing, for example in our setup with nitrogen or dry air.

The PL measurements in Chapter 4 were performed by Alexandra Bausch.

3.3.10 Solar Simulator and J-V measurement Setup

The current density-voltage (J-V) measurements were performed under the simulated sunlight with the Abet Class AAA 3000 sun simulator, which provide the light output matching the ASTM G-173-03 Standard Testing Conditions, 100 mW/cm^2 irradiance and AM 1.5G spectrum. The light intensity was corrected by a spectral mismatch factor, which was obtained by measuring the spectral response of the perovskite solar cell and a Si reference cell (NIST traceable, VLSI), and the spectral irradiance of the solar simulator and the AM 1.5G solar spectrum. The photovoltaic devices were measured with a Keithley 2400 Source Measure Unit and scanned from 1.2 V to 0 V and back, with a step size of 0.025 V and an equilibrium time of 0.1 s after holding under illumination at 1.2 V for 2 s. The active pixel size is 4.5 mm^2.

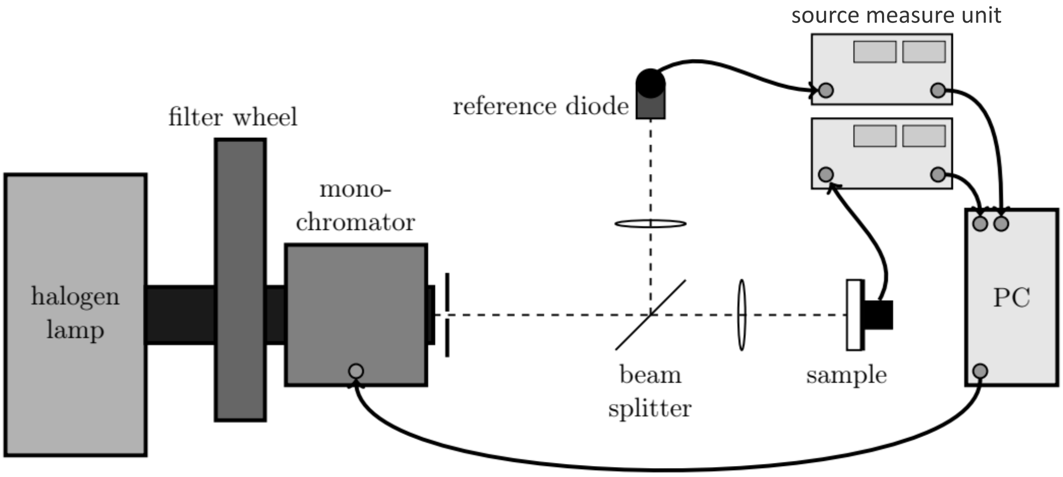

Figure 3.8: Schematic illustration of the EQE setup. Adapt with permission from [143]

3.3.11 External Quantum Efficiency (EQE)

Light irradiated from a halogen lamp was monochromated in a range from 375 to 820 nm and split into two parts by a beam splitter. One part was focused on one pixel of a photovoltaic device and the other on a reference diode which was calibrated with a NIST-traceable Si diode (Thorlabs) prior to measurements (Figure 3.8). The signals from the illuminated pixel and the reference diode were measured with two Source Measure Units, respectively. A Labview program was then used to evaluate these signals in order to obtain the EQE spectrum.

3.3.12 Environmental Rig

The environmental rig and the sample holder was designed and built by A. Weu and Dr. Paul Hopkinson [144]. The environmental rig is flushed with nitrogen (Purity: 99.999 %) as the carrier gas, and is mixed with oxygen (Purity: 99.99 %) to obtain the desired O_2 percentage by adjusting the relative flow rate of O_2 to N_2. In order to control the level of humidity, the incoming N_2 gas travels through a water bubble where the humidity is introduced and can be adjusted by the ratio of humid and dry N_2. The oxygen and humidity levels are monitored by different sensors (oxygen sensor: Cambridge Sensotet, Rapidox 2100; humidity sensor: Michell instruments, Easy Dew) continuously before or after being connected to the sample holder, which can hold four samples at the same time.

For all the oxygen degradation studies, the perovskite films were stored in a nitrogen filled glovebox after fabrication, and transferred to a sealed sample holder without exposure to moisture or oxygen. All the samples were degraded at various oxygen levels under simulated AM 1.5G sunlight at 100 mW/cm^2 irradiance (Abet

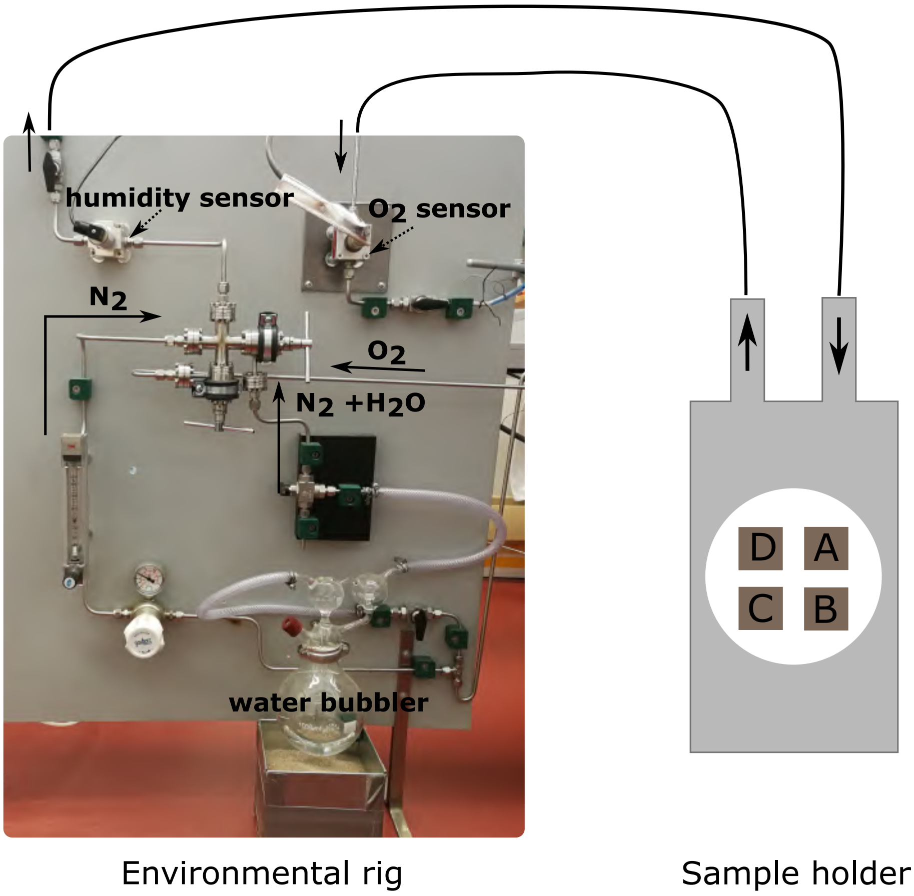

Figure 3.9: Image of the self-built environmental rig that flushes the sample holder with controlled atmosphere.

Sun 3000 Class AAA solar simulator) for 10 h.

4 Oxygen and Light Induced Photodegradation

4.1 Overview

This chapter is based on our recent publication in the journal Advanced Energy Materials with the title 'Role of Microstructure in Oxygen Induced Photodegradation of Methylammonium Lead Perovskite Films' [58]. Most graphs are reproduced or adapted with permission from Wiley VCH. This project was performed in collaboration with Dr. Paul Fassl, who fabricated the samples utilizing $Pb(OAc)_2$ recipe and performed SEM measurements. The PDS measurements were performed by David Becker-Koch and Alexandra Bausch. The PL measurements were performed by Alexandra Bausch.

4.2 Introduction

When we started this study at the beginning of 2016, although the perovskite community had already reported on device stability issues caused by various reasons, such as oxygen, humidity, UV light, heat and electrical stress [47, 51, 52, 145], the main cause for the perovskite instability was thought to be the degradation of $CH_3NH_3PbI_3$ ($MAPbI_3$) into PbI_2 under humid atmosphere based on numerous studies [50, 130, 131, 135, 146–151]. At that time, some pioneering papers [53–57] discussed oxygen-induced degradation under light exposure and revealed the degradation mechanism to be deprotonation of methylammonium cations by superoxide (O_2^-), formed via the transfer of photogenerated electrons from perovskite to oxygen molecules. However, their study were carried out on complete solar cell devices, where limited information on the degradation of the actual perovskite layer was reported.

Therefore, we carried out the degradation experiments under precisely controlled oxygen levels (0-20 %) under 1 sun illumination. In order to understand the progression of oxygen induced degradation of bare perovskite films, we studied their optical, compositional and structural characteristics by UV-vis, PDS, XPS and SEM measurements. By completing the degraded films into solar cells, we correlated the degradation of active perovskite to the decay in photovoltaic performance. We utilised three deposition methods for fabrication of $CH_3NH_3PbI_3$ films, which allowed us to include the effects of perovskite microstructure on the progression of oxygen induced degradation.

4.3 Degraded Films in Oxygen under Illumination

The ETL (in most cases $PC_{61}BM$) in the inverted devices has been reported to serve as a blocking layer preventing oxygen diffusion [55, 152], whereas the metallic cathode could complicate the degradation by iodide diffusion [153, 154]. In another project, we studied the degradation of complete devices under light in various atmospheres and observed that the degradation rate in 20 % O_2 is comparable to in N_2, due to the protection of $PC_{61}BM$ from oxygen induced degradation [125]. Therefore, in order to study the progression of oxygen induced degradation on actual perovskite, we degraded $CH_3NH_3PbI_3$ films coated on ITO/PEDOT:PSS substrates for XPS, SEM and PV studies and on spectrosils for UV-vis and PDS measurements.

The $CH_3NH_3PbI_3$ films were fabricated by the $Pb(OAc)_2$, sol-eng and 1-1-1 recipes in a drybox (glovebox filled with dry air, RH $<$ 1.0 %) and directly transferred to a N_2-filled glovebox. Samples were then loaded into a sealed environmental box and exposed to various levels of O_2 under 1 sun illumination for 10 hours. The environmental box is flushed with N_2 and O_2, where oxygen levels were controlled by adjusting the relative flow rate of O_2 to N_2 and monitored throughout the experiment (Figure A1 in the Appendix shows an example of a degradation in 10 % O_2). Details about film preparation are described in Section 3.2.3.

4.3.1 Optical Properties

To probe the effect of degradation on the bulk properties of degraded films, UV-vis and PDS measurements were carried out. Figure 4.1a-c present the absorption of pristine and degraded perovskite films deposited on spectrosils using the $Pb(OAc)_2$, sol-eng and 1-1-1 recipes. Pristine films prepared by all three methods exhibit a clear onset at 780 nm from the perovskite film [4]. After degradation, the absorption of all films decreases with increasing oxygen concentration. In order to quantify the reduction in absorption, the evolution of absorbance at 700 nm is plotted in Figure 4.1d, with the 0 in the x-axis representing the pristine samples. Absorption of $Pb(OAc)_2$ films drops only slightly at low oxygen levels. When O_2 is above 12 %, the absorption decreases dramatically, together with the appearance of an onset at 520 nm which corresponds to the formation of PbI_2 [53, 55]. For sol-eng films, the absorption drops drastically even for low levels of oxygen and the PbI_2 onset is already present at 5 % O_2. The 1-1-1 recipe is the most stable, where the absorption of degraded films remains quite similar to the pristine and only starts to decrease slightly at 20 % O_2.

We performed PDS measurements to investigate the change in optical absorption edge and sub-band gap upon degradation [82, 84, 155–158]. Urbach energy (E_u), calculated by fitting the exponential increase in absorption at the band edge (fitting range: 1.50-1.58 eV), represents the degree of energetic disorder in the bulk films [96, 156, 159]. Figure 4.2 presents the Urbach energies of degraded perovskite films after exposure to light and oxygen for 10 h. The Urbach energy for degraded $Pb(OAc)_2$ samples is unchanged up to 10 % at around 18.5 meV, then rises to above 22.5 meV

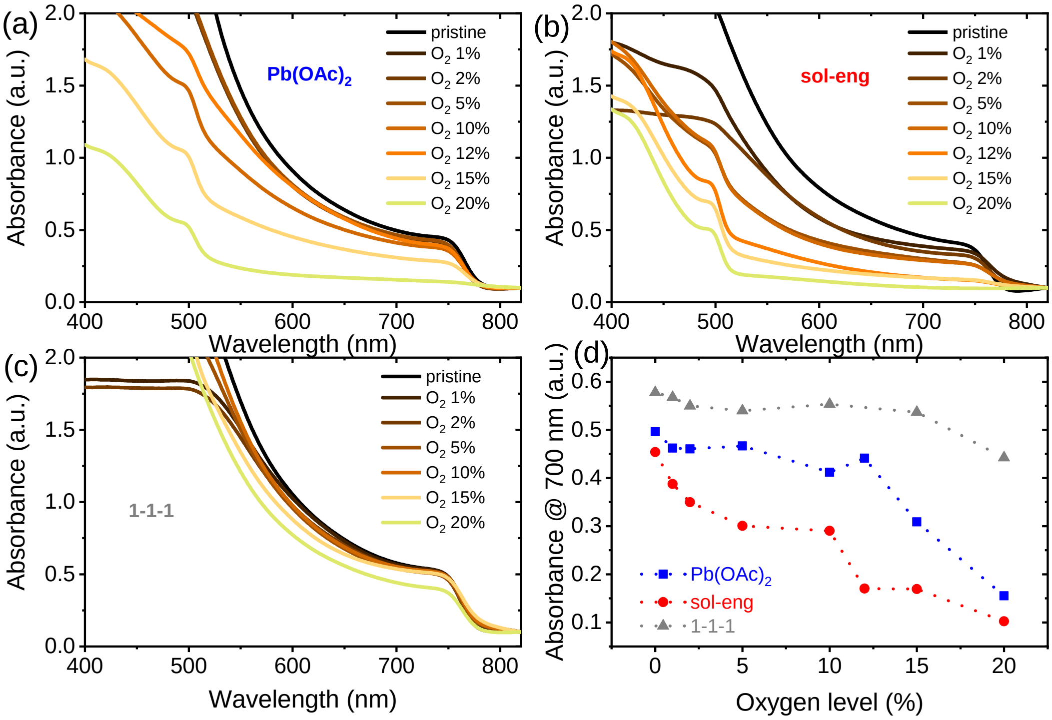

Figure 4.1: UV-vis measurements of degraded $CH_3NH_3PbI_3$ films for (a) $Pb(OAc)_2$, (b) sol-eng and (c) 1-1-1 on spectrosils. (d) Absorbance at 700 nm determined by (a-c) for degraded perovskite films. Adapted with permission from [58]. Copyright 2017, Wiley-VCH.

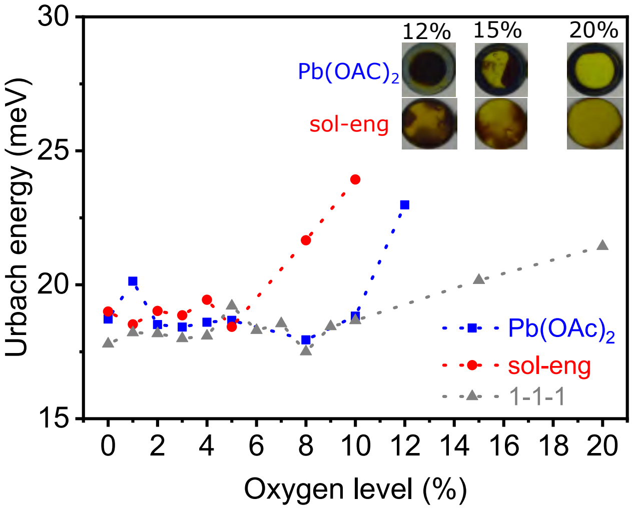

Figure 4.2: Urbach energies of degraded $CH_3NH_3PbI_3$ films for $Pb(OAc)_2$, sol-eng and 1-1-1 on spectrosils determined by PDS measurements. The measurements were performed by David Becker-Koch and Alexandra Bausch. Adapted with permission from [58]. Copyright 2017, Wiley-VCH.

at 12 % O_2 and cannot be determined from PDS spectra as films for levels above 12 % are dominated by PbI_2 (see pictures in inset of Figure 4.2 and the onset at 520 nm in Figure 4.1a). For the sol-eng degraded samples, E_u starts to increase at 8 % reaching around 22 meV, and continues to rise until 24 meV for 10 % O_2. Degraded samples convert to PbI_2 above 10 % O_2 and therefore no value could be determined, while for the 1-1-1 recipe, E_u remains around 18 meV up to 10 % O_2, increases slightly to 20 meV and 21 meV for 15 % and 20 %, respectively.

We noticed the discrepancy between the unchanged E_u and the fast reduction in the absorption of degraded sol-eng films at low oxygen levels. One possible explanation is that the Urbach energy draws information only about the sub-band gap absorption from perovskite, not the degradation by-products (e.g. PbI_2). Although the absorption intensity drops at low oxygen levels and possible early degradation by-products are formed, degraded films still exhibit high-quality perovskite domains suggested by the steep absorption onset, and therefore the charge carrier generation and separation remain quite efficient. At 8 % for sol-eng and 12 % for $Pb(OAc)_2$, Urbach energy rises as a result of the increased energetic disorder in the degraded films, which hampers the electronic properties of the final devices. For even higher oxygen levels, no onset could be determined for sol-eng and $Pb(OAc)_2$, as the films degraded to PbI_2 indicated by the dominating PbI_2 feature in absorption spectra.

4.3.2 Surface Compositional Properties

In order to investigate the degradation mechanism of perovskite, XPS measurements were performed. The chemical composition evolution is revealed by core level spectra of the main elements (I, Pb, N, C and O) for each degraded sample. As XPS is a surface sensitive technique that only probes the top 5-10 nm of the sample, all the following discussion is therefore focused on the surface properties of perovskite films.

Figure 4.3 presents the I3d and Pb4f XPS spectra collected from $CH_3NH_3PbI_3$ films fabricated by the $Pb(OAc)_2$, sol-eng and 1-1-1 recipes on ITO/PEDOT:PSS substrates, which had been degraded under constant simulated AM 1.5G solar illumination for 10 h at various oxygen levels. The I3d spectrum consists of $3d_{5/2}$ and $3d_{3/2}$ peaks, with a spin-orbit splitting of 11.5 eV. The binding energies of $I3d_{5/2}$ peaks for all the pristine films are 619.6 eV, consistent with the reported values from other groups [96]. The $I3d_{5/2}$ peak undergoes a slight shift towards higher binding energies upon degradation, which is monitored in all three recipes, suggesting a similar degradation process regardless of fabrication methods. The Pb4f spectrum consists of $4f_{7/2}$ and $4f_{5/2}$ peaks with a spin-orbit splitting of 4.9 eV. The binding energies of $Pb4f_{7/2}$ peaks for pristine and degraded perovskite films prepared by all three recipes are 138.6 eV, in good agreement with the values reported in literature [96]. Although some groups measured the metallic lead (Pb^0) peak at a lower binding energy (136.9 eV) on freshly prepared samples [48, 160], we observed no Pb^0 for all the pristine films. Small peaks of Pb^0 start to appear on the $Pb(OAc)_2$ perovskite films at an oxygen level of 5 % and on the sol-eng films at just 2 %. Samples made

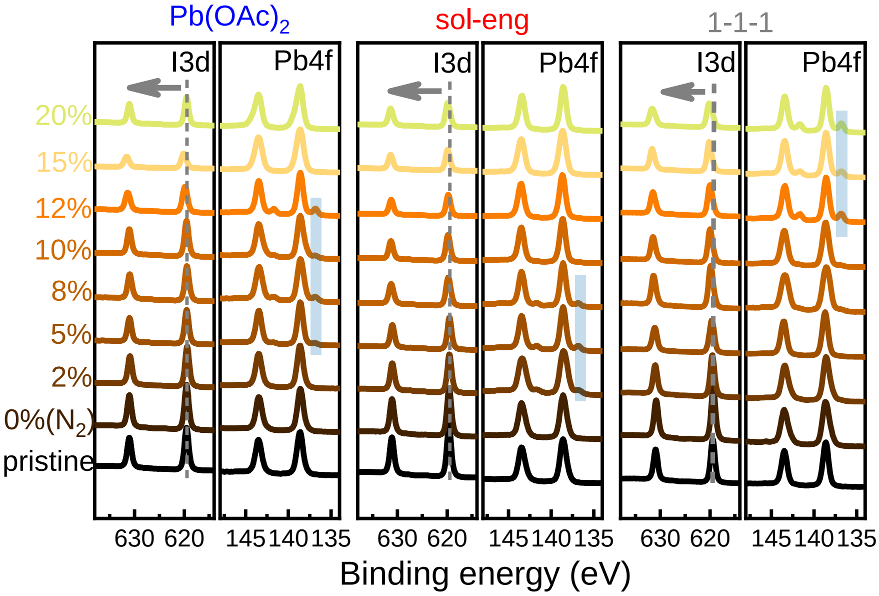

Figure 4.3: I3d and Pb4f spectra collected from X-ray photoemission spectroscopy measurements on pristine and degraded (10 h under various oxygen levels at 1 sun illumination) perovskite films fabricated using the $Pb(OAc)_2$, sol-eng and 1-1-1 recipes on PEDOT:PSS coated ITO substrates. Adapted with permission from [58]. Copyright 2017, Wiley-VCH.

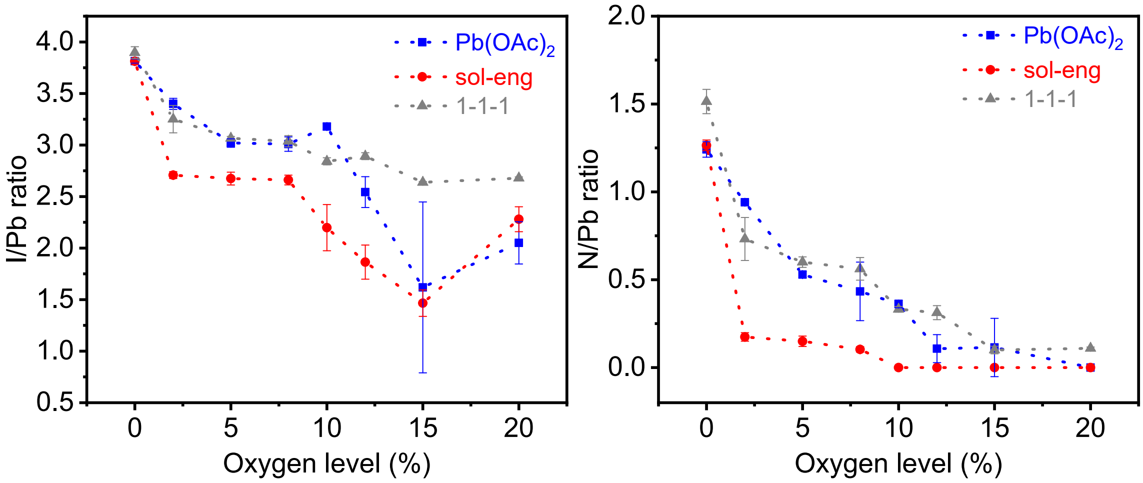

Figure 4.4: I to Pb (left) and N to Pb (right) ratio evolution calculated by X-ray photoemission spectroscopy measurements for degraded films fabricated using the $Pb(OAc)_2$, sol-eng and 1-1-1 recipes on PEDOT:PSS coated ITO. Adapted with permission from [58]. Copyright 2017, Wiley-VCH.

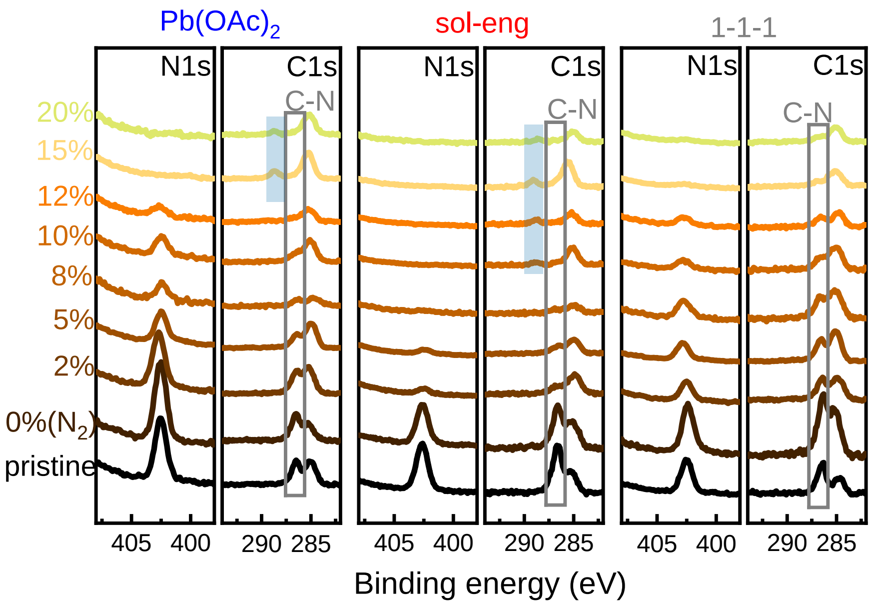

Figure 4.5: N1s and C1s spectra collected from X-ray photoemission spectroscopy measurements on pristine and degraded (10 h under various oxygen levels at 1 sun illumination) perovskite layers fabricated using the $Pb(OAc)_2$, sol-eng and 1-1-1 recipes on PEDOT:PSS coated ITO substrates. Adapted with permission from [58]. Copyright 2017, Wiley-VCH.

by the 1-1-1 recipe only start to show a small trace of Pb^0 at 12 %. The Pb^0 found here is possibly a degradation product in the early phase, as for higher oxygen levels, the previously observed metallic Pb is no longer present for $Pb(OAc)_2$ and sol-eng recipes.

By fitting the $Pb4f_{7/2}$ and $I3d_{5/2}$ peaks we can quantify the atomic percentages of Pb and I in the perovskite and their changes upon degradation. We calculate the I to Pb (I/Pb) ratio by dividing the atomic percentage of I over Pb. The I/Pb ratio for pristine samples is above 3, higher than the expected stoichiometry, due to residual methylammonium iodide on the surface. In the left panel of Figure 4.4, we monitor I/Pb ratio evolution upon degradation and observe a gradual decrease to below 2, suggesting another possible by-product (PbO_x) besides PbI_2. Films prepared by the 1-1-1 recipe show a less steep decline compared to samples prepared by the other two recipes. The I/Pb ratio for the $Pb(OAc)_2$ films decreases at a comparable speed as the 1-1-1 below 10 % O_2 and drops remarkably quickly at higher oxygen levels. The sol-eng recipe gives the least stable films in terms of I/Pb ratio, as it quickly drops to around 2.5 for 2 %-5 % O_2.

Figure 4.5 presents the N1s and C1s spectra collected from pristine and degraded $CH_3NH_3PbI_3$ films fabricated by the $Pb(OAc)_2$, sol-eng and 1-1-1 recipes. The C1s core level of the pristine perovskite films consists of two types C-bonds. One peak at

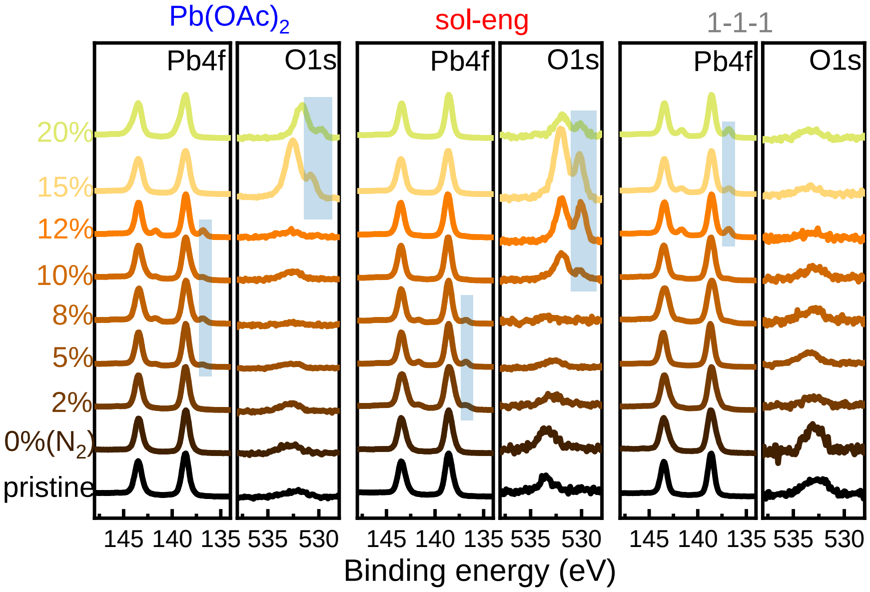

Figure 4.6: Pb4f and O1s spectra collected from X-ray photoemission spectroscopy measurements on pristine and degraded (10 h under various oxygen levels at 1 sun illumination) perovskite layers fabricated using the Pb(OAc)$_2$, sol-eng and 1-1-1 recipes on PEDOT:PSS coated ITO substrates. Adapted with permission from [58]. Copyright 2017, Wiley-VCH.

a lower binding energy (285.2 eV) represents the C-C and C-H bonds from surface contamination. The other peak, at a higher binding energy of 286.7 eV, is attributed to the C-N bond in the $CH_3NH_3^-$ cation. The corresponding peak in the N1s spectra is observed at 402.6 eV. During the degradation process the N1s core level intensity gradually decreases, coinciding with the disappearance of C-N bond, suggesting the loss of CH_3NH_2. We calculate the N to Pb (N/Pb) ratio and monitor its evolution under various oxygen levels, as presented in the right panel of Figure 4.4. The N/Pb ratio is above 1 for all the pristine films, due to the excess of methylammonium iodide on the surface mentioned previously. It consistently decreases until both N1s and C-N peaks disappear completely, for oxygen levels above 15 % in degraded Pb(OAc)$_2$ and 1-1-1 films. A sharp drop in the N/Pb ratio for the films prepared by the sol-eng recipe occurs at significantly lower oxygen levels—as low as 2 %. The drastic difference in the compositional evolution suggests a quite different rate of surface degradation among three methods.

Now we turn our attention to the O1s spectra (Figure 4.6). The O1s spectrum of pristine samples only contains one small peak at around 532 eV as a result of fabrication in the dry air environment. A second O1s peak at a lower binding energy (530.2 eV) only appears at high oxygen levels for films prepared by the Pb(OAc)$_2$ and sol-eng recipes. It is observed together with the increase in the intensity of the O1s peak around 532 eV. At the same time, N1s and C-N peaks (Figure 4.5) vanish and a new C1s peak at a higher binding energy (288.8 eV) that represents the oxidized carbon species (C=O, O-C=O) is detected. This second O1s peak can be attributed to the appearance of PbO_x during degradation process [161, 162], proposed by the ab initio studies by Zhang and Sit [163]. This result is consistent with the disappearance of Pb^0 for the $Pb(OAc)_2$ and sol-eng recipes at higher oxygen levels (Figure 4.3). There is no trace of a second O1s peak for the degraded 1-1-1 films, possibly suggesting a slower break down in the perovskite structure.

Haque and coworkers [53] report that superoxide generated in a light and oxygen environment causes the degradation of perovskite. Upon illumination, electron transfers from photoexcited perovskite to atmospheric oxygen and superoxide (O_2^-) is formed. O_2^- attacks the $CH_3NH_3PbI_3$, leading to the formation of methylamine (CH_3NH_2), PbI_2, I_2 and H_2O (Reaction 2.26). Zhang and Sit [163] show, based on their ab initio study, that peroxide (OOH^-) forms through the deprotonation of $CH_3NH_3^-$ cations by superoxide, destroying the Pb-I octahedral structure. At the same time Pb-O bonds are formed, together with the possible formation of I^+, O^{2-}, OH^- and local PbO structure. Ouyang et al. [164] further propose that the degradation products from the rapid surface oxidation, PbO and $Pb(OH)_2$, serve as a protective layer to prevent further oxidation of inner perovskite. The other oxidation product, H_2O, causes hydration-based degradation of the inner perovskite at a slower pace.

It is important to note that, even at low oxygen levels (2 %-5 %), although the surface of perovskite films is degraded as suggested by the loss of N and I (the drop in I/Pb and N/Pb in Figure 4.4), the perovskite under the surface is still intact and partly consists of high-quality perovskite structures, as indicated by the similar Urbach energies to the pristine (Figure 4.2).

We emphasize that the perovskite films degraded in the dark at 20 % oxygen for 24 hours (Figure A2 in the Appendix), or aged in N_2 under illumination for 10 h, do not show noticeable differences to the pristine, suggesting that perovskite is stable under these conditions. This observation demonstrates that oxygen alone does not cause degradation on this timescale, and therefore, the observed degradation is a consequence of both illumination and oxygen together, in good agreement with precious reports [55, 57, 165].

So far, all the discussions are focused on the perovskite sample coated on PEDOT:PSS. We also performed the same series of degradation and XPS studies for the $CH_3NH_3PbI_3$ films on bare ITO substrates. Figure A3, A4 and A5 in the Appendix present the XPS spectra collected from pristine and degraded $CH_3NH_3PbI_3$ films fabricated by the $Pb(OAc)_2$, sol-eng and 1-1-1 recipes on ITO substrates. In comparison to the films on PEDOT:PSS for the same recipe, the decrease in N1s and C-N peaks are much more dramatic, and the appearance of PbO_x starts at lower oxygen levels, indicating that rapid degradation is present without a PEDOT:PSS layer.

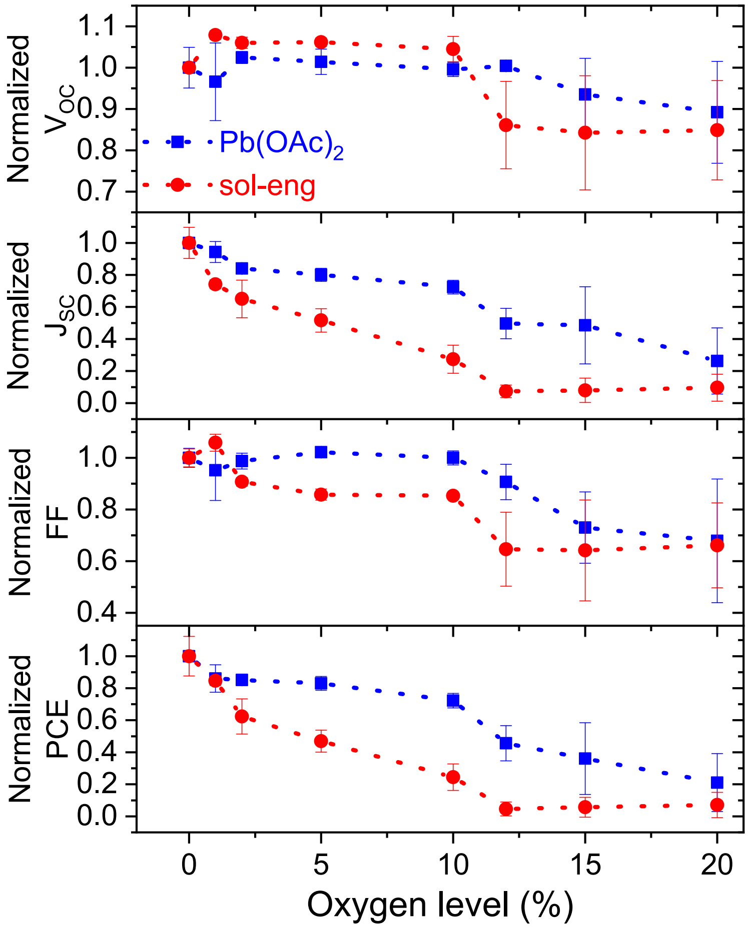

Figure 4.7: Solar cell characteristics of ITO/PEDOT:PSS/$CH_3NH_3PbI_3$/$PC_{61}BM$/BCP/Ag solar cells, with the bare perovskite films degraded for 10 h under various oxygen levels at 1 sun illumination, normalized to the values of the device degraded in N_2 atmosphere. Adapted with permission from [58]. Copyright 2017, Wiley-VCH.

4.4 Photovoltaic Performance of Degraded films

In this section, we focus only on the Pb(OAc)$_2$ and sol-eng recipes. The reason to leave out the 1-1-1 recipe is that it yields very thick perovskite films (approximately 650 nm), nearly three times thicker than the other two (around 275 nm). Since the oxygen-induced degradation starts at the surface, it takes a much longer time for thicker films to undergo the same oxidation process. This explains the stable optical properties, and the slowest degradation rate of the 1-1-1 recipe, compared to other methods. To avoid the possible influence of perovskite film thinness on the rate of degradation, we choose not to further discuss the 1-1-1 in the following sections.

In order to investigate the oxygen induced degradation on the photovoltaic performance, degraded films were transferred to a N_2-filled glovebox immediately following degradation, then completed with $PC_{61}BM$/BCP/Ag layers into fully functional so-

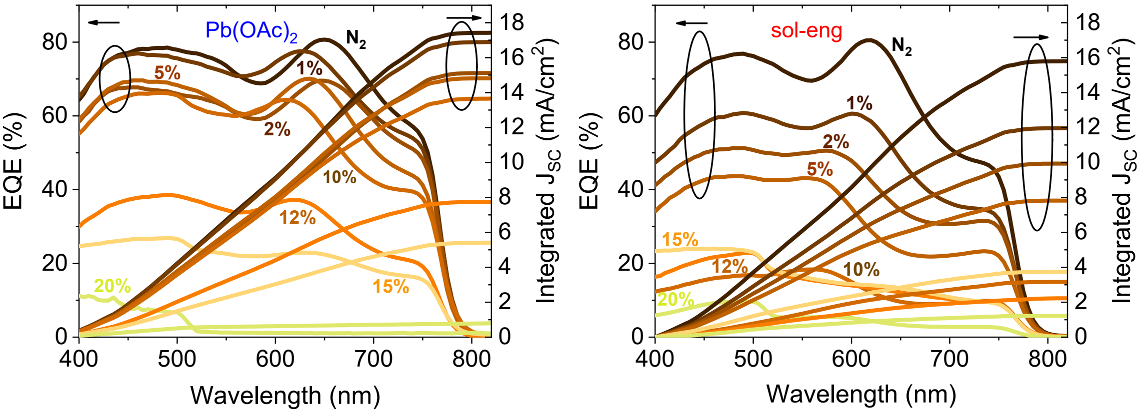

Figure 4.8: EQE spectra of the degraded $Pb(OAc)_2$ (left) and sol-eng (right) devices, respectively. Adapted with permission from [58]. Copyright 2017, Wiley-VCH.

lar cells, and tested under a solar simulator. The J-V characteristics and EQE spectra of the champion devices are presented in Figure A6 in the Appendix, with the statistics of PV parameters derived from more than 100 devices shown in Table B2. Both recipes result in hysteresis-free solar cells with stable power output (Figure A7 in the Appendix), thanks to the application of $PC_{61}BM$ as ETL [118, 123]. The highest PCEs for solar cells from the $Pb(OAc)_2$ and sol-eng recipes are 15.5 % and 10.5 %, respectively. Similar to the previous XPS results (Figure A2 in the Appendix), there is no obvious change in their PV performance compared to the pristine, when the perovskite films were kept in N_2 atmosphere under light for 10 h or stored in 20 % O_2 in the dark for 72 h (Figure A8 in the Appendix).

Figure 4.7 shows the evolution of the PV characteristics of the degraded devices, normalised to the performance of a device whose active layer was degraded for 10 h in nitrogen only atmosphere. Below 10 % O_2, V_{OC} and FF remain almost unchanged; the drop in PCE is mostly due to the reduction in J_{SC}. While the $Pb(OAc)_2$ devices exhibit relatively stable J_{SC}, the sol-eng devices start to show reduced J_{SC} at even 1 % O_2. When the oxygen level is above 10 %, V_{OC} and FF also start to drop. Sol-eng solar cells degrade much more significantly than $Pb(OAc)_2$, with a reduction in all parameters. The PCE of the sol-eng devices reaches nearly zero at 12 %, while $Pb(OAc)_2$ devices at 20 % O_2 still exhibit 25 % of their initial value. We observe a similar trend in EQE spectra (Figure 4.8) as in the J_{SC}. The drop in EQE of the sol-eng devices is more pronounced than in $Pb(OAc)_2$, and starts already at very low oxygen levels. The decrease of EQE across the whole visible range suggests the loss in absorption of the active perovskite layers, which is confirmed by the UV-vis results discussed previously.

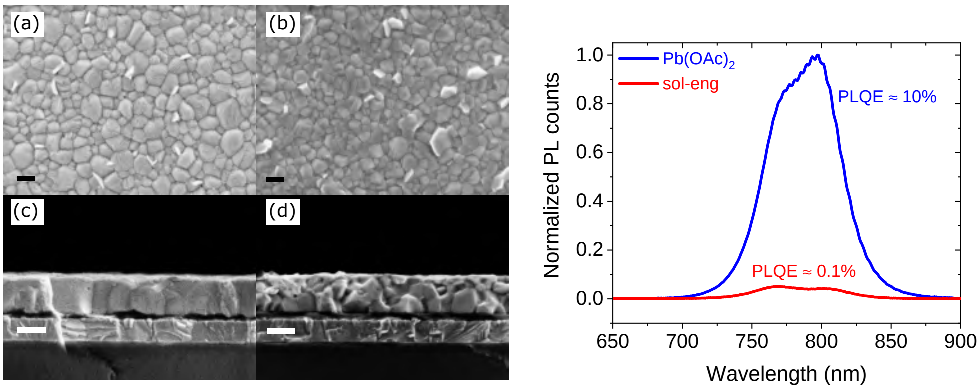

Figure 4.9: Left: Scanning electron microscopy top view and cross-section images of pristine perovskite films prepared by (a,c) Pb(OAc)$_2$ and (b,d) sol-eng recipes. Scale bars represent 200 nm. The measurements were carried out by Dr. Paul Fassl. Right: Photoluminescence spectra of Pb(OAc)$_2$ and sol-eng films prepared on spectrosils. The measurements were carried out by Alexandra Bausch. Adapted with permission from [58]. Copyright 2017, Wiley-VCH.

4.5 Discussion—Role of Microstructure

So far, we observe drastic differences in optical properties, surface composition and PV performance of degraded $CH_3NH_3PbI_3$ films prepared by the Pb(OAc)$_2$ and sol-eng methods, which yield perovskite films with highly different microstructures. AFM images (Figure A9 Appendix) of pristine Pb(OAc)$_2$ and sol-eng films coated on ITO/PEDOT:PSS substrates show that both recipes yield pinhole-free and compact films with low root-mean-squared surface roughness (9.36 nm for Pb(OAc)$_2$ and 11.97 nm for sol-eng). The top view SEM images in Figure 4.9 reveal large and regular-shaped grains for Pb(OAc)$_2$, and small and irregular gains for sol-eng samples. The cross-section images show that grains in Pb(OAc)$_2$ film protrude throughout the entire film, which allows the generated charges in perovskite to be transported within single grains. The sol-eng film consists of smaller grains that do not extend vertically through the perovskite film. They are relatively larger at PEDOT:PSS/perovskite interface but smaller at the surface, as a result of the antisolvent treatment [74, 166, 167]. The dramatic difference in PL intensity and PLQE value (Figure 4.9) between two methods also confirms great difference in their microstructure. Sol-eng films show a much reduced PL peak and only 0.1 % PLQE, while Pb(OAc)$_2$ films yields 10 % PLQE. Recent publications [168–173] suggest that the defects and traps at the surface and grain boundaries of perovskite crystals serve as recombination centres that cause the low PL intensity. As a result of smaller grains and a higher defect density [100, 174, 175], sol-eng devices exhibit a lower J_{SC} and FF in comparison to Pb(OAc)$_2$.

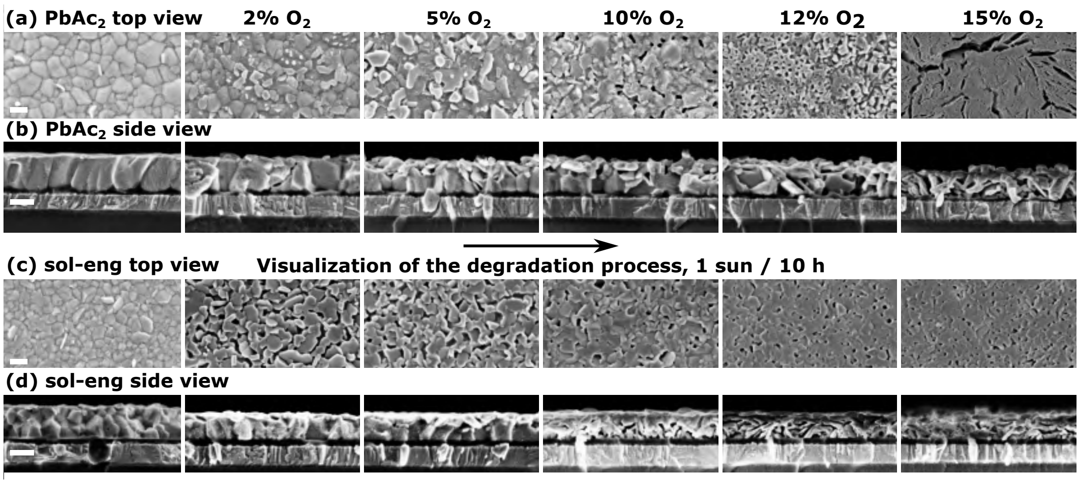

Figure 4.10: Scanning electron microscopy top view and cross-section images of perovskite films prepared by (a,b) $Pb(OAc)_2$ and (c,d) sol-eng recipes showing changes in morphology for different degradation states from left, degraded in N_2, to right, degraded in 15 % O_2, all for 10 h at 1 sun illumination. Scale bars represent 200 nm. The measurements were carried out by Dr. Paul Fassl. Adapted with permission from [58]. Copyright 2017, Wiley-VCH.

4.5.1 Evolution of Microstructure in Degradation

The degradation process was monitored by recording SEM images of the surface and cross-section of degraded ITO/PEDOT:PSS/$CH_3NH_3PbI_3$ films at various oxygen levels. These experiments were performed by Dr. Paul Fassl. Figure 4.10 presents the different evolutions in the morphology of degraded perovskite films prepared by the $Pb(OAc)_2$ and sol-eng recipes. It must be noted that this figure only gives a rough visualization of the degradation process. Since the size of the shown SEM images is $1.8\,\mu m \times 0.9\,\mu m$, the small sections here are only representative areas for each sample, not the whole film. Films degraded in N_2 do not show any sign of degradation. For $Pb(OAc)_2$ films up to 10 % O_2, the grain structure is still identifiable, except for the appearance of smaller structures at the surface and the formation of gaps in the cross-section images. For 10 % and 12 % O_2, small holes appear in the top view images, and they penetrate into and damage the film under the surface, as shown in the cross-section images. For 15 % O_2, the morphology alters completely and the layer becomes thinner, suggesting complete conversion to PbI_2. These results are in good agreement with the PV studies, where degraded $Pb(OAc)_2$ devices still possess 80 % of the initial performance up to 10 % O_2, after which complete deterioration.

For sol-eng films, at only 2 % and 5 % O_2, the grain structure at the surface is already different. As revealed by the cross-section images, the film is about 40-50 nm thinner, but the grains underneath remain pristine. For 10 % and higher oxygen levels, the gaps between grain structures appear, and the entire film is degraded and

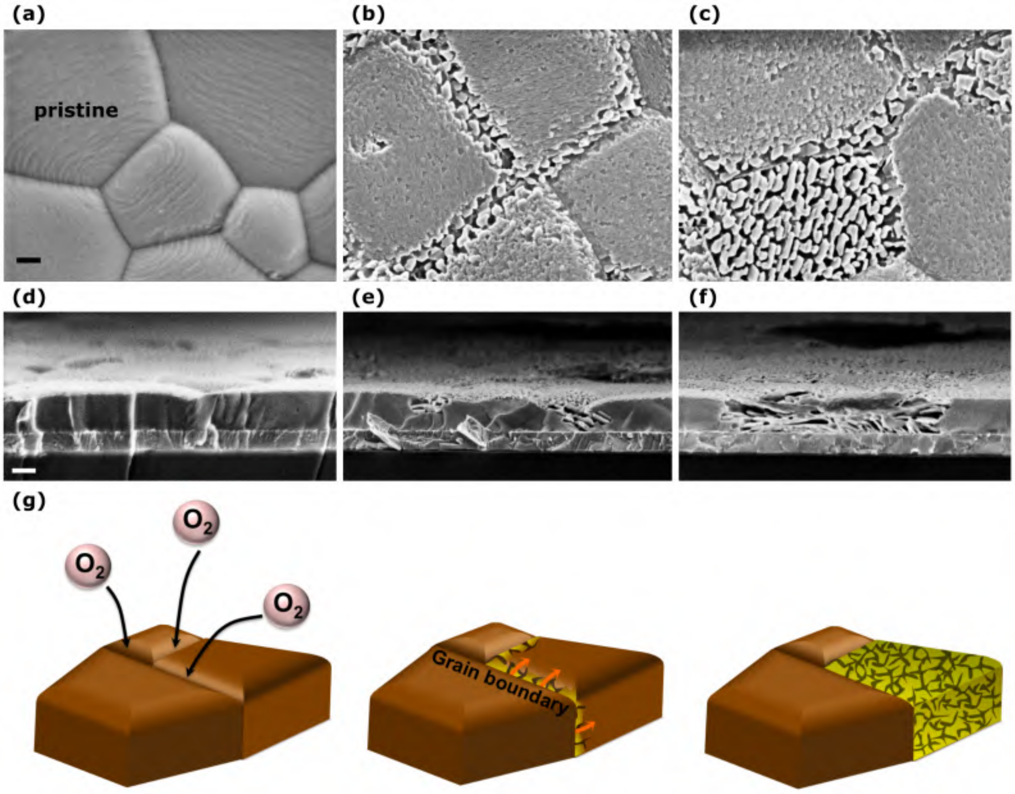

Figure 4.11: Scanning electron microscopy top view and cross-section images of $Pb(OAc)_2$ on ITO: (a,d) pristine layers, (b,e) initial stages of degradation, and (c,f) later stages of degradation. The scale bars represent 200 nm. (g) Illustration of the progression of oxygen induced degradation from the grain boundaries. The measurements were carried out by Dr. Paul Fassl. The cartoon in (g) was provided through the courtesy of Prof. Yana Vaynzof. Reproduced with permission from [58]. Copyright 2017, Wiley-VCH.

converted to PbI_2. These results are consistent with the previous observation of a severely degraded surface at low oxygen levels (by XPS) but still intact grains in the bulk by UV-vis and PDS measurements. The rapid degradation at the surface of sol-eng samples explains the drop in J_{SC} at very low oxygen levels, while reasonable Voc and FF are maintained by the high-quality perovskite grains in the bulk. The reduction in J_{SC} is related to the loss in absorption and increasing recombination pathways due to the degradation by-products [29, 176, 177].

4.5.2 Role of Grain Boundaries

The observation that smaller grains degrade faster indicates that the oxygen induced degradation is related to the grain size, and possibly the grain boundaries. To investigate this, we monitored the degradation progress of larger perovskite grains.

By depositing $Pb(OAc)_2$ films directly on ITO substrates, we increased the grain size to several micrometers, thanks to the non-wettability of the precursor solution on ITO [114]. Figure 4.11 presents top view and cross-section images of pristine and degraded films at 5 % oxygen. At the early stages of degradation, the surface of the grains become rougher, and small holes and gaps start to appear at grain boundaries, suggesting that the degradation is initialized at the surface and grain boundaries. Later, the degradation extends to entire grains. However, some grains are still intact, while others are strongly altered. The fact that degraded films still possess some mostly intact grains explains the decent photovoltaic performance in the degraded samples. The whole progress of degradation is illustrated in Figure 4.11g. Previous studies have shown that density of defects is considerable larger at the surface and grain boundaries than in the interior regions of the grains [169, 171, 172, 178–180]. Oxygen molecules are able to infiltrate more easily in these areas of higher defect density, generating superoxide that leads to further degradation, which is in agreement with our observation of the fast-degrading sol-eng films, which exhibit small grains, and therefore, more grain boundaries and a high defect density, confirmed by the low PL and PLQE.

4.6 Conclusions

In this chapter, we systematically degraded $CH_3NH_3PbI_3$ films prepared by various methods, with different microstructures, in controlled oxygen atmospheres under 1 sun illumination. Using UV-vis, PDS, XPS, PV and SEM measurements, we demonstrate that the microstructure of perovskite films has a tremendous effect on the oxygen and light induced degradation. Our study shows that perovskite films with small, irregular grains and high defect density degrade much faster and more severely than films with large uniform grains and better electronic properties. Therefore, the stability of perovskite films, or devices, can be improved in oxygen and light by producing high-quality perovskite films with large uniform grains and reduced defect density. We also reveal that the light and oxygen induced degradation occurs even at low oxygen levels, which emphasizes the importance of avoiding unnecessary light exposure during device fabrication in non-inert atmospheres, in order to reduce the degradation occurring during the production phase.

5 Effects of Large-Scale Compositional and Electronic Inhomogeneities on Device Performance

5.1 Overview

This chapter is based on our recent publication in the journal of ACS Applied Energy Materials with the title 'Large-Scale Compositional and Electronic Inhomogeneities in $CH_3NH_3PbI_3$ Perovskite and Their Effect on Device Performance' [140]. Most graphs are reproduced or adapted with permission from the American Chemistry and Materials Society. The SEM measurements in this chapter were performed by Dr. Paul Fassl.

5.2 Introduction

Since the first application of hybrid organic-inorganic halide perovskite solar cells in 2009 [3], significant work has been devoted to enhance the PCE of perovskite solar cells via optimization of the perovskite composition [6, 8, 65, 155, 181–183] and film morphology [25, 29], and also by improving the adjacent transport layers [184, 185]. Early publications often only reported the maximum PCE of the champion solar cells [3, 5, 186–189]. Recently, researchers have started to pay more attention to the statistics of photovoltaic device performance parameters [29, 74–76, 190]. A wide distribution in PCE, up to 6-7 %, was reported in most studies from 2013 to 2017 (left panel of Figure 5.1). In order to monitor our statistics of device performance, we fabricated and measured a set of 8 samples with 8 pixels on each (in total of 64 solar cells) under identical conditions, with the structure of ITO/PEDOT:PSS/$CH_3NH_3PbI_3$/$PC_{61}BM$/BCP/Ag. As presented in the right panel of Figure 5.1, we observed large variations in solar cell performance in the entire batch (black line) of all 64 devices, comparable with previous studies from different groups. We also noticed variation in the pixels from individual devices (8 coloured lines), where both the average and standard deviation of PCE differ from sample to sample.

Although we can attribute the differences in the reported photovoltaic performance distribution from different groups to different fabrication methods and conditions [25, 128, 191–193], the origin of the wide distribution within single studies remains unclear and merely mentioned. In addition to the wide distribution in the performance of the perovskite devices, different IP values (from 5.1 to 6.6 eV)

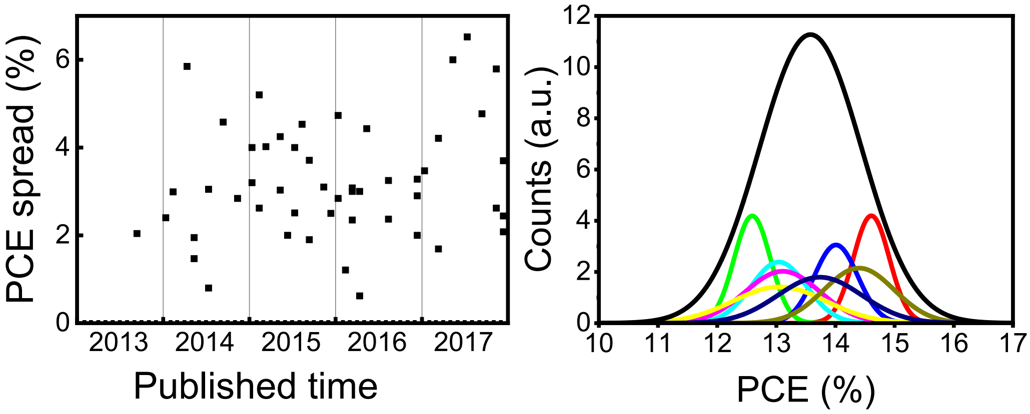

Figure 5.1: Left: PCE spread (i.e., $PCE_{max} - PCE_{min}$) reported in 50 representative studies (for a detailed list of references, see Table B3 in the Appendix) from 2013 to 2017. Right: Variation in PCE of eight identical devices ($8 \times 8 = 64$ pixels) from one batch (black line), as well as distributions among eight pixels from each device (coloured lines). Lines displayed are the Gaussian fit to each distribution. The actual histograms of all eight devices are shown in Figure A10a. Adapted with permission from [140]. Copyright 2018, American Chemical Society.

are reported in the literature for the same perovskite $CH_3NH_3PbI_3$ [92–97]. The work from Olthof's group examined the origin of the various reported IP values and consequently the device performances [194]. They performed UPS and XPS measurements on $CH_3NH_3PbI_3$ films fabricated by deliberately varying the precursor composition ratio and with different deposition methods. UPS studies show that IP is significantly altered as a result of the variation in surface composition (i.e., N/Pb ratio) observed by XPS studies. The photovoltaic performance is enhanced when an optimized energy level alignment between the perovskite film and adjacent transport layers is obtained by varying the IP of perovskite, due to a higher accessible open-circuit voltage (V_{oc}) and more efficient charge transport [94, 195–198]. However, single XPS and UPS measurements are limited by the acquisition point size. As a result, IP values of certain spots on the film cannot represent the electronic structure of the whole sample. Therefore, a single-point photoemission spectroscopy experiment is insufficient to provide the full information about the surface compositional and electronic properties of the whole film.

Therefore, we performed XPS and UPS mapping experiments on perovskite films across a 7.2 mm × 7.2 mm area in the centre of a 12 mm × 12 mm sample, which covers the active areas of the eight pixels of the final device (see illustration in Figure A10b). Details about the mapping experiments are explained in the section 3.3.8. We observed large surface compositional and electronic variations between identically fabricated samples, and furthermore, a divergent extent of inhomogeneity across single samples. By employing three fabrication recipes for perovskite deposition, we show that these variations are not limited to certain fabrication methods.

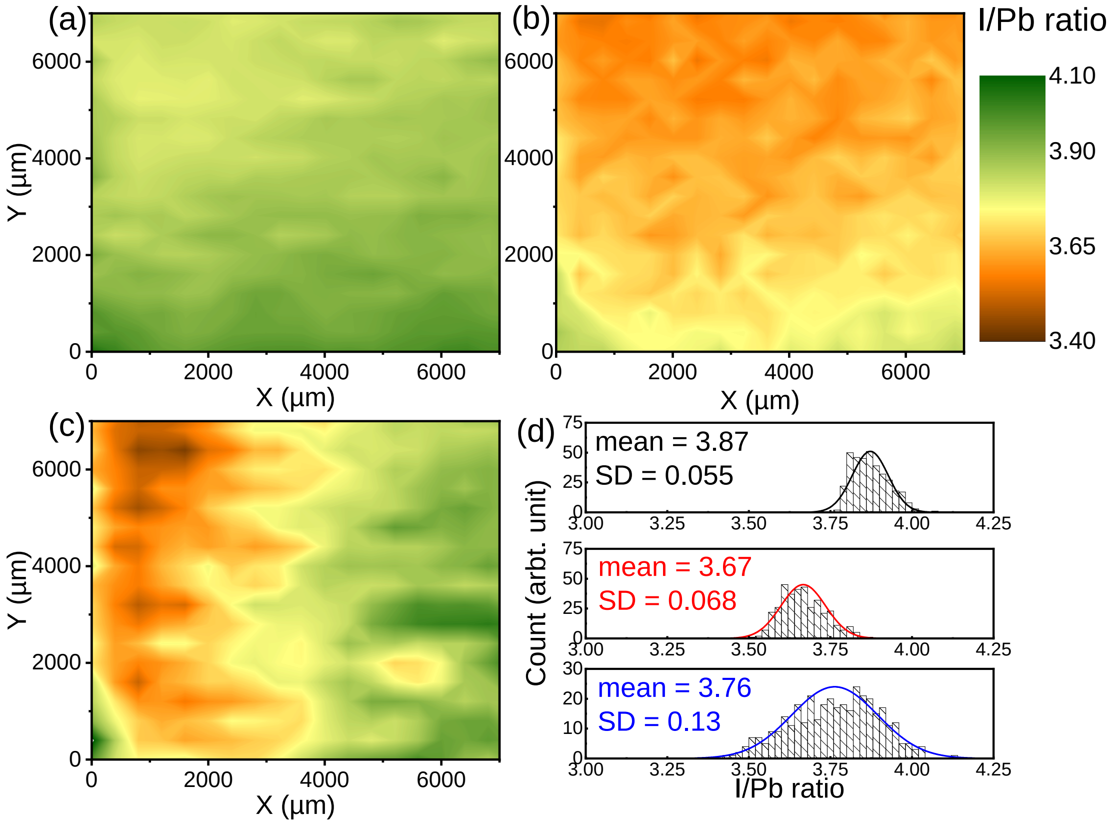

Figure 5.2: I/Pb maps of perovskite samples produced by the $Pb(OAc)_2$ recipe, where (a) is a uniform film, (b) is quite uniform but with a different average I/Pb ratio, and (c) is a film with a very high inhomogeneity. (d) Histograms of the I/Pb ratio distribution of these three samples (black, sample in panel (a); red, sample in panel (b); blue, sample in panel (c)). Adapted with permission from [140]. Copyright 2018, American Chemical Society.

XPS and UPS mapping experiments performed on the same samples reveal a correlation between compositional and electronic inhomogeneities. Lastly, we completed the films into solar cells and were able to correlate the distribution of the photovoltaic performance to the degree of electronic inhomogeneity.

5.3 XPS and UPS Mapping

5.3.1 I/Pb Maps

To probe the surface compositional properties of the entire sample, we performed two-dimensional XPS mapping experiments across the measured $CH_3NH_3PbI_3$ films, where a serial acquisition of 324 XPS measurements are carried out, with an X-ray

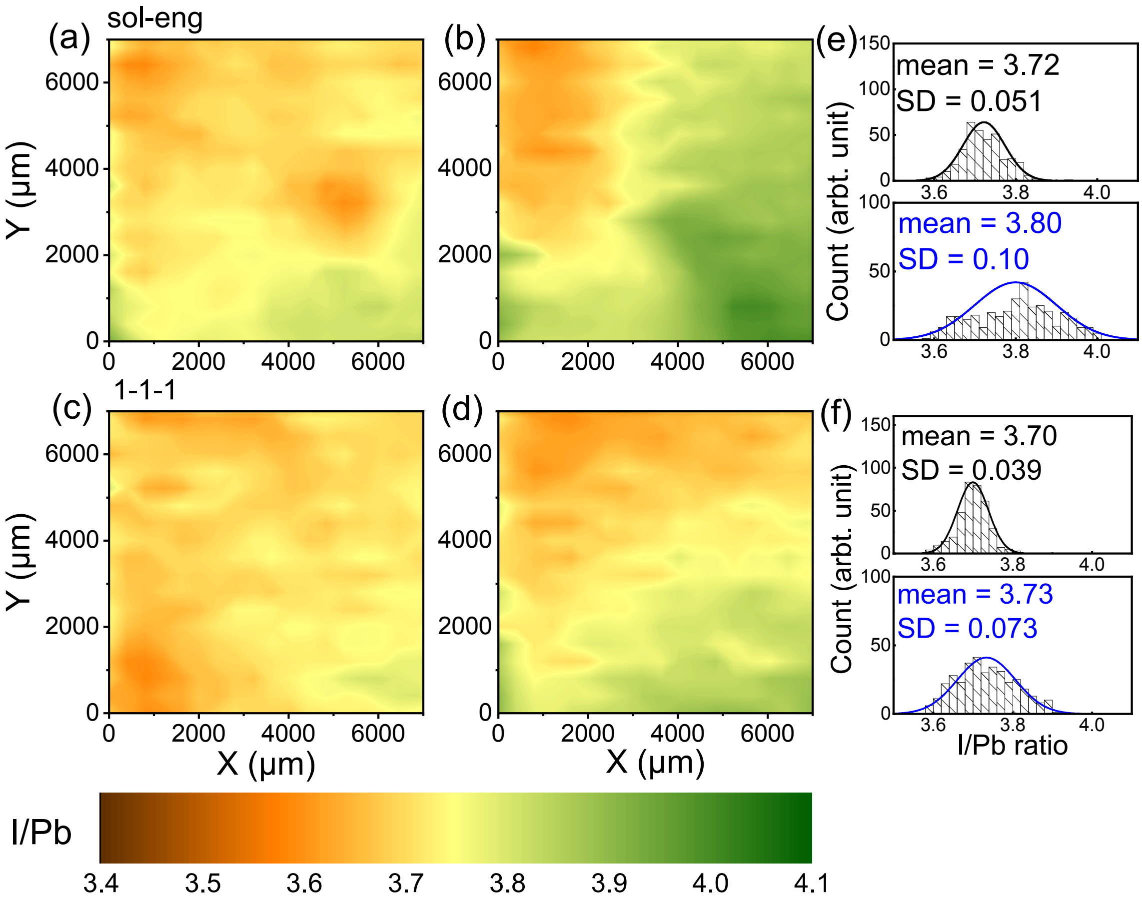

Figure 5.3: I/Pb maps of perovskite films produced by different recipes: (a) uniform and (b) inhomogeneous films produced by the sol-eng recipe; (c) uniform and (d) inhomogeneous films produced by the 1-1-1 recipe. Corresponding histograms of I/Pb ratio distribution of (e) sol-eng and (f) 1-1-1 samples. Adapted with permission from [140]. Copyright 2018, American Chemical Society.

spot size of 400 μm and step size of 400 μm. At each measurement point, Pb 4f and I 3d spectra are collected, and the I/Pb ratio is then calculated from the ratio of the atomic percentages of iodine and lead. An I/Pb map summarizes the distribution of the I/Pb ratio across the sampled area as a two-dimensional colour contour plot, with x- and y- axes representing the probed position, and the colour difference representing the changes in surface composition.

Figure 5.2 presents I/Pb maps of three $CH_3NH_3PbI_3$ films on ITO/PEDOT:PSS substrates prepared by the $Pb(OAc)_2$ recipe under identical conditions. The first two samples (Figure 5.2a,b) are relatively uniform, but have different average values of I/Pb ratio. In contrast, the third film (Figure 5.2c) exhibits large compositional inhomogeneities across the surface. Histograms of the I/Pb ratio distribution (Figure 5.2d) illustrate the clear differences amongst them. In order to show that the observed compositional inhomogeneities are not limited to certain fabrication methods, I/Pb maps of samples prepared by the sol-eng and 1-1-1 recipes are presented in Figure 5.3. Similar to the $Pb(OAc)_2$ films, uniform (Figure 5.3a,c) or inhomogeneous samples (Figure 5.3b,d) can be produced by the sol-eng and 1-1-1 recipes under identical conditions as well.

5.3.2 IP maps

In order to monitor the electronic properties of the entire sample, UPS mapping experiments were performed in a similar fashion to the XPS mapping. UPS spectra were collected across the sample with a measurement spot size of around 400 μm. At each probed spot, the work function was acquired by measuring the difference between the cut-off binding energy obtained from the secondary photoemission onset, and the Fermi Level of the spectrometer determined by a standard gold sample (Equation 3.8). The IP is, then obtained by the sum of the work function and the difference between Fermi level and the valence band edge, as determined from the x-intercept of the linear fit of valence band onset (Equation 3.9). An IP map (two-dimensional colour contour plot with colour changes representing the IP variations) depicts the distribution of electronic structure across the sampled area.

Figure 5.4 presents IP maps of two representative samples prepared by both the $Pb(OAc)_2$ and sol-eng recipes. Similar to the XPS mapping results, despite the identical fabrication recipe and process, some films are relatively uniform (Figure 5.4a,c), while others exhibit large-scale inhomogeneities in electronic properties (Figure 5.4b,d). It is important to note that the perovskite films prepared by the sol-eng (Figure 5.4c,d) and 1-1-1 recipe (Figure 5.5) tend to be more inhomogeneous than $Pb(OAc)_2$ recipe. A droplet-like feature is observed in the inhomogeneous IP maps of sol-eng (Figure 5.4d) and 1-1-1 films (Figure 5.5b), which can attributed to the effect of antisolvent dropping on the wet film during the fabrication process, suggesting clearly different electronic properties at this dripping spot compared to the rest of the film. Therefore, recipes employing antisolvent quenching methods are more likely to form energetically inhomogeneous samples.

We note a correlation between the surface chemical compositional inhomogeneities

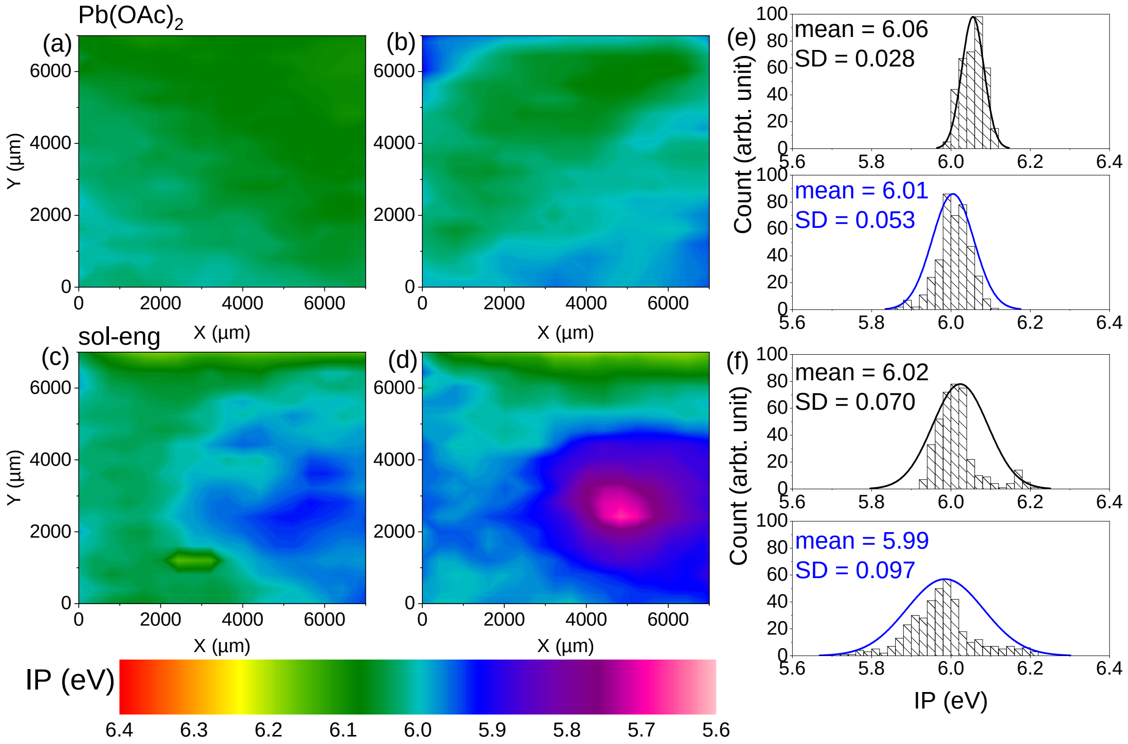

Figure 5.4: IP maps of perovskite films produced by different recipes: (a) uniform and (b) inhomogeneous films produced by the $Pb(OAc)_2$ recipe; (c) uniform and (d) inhomogeneous films produced by the sol-eng recipe. Corresponding histograms of IP distribution of (e) $Pb(OAc)_2$ samples and (f) sol-eng samples. Adapted with permission from [140]. Copyright 2018, American Chemical Society.

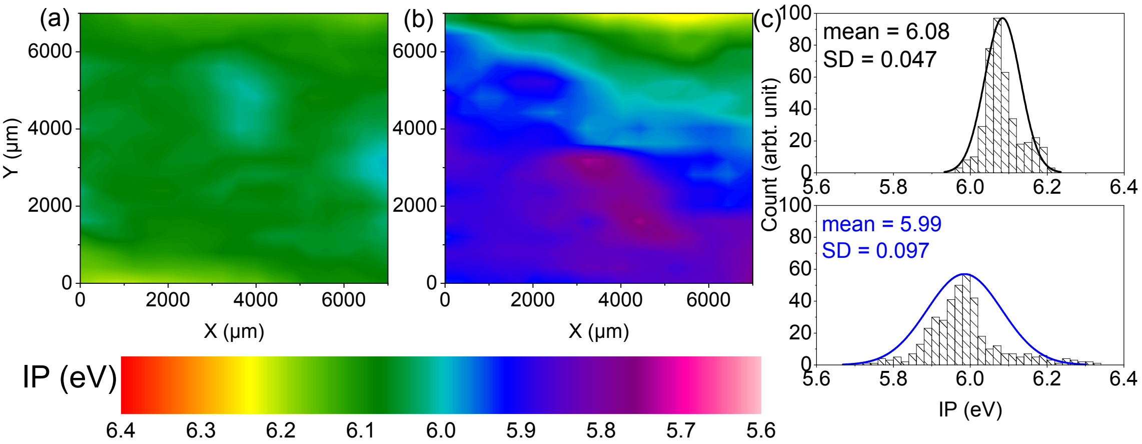

Figure 5.5: IP maps of (a) uniform and (b) inhomogeneous perovskite films prepared by the 1-1-1 recipe. (c) Histograms of the IP distribution of sample (a) and (b). Note the spot in panel (b) resulting from the deposition of the antisolvent during film fabrication. Adapted with permission from [140]. Copyright 2018, American Chemical Society.

and the variation in the electronic properties. Figure A19 in the Appendix shows a linear-like correlation between the standard deviations of IP and I/Pb, where the XPS and UPS mapping were carried out on the same region of the same sample, indicating that samples with a large compositional variation tend to be more inhomogeneous in electronic properties.

5.3.3 Influence of Storage Conditions

To study the effect of storage conditions after fabrication on the surface composition, we stored compositionally inhomogeneous perovskite films in three different conditions (N_2-filled glovebox, dry air filled glovebox and vacuum (10E-10 mbar, same as the photoemission spectroscopy experiments)) for 50 hours, and carried out XPS mapping experiments afterwards. Figure A16 in the Appendix shows that the I/Pb maps of the $Pb(OAc)_2$ films stored in N_2 and dry air remain unchanged in both I/Pb ratio and its distribution, while the I/Pb value is dramatically reduced over the entire sample for the films kept in vacuum. A similar reduction in I/Pb across the entire sample is observed for the sol-eng and 1-1-1 perovskite films stored in vacuum as well (Figure A17, Appendix). This decrease in I/Pb can be attributed to the loss of methylammonium iodine from perovskite surface as a result of long-time vacuum exposure [199]. In order to minimize the effect of exposure to vacuum on the mapping results, we kept the XPS and UPS mapping measurement time of a single sample to below 1.5 h.

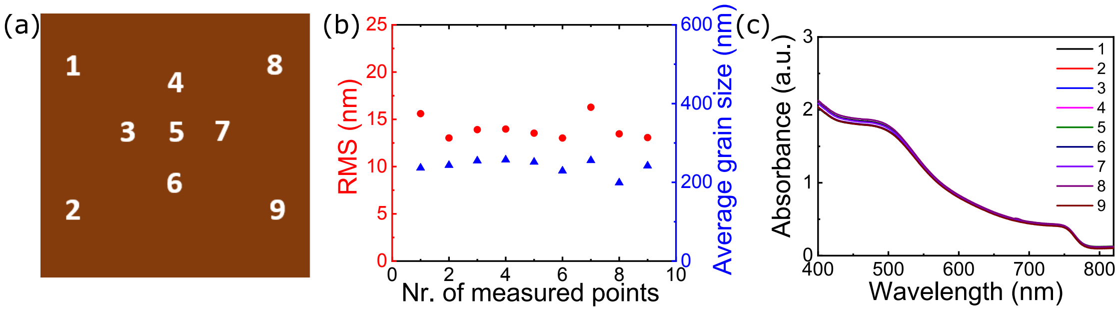

Figure 5.6: (a) Illustration of nine different spots on the sample where AFM, SEM and UV-vis measurements are carried out. (b) Roughness and average grain size of an inhomogeneous perovskite film produced by the $Pb(OAc)_2$ recipe measured at various spots, calculated from AFM measurements. (c) Absorbance spectra of an inhomogeneous perovskite film produced by the $Pb(OAc)_2$ recipe measured at various spots. Adapted with permission from [140]. Copyright 2018, American Chemical Society.

5.3.4 Possible Causes for the Surface Inhomogeneities

Microstructure, Absorption or Phase Impurities?

In order to investigate the microstructural variation across the perovskite samples, we carried out AFM and SEM measurements on nine different spots across the perovskite film (Figure 5.6a). As presented in Figure 5.6b, for perovskite films prepared by the $Pb(OAc)_2$ recipe on ITO/PEDOT:PSS substrates, the root-mean-square roughness and average grain size (obtained from AFM measurements) show no obvious difference at different spots across the film, in good agreement with the unchanging grain structures in SEM images (Figure A11, Appendix). Figures A13 and A14 in the Appendix further demonstrate that the microstructure of perovskite films prepared by the sol-eng and 1-1-1 recipes also remain unchanged across the sample. Therefore, the compositional inhomogeneities at the film surface are not related to variations in the microstructure of perovskite samples. We also measured the UV-vis absorption of the perovskite at different points. As presented in Figure 5.6c and A12, the absorption remains unaltered across the film for all three recipes, suggesting that the observed inhomogeneities are unrelated to the changes in absorption. It is important to note that the surface compositional inhomogeneities are not the result of phase impurities, indicated by the X-ray diffraction spectrum of $Pb(OAc)_2$ film (Figure A15, Appendix), as no residual PbI_2 or lead acetate is detected.

Fabrication Conditions

The impact of solvent atmosphere during perovskite fabrication on the crystal formation and film morphology has already been discussed in literature [186, 191, 200], which possibly affects the chemical composition at the surface of perovskite films. The perovskite layers were solution-deposited in a spin-coater with a closed lid located in a dry air filled glovebox. It is likely that the surface compositional

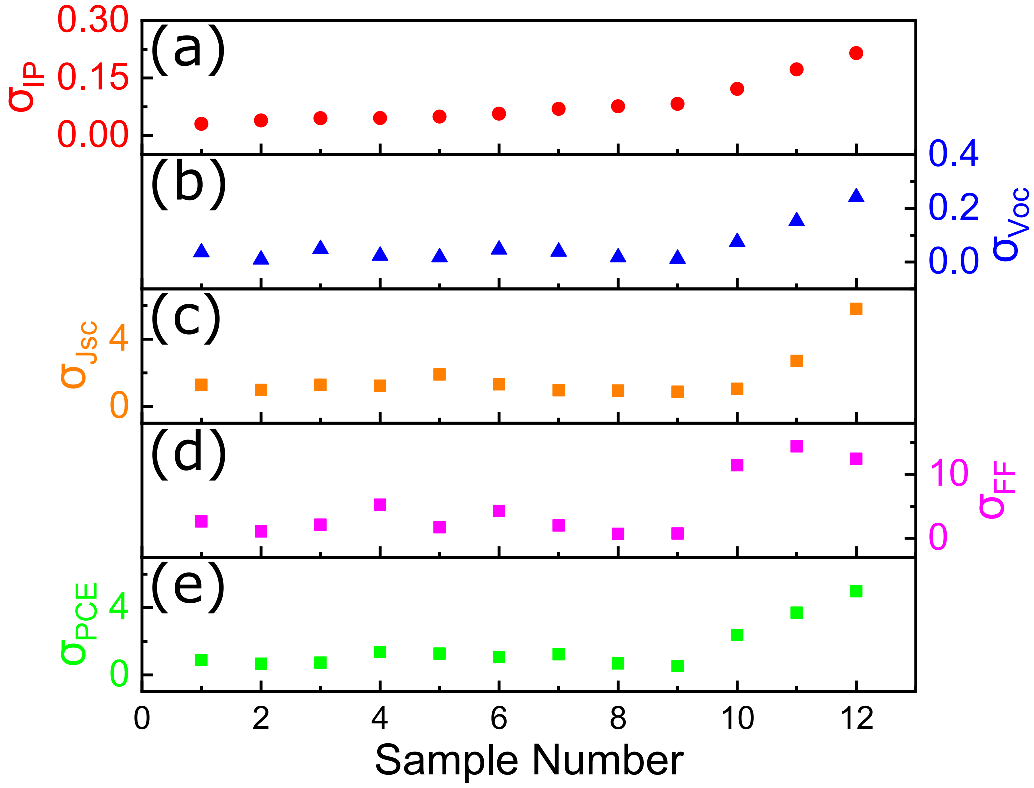

Figure 5.7: (a) Standard deviation of IP (σ_{IP}) derived from UPS mapping experiments of 12 perovskite films, which afterwards were completed into solar cells and measured under AM1.5 G simulated sunlight ($100\,\mathrm{mW/cm^2}$). Standard deviation of V_{OC} (b), J_{SC} (c), FF (d), and PCE (e) extracted from J-V measurements of the corresponding solar cell devices. Reproduced with permission from [140]. Copyright 2018, American Chemical Society.

inhomogeneities are related to the fact that films cannot be prepared in identical environmental conditions. For example, the first sample is prepared in the atmosphere with the lowest solvent vapor concentration, and samples coated later face a higher solvent vapor concentration atmosphere than the previous ones, since residual solvent from the precursor solutions cannot easily escape the spin-coater and continuously form a solvent bath inside. The variations observed across the sample could also be attributed to uneven annealing of the perovskite films, possibly induced by temperature gradient across the heating plates, or by the fact that some region of the sample touches the heating plate earlier due to manual handling errors.

5.4 Effect on Device Performance

To investigate the influence of electronic inhomogeneities on the photovoltaic performance, perovskite films prepared by the $Pb(OAc)_2$ recipe were completed with

$PC_{61}BM$/BCP/Ag into fully functional solar cells following the UPS mapping experiments and tested under a solar simulator. Since the observed inhomogeneities are not limited to certain fabrication methods, this study was carried out using only the $Pb(OAc)_2$ recipe. Average device parameters and standard deviations of all twelve devices are listed in Table B4 in the Appendix, with the J-V curves of their champion pixels shown in Figure A18 in the Appendix. We calculated standard deviations of V_{OC}, J_{SC}, FF and PCE for each sample to quantify their degree of inhomogeneity in photovoltaic performance. As presented in Figure 5.7, there is a clear correlation between the standard deviations of IP and device performance parameters. Samples with a narrow distribution in ionization potential (Sample nr. 1-9) exhibit a small performance variation, while the electronically inhomogeneous perovskite films (sample nr. 10-12) result in devices with widespread PV parameters.

It has been reported that the IP of the perovskite film influences the built-in potential in the final photovoltaic device and consequently the accessible V_{OC} [194]. As a result of the unchanged absorption across the perovskite film, the band gap remains the same; however, the observed variation in the IP suggests corresponding changes in the electron affinity (i.e., the conduction band position of perovskite) across the film. This in turn affects the energetic alignment at the perovskite/$PC_{61}BM$ interface, and consequently the electron extraction efficiency and V_{OC} [94, 195–198]. Some publications have shown that the IP of perovskite layers also affects the hole blocking and charge carrier recombination efficiency at the perovskite/$PC_{61}BM$ interface [201, 202]. The differences in the charge carrier extraction and blocking efficiency explain the observed changes in the J_{SC} and FF, despite the uniform microstructure and unchanged absorption across the sample. The wide spread in PCE observed in our study and by other groups (Figure 5.1 left panel) is hence the combined result of these factors.

5.5 Conclusions

In this chapter, large-scale chemical compositional and electronic inhomogeneities of $CH_3NH_3PbI_3$ films are observed with XPS and UPS mapping experiments. By analysing perovskite films prepared by different fabrication methods, we demonstrate that these inhomogeneities are not limited to certain recipes, and are therefore commonly observed by other research groups as well. Our study shows that the extent of the variation in PV parameters across the entire sample are related to the extent of the observed inhomogeneities, which explains the wide spread of device performance reported in the literature. Therefore, in order to obtain devices with reliable and reproducible performance, more attention should be devoted to improving the perovskite fabrication process, in order to obtain an active layer with a uniform surface composition and electronic properties. Additionally, our results highlight the importance of studying the surface properties of perovskite layers, instead of simply focusing on bulk properties such as microstructure and absorption.

6 The Relationship between Antisolvent Type and Dripping Speed, Determining the Device Performance

6.1 Overview

This project was performed in collaboration with Dr. Alex Taylor, who inspired the project idea and contributed to the samples fabrication and device characterisation (J-V measurements). The SEM and optical microscope measurements in this chapter were carried out by Dr. Fabian Paulus and Maximilian Litterst, respectively.

6.2 Introduction

Solution-processed perovskite has drawn great attention in the photovoltaic community, as it ensures highly efficient solar cell at a low manufacturing cost. One of the most employed fabrication methods uses an antisolvent dripping technique during spin coating the perovskite precursor solution on the substrate. It results in high-quality perovskite films that yield reproducible solar cells with efficiencies over 22 % [8, 65]. Since the introduction of this technique in 2014 [74, 85], the choice of antisolvents in early times were always among toluene [74], diethyl ether [75] and chlorobenzene [8, 87]. Interestingly, these three solvents produce high-quality perovskite films with high photovoltaic efficiencies, despite their different physiochemical properties (such as boiling point and polarity (Table B5 in the Appendix)). Recently, three promising new candidates, namely ethyl acetate [88], anisole [90] and trifluorotoluene [89], were reported to yield champion efficiencies of 19.4 %, 19.8 % and 20.3 %, respectively.

Although diethyl ether has been reported to result in a rapid crystallization of high-quality pinhole-free $CH_3NH_3PbI_3$ perovskite film [75, 203], it does not seem to work well for the $(FAPbI_3)_{0.85}(MAPbBr_3)_{0.15}$ perovskite. Bu et al. reported a poorly functioning device using diethyl ether, due to its low boiling point [88]. Paek et al. also showed that pinholes are present on the surface of films treated with diethyl ether [89]. They proposed that only the DMF/DMSO miscible solvents with a high boiling point (such as trifluorotoluene, toluene and chlorobenzene) assure a smooth and complete perovskite film, which yields much enhanced device performance in comparison to the immiscible solvents (e.g. xylene and diethyl ether).

It is interesting to notice that there are no clear/standard requirements for a ‘good’ antisolvent, and a ‘poor’ antisolvent for some compositions might work great on other occasions. Therefore, we elucidate this issue with a systematic study comparing a large number of solvents in the following sections. In addition, parameters of the antisolvent application such as the dripping time [204] and the antisolvent volume [90] have been well studied, whereas the influence of the antisolvent dripping speed on the perovskite formation and its device performance has been merely discussed. Hence, we also compare two different dripping speeds (i.e., fast and slow) of a series of solvents and reveal the relationship between the antisolvent and its dripping speed, and their effects on the device performance.

6.3 The Relationship between Antisolvent type and Dripping Speed

We employed thirteen different solvents: ethanol (EtOH), 2-propanol (IPA), 1-butanol (BuOH), ethyl acetate (EA), chloroform (CF), chlorobenzene (CB), butyl acetate (BA), 1,2-dichlorobenzene (DCB), anisole (Ani), trifluorotoluene (TFT), diethyl ether (DE), m-xylene (XYL) and toluene (Tolu). Their chemical structures are presented in Figure A20 with the physiochemical properties listed in Table B5 in the Appendix. These 13 solvents not only contain the widely used popular antisolvents (e.g. CB and Tolu), but also include some traditionally considered 'poor' solvents (e.g. EtOH, IPA and DE), in addition to some solvents which were never reported as the antisolvent (e.g. CF).

6.3.1 Device Performance

In order to investigate the relationship between the antisolvent and its dripping speed, we fabricated $Cs_{0.05}(MA_{0.17}FA_{0.83})_{0.95}Pb(I_{0.9}Br_{0.1})_3$ (CsMAFA) perovskite solar cells with the device architecture of ITO/PTAA/PFN-P_2/CsMAFA/$PC_{61}BM$/BCP/Ag and compared the resulting PV performance of two dripping speeds (fast and slow) using 13 different antisolvents. Their J-V characteristics and statistics are presented in Figure 6.1. The other parameters, such as dripping time and volume of the applied antisolvent were kept the same. (Fabrication details are described in Chapter 3.2.3.)

It is clear that the antisolvent dripping speed influences the perovskite device performance to different extents, depending on which antisolvent was employed during the fabrication of perovskite film. Therefore, we categorise these 13 antisolvents into three types based on the different device performances between fast and slow antisolvent application.

Methanol (MeOH) (type 0) does not produce a photoactive black perovskite film due to its high solubility of organic precursors [85]. The first type (type I) contains three antisolvents: EtOH, IPA and BuOH. They belong to the alcohol group, which has a hydroxyl functional group (-OH) bound to a carbon atom. Devices whose perovskite films were prepared with a fast dripping of the type I antisolvents obtain a higher V_{OC}, J_{SC}, FF and PCE with narrower distributions, in comparison to the

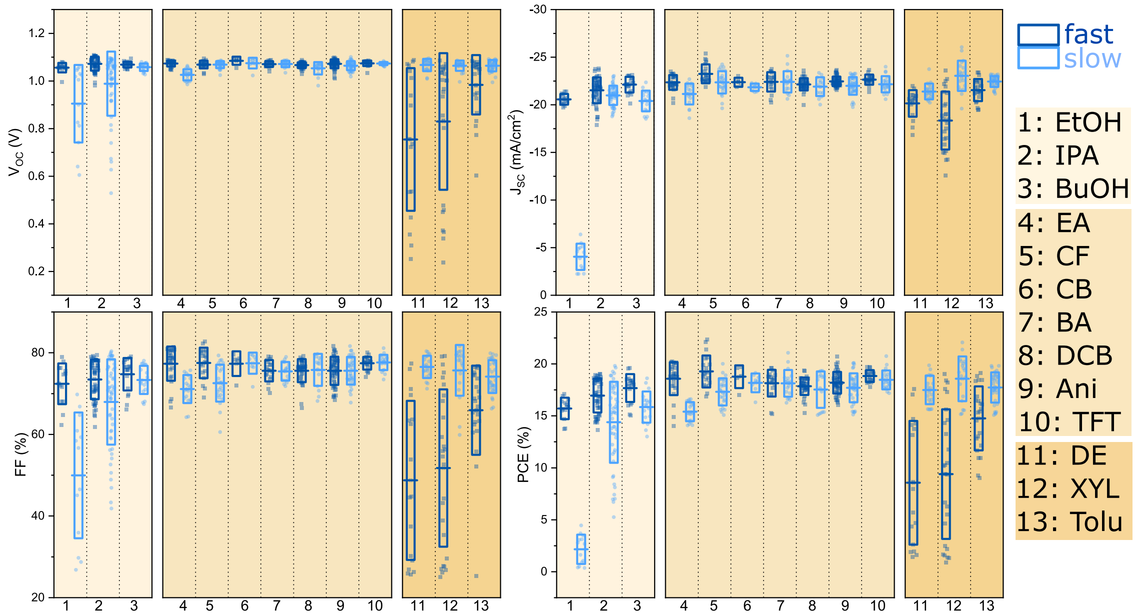

Figure 6.1: Solar cell characteristics of ITO/PTAA/PFN-P_2/CsMAFA/$PC_{61}BM$/BCP/Ag solar cells, with the perovskite films fabricated using 13 different antisolvents with fast (dark blue) and slow (light blue) dripping speeds. The used antisolvents are EtOH, IPA, BuOH, EA, CF, CB, BA, DCB, Ani, TFT, DE, XYL and Tolu, from 1 to 13.

devices fabricated by a slow antisolvent dripping. The difference in the PV performance between the fast and slow dripping speeds varies from extremely different to relatively comparable for EtOH, IPA and BuOH, respectively. This can be attributed to the continuous decrease in the solubility of organic precursors (i.e., MAI and FAI), which is further elaborated in Section 6.4. The solar cell fabricated by a slow EtOH dripping has a PCE of less than 5 % with a low J_{SC} below $7\,mA/cm^2$, suggesting the formation of a poor-quality perovskite absorbing layer. This is confirmed by the non-stoichiometric chemical composition by its XPS measurements (Section 6.3.2) and also by its SEM images (Section 6.3.3).

For the type II antisolvents, namely EA, CF, CB, BA, DCB, Ani and TFT, the PV performance is not affected by the antisolvent application speed with a PCE around 20 %. Therefore, the type II solvents are promising candidates, as it does not require a specific dripping speed to ensure the formation of high-quality perovskite films and well-functioning devices. However, there is a slight variation among device performances using different antisolvents. The use of EA and CF yields devices with slightly different PV parameters between fast and slow dripping speeds, while devices employing TFT as the antisolvent obtain comparable and reproducible PV performance, regardless of dripping speed. Further discussion is elaborated in Section 6.4.

The type III category consists of DE, XYL and Tolu. The devices using this type antisolvents behave the opposite to the type I: perovskite solar cells fabricated by a slow antisolvent dripping are more efficient with improved reproducibility, in comparison to these using a fast application. Possible explanations are discussed in Section 6.4.

6.3.2 Surface Chemical Composition

To make sure that the perovskite layer contains the correct stoichiometry, we carried out XPS measurements on CsMAFA films fabricated using 13 antisolvents with fast and slow dripping speeds coated on ITO/PTAA/PFN-P_2 substrates. Five acquisitions were taken at five different spots of each sample. As XPS is a surface sensitive technique that only probes the top 5-10 nm of the sample, all the following discussion is therefore focused on the surface properties of perovskite films.

By fitting the $Pb4f_{7/2}$ and $I3d_{5/2}$ peaks from their XPS spectra we can quantify the atomic percentages of Pb and I in the perovskite. We calculate the I to Pb (I/Pb) ratio by dividing the atomic percentage of I over Pb. The Br to Pb (Br/Pb), Cs to Pb (Cs/Pb), FA to Pb (FA/Pb) and MA to Pb (MA/Pb) ratios are obtained in a similar way. The N1s spectrum of the CsMAFA perovskite contains two peaks at around 400.6 eV and 402.9 eV representing the FA and MA, respectively (Figure A21a in the Appendix). The peak positions are consistent with the reported values from other groups [205]. The atomic percentages of FA and MA are quantified by fitting the corresponding N1s peaks. The theoretical values of the I/Pb, Br/Pb, Cs/Pb, FA/Pb and MA/Pb ratios based on the precursor concentration are listed in the Table 6.1. Note that FA contains two nitrogen atoms; therefore, the theoretical

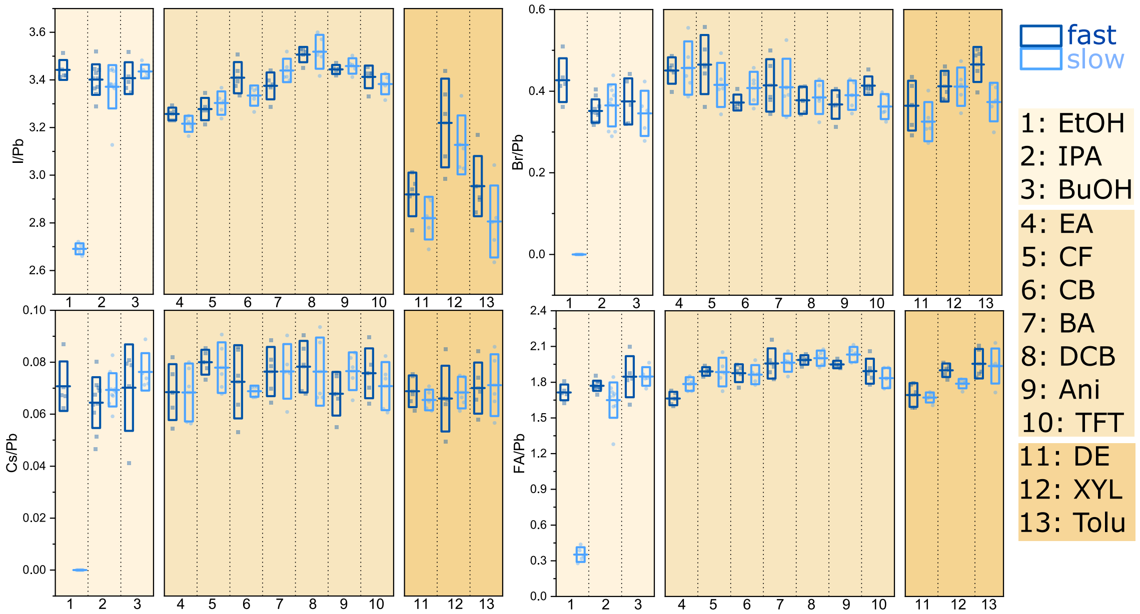

Figure 6.2: The I/Pb, Br/Pb, Cs/Pb and FA/Pb ratios of CsMAFA perovskite films fabricated using 13 antisolvents with fast (dark blue) and slow (light blue) dripping speeds on ITO/PTAA/PFN-P_2 substrates. The used antisolvents are EtOH, IPA, BuOH, EA, CF, CB, BA, DCB, Ani, TFT, DE, XYL and Tolu, from 1 to 13.

ratio of FA/Pb is 1.58, not 0.79. As shown in Figure A21a (Appendix), the N1s peak assigned to MA is low and noisy, which makes it difficult to perform a neat fitting with small errors. As a result, there is a large variation in the MA/Pb ratio among different acquisition spots on every single sample (Figure A21b, Appendix).

Figure 6.2 presents the I/Pb, Br/Pb, Cs/Pb and FA/Pb ratios of perovskite layers fabricated using 13 different antisolvents with fast and slow dripping speeds.

Table 6.1: Theoretical values of the I/Pb, Br/Pb, Cs/Pb, FA/Pb and MA/Pb ratios.

ratio(theo)	I/Pb	Br/Pb	Cs/Pb	FA/Pb	MA/Pb
	2.7	0.3	0.05	1.58	0.16

For the perovskite samples prepared by these antisolvents, the calculated I/Pb and FA/Pb ratios are approximately 30 % higher than the theoretical values, except for the film fabricated by a EtOH slow dripping. These high ratios indicate the presence of residual FAI on the surface, proposed by Philippe et al. [205]. In addition, there is a slight enrichment in the Br/Pb and Cs/Pb ratios for these samples, which is also the consequence of the excess FAI on the sample surface [205].

The perovskite film fabricated using a slow EtOH dripping contains a much reduced I content, together with no traces of Br nor Cs. Moreover, it exhibits nearly zero percentage of MA and a much lower FA amount. These findings indicate the

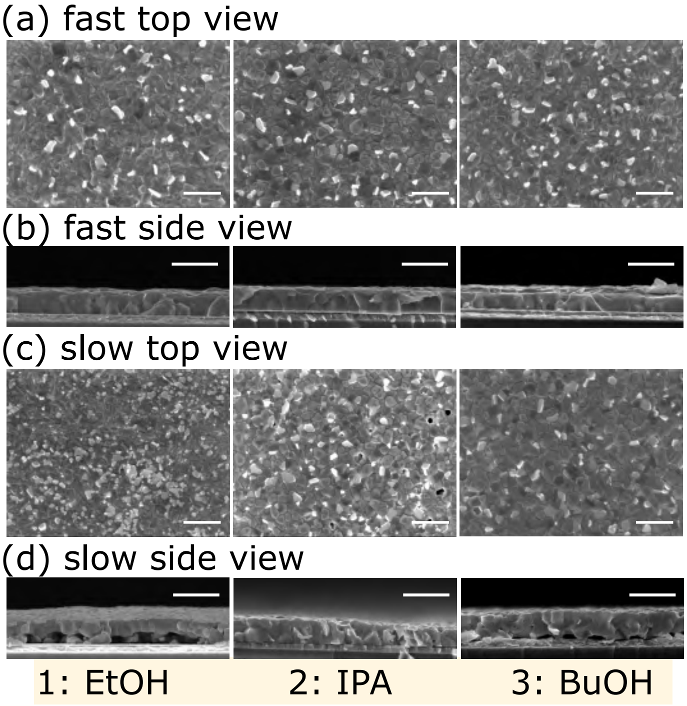

Figure 6.3: Scanning electron microscopy top view and cross-section images of the CsMAFA perovskite films fabricated by dripping the antisolvent fast (a,b) and slow (c,d). The antisolvents used are EtOH, IPA and BuOH, from left to right. Scale bars represent 1 μm. The measurements were carried out by Dr. Fabian Paulus.

presence of PbI_2, rather than the CsMAFA perovskite. Consequently, the devices prepared using a slow EtOH dripping exhibit a PCE below 5 % with much reduced J_{SC} and FF.

6.3.3 Microstructure

In order to monitor the influence of antisolvent type and dripping speed on the perovskite microstructure, we recorded SEM top view and cross-section images of CsMAFA perovskite films fabricated using 13 antisolvents with fast and slow dripping speeds on ITO/PTAA/PFN-P_2 substrates. These experiments were performed by Dr. Fabian Paulus and are presented in Figure 6.3, 6.4 and 6.5.

Figure 6.3 demonstrates the clear difference in the microstructure of the perovskite films on the top surface and also at the PTAA/PFN-P_2/perovskite interface prepared using the type I antisolvents with different dripping speeds. The white content in the top view images are PbI_2 phases [206]. It is clear that the perovskite film prepared by a EtOH slow dripping exhibits many more PbI_2 phases than the one produced with a fast dripping. Moreover, the EtOH slow sample exhibits a different grain structure on the surface and in the bulk. As revealed by its cross-section

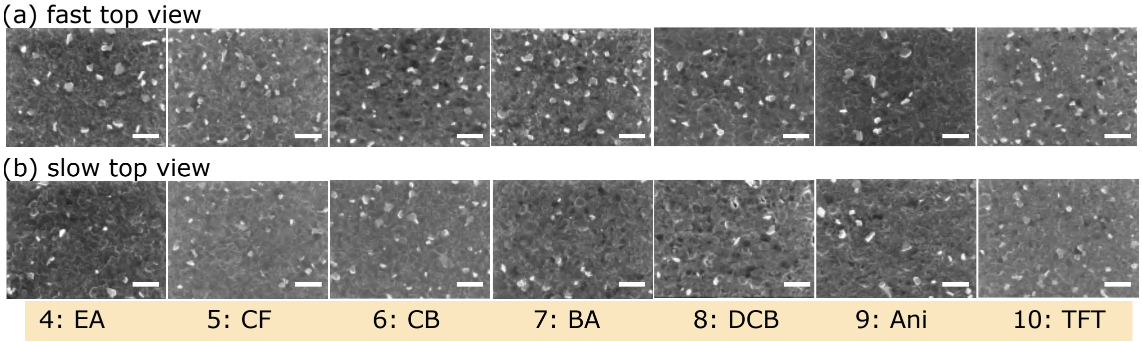

Figure 6.4: Scanning electron microscopy top view images of the CsMAFA perovskite films fabricated by dripping the antisolvent fast (a) and slow (b). The antisolvents used are EA, CF, CB, BA, DCB, Ani and TFT, from left to right. Scale bars represent 1 μm. The measurements were carried out by Dr. Fabian Paulus.

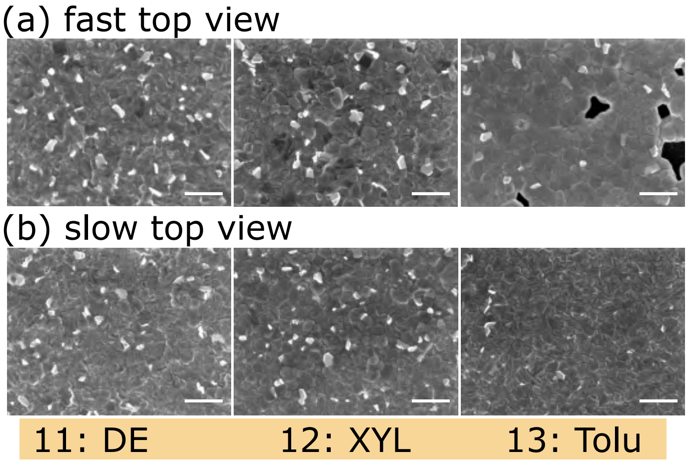

Figure 6.5: Scanning electron microscopy top view images of the CsMAFA perovskite films fabricated by dripping the antisolvent fast (a) and slow (b). The antisolvents used are DE, XYL and Tolu, from left to right. Scale bars represent 1 μm. The measurements were carried out by Dr. Fabian Paulus.

image, ‘cave’-like structures are present at the PTAA/PFN-P_2/perovskite interface, suggesting an incomplete film coverage at this interface. We observe a similar trend when using IPA and BuOH as the antisolvent. The perovskite films prepared by fast dripping are dense and complete, while the slow application results in a slight increase of PbI_2 phases and incomplete film coverage with either holes penetrating through the whole layer (IPA) or caves present at the PTAA/PFN-P_2/perovskite interface (BuOH).

The top view and cross-section images of the perovskite films fabricated using type II antisolvents with different dripping speeds are presented in Figure 6.4 and A22 (Appendix). All the perovskite films prepared using type II antisolvents are pinhole-free and compact, with comparable grain sizes and less PbI_2 phases. The dripping speed of type II antisolvents does not affect the perovskite microstructure, nor the amount of the PbI_2 phases.

Figure 6.5 and A23 (Appendix) show the top view and cross-section images of the perovskite films fabricated using type III antisolvents with different dripping speeds. Many fewer PbI_2 phases are present in comparison to the films fabricated employing type I antisolvents. Note that it is difficult to form a complete perovskite film using a fast antisolvent dripping, as hinted at by the SEM image of the Tolu fast sample in Figure 6.5 and the optical microscope images in Figure A24a in the Appendix. When the type III antisolvent is applied fast, the photoactive black perovskite forms only in the middle, close to where the antisolvent droplet hits the sample, while regions closer to the edges exhibit a completely different microstructure. Perovskite films prepared by a slow dripping of the type III antisolvents are pinhole-free and compact.

6.4 Discussion

So far, we have reported that there are three types of antisolvents, each resulting in different device performance with different dripping speeds. For the first type, only fast application of the antisolvent ensures a pinhole-free and compact perovskite film. As a result, the devices prepared by fast dripping exhibit improved PV performance with narrower distributions than those with a slow dripping. For the type II antisolvents, the dripping speed is not as crucial as for the first type, as PV performance is not significantly altered when the antisolvents are applied fast or slow. The type III antisolvents work exactly opposite to the type I. Perovskite devices prepared using a fast dripping perform poorly with a large PV performance variation, whereas the solar cells prepared by a slow dripping exhibit comparable PV parameters to the type II antisolvents. This is likely the reason why some of the type III antisolvents were regarded as ‘poor’ choices for the fabrication of perovskite films in the literature (e.g. DE and XYL) [88, 89], because the researchers might have applied the antisolvent too rapidly.

In order to investigate the reasons why the dripping speed has quite different effects on device performance for these three types of antisolvents, we carried out a solubility test of MAI in all antisolvents (Figure 6.6). The MAI solubility test

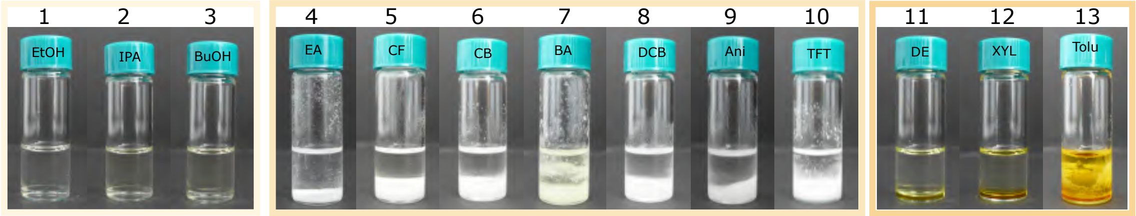

Figure 6.6: Pictures of different solution mixtures, where 13 antisolvents were added to the MAI solution (2M in DMF/DMSO) at a volume ratio of 6:1. The used antisolvents are EtOH, IPA, BuOH, EA, CF, CB, BA, DCB, Ani, TFT, DE, XYL and Tolu, from 1 to 13. 1-3: Clear and transparent solution. 4-10: White precipitants at the bottom of the vials. 11-13: Yellow solution with two different phases.

is performed by adding different antisolvents to a 2 M MAI solution (dissolved in DMF/DMSO (v:v, 4:1)) at a volume ratio of 6:1. This ratio is very close to the volume ratio of the antisolvent to the perovskite precursor solution applied on each sample during spin coating process.

Furthermore, using the SEM top view images we determined the percentage of PbI_2 phases to the whole sampled area, and compared the amount of PbI_2 content in samples prepared using all 13 antisolvents with different dripping speeds (Figure 6.7). Details and the SEM images used for this calculation are further elaborated in the Appendix C. It is important to point out that the SEM images employed for calculating the PbI_2 amount are only representative areas for each sample, not the whole film, since the size of the shown SEM images in Figure C1, C2 and C3 is $12\,\mu\text{m} \times 9.6\,\mu\text{m}$.

Type I

MAI dissolves easily in the type I antisolvents. The solubility in EtOH, IPA and BuOH decreases exponentially from EtOH to BuOH, as presented in Figure A25 in the Appendix. The lowest volumes of solution required to fully dissolve 100 mg MAI powder in methanol (MeOH), EtOH, IPA and BuOH are listed in Table B6 (Appendix). FAI is even more soluble in the type I antisolvents than MAI. The solubility test of FAI is shown in Figure A26 and Table B7 in the Appendix. These results allow us to understand the performance trend for the type I antisolvents.

The organic precursors (i.e., MAI and FAI) are extremely soluble in MeOH. When it is used as the antisolvent (regardless of dripping speed), the MAI and FAI are washed away and the stoichiometry of the perovskite is significantly altered, and consequently a yellow (PbI_2) film is formed (Figure A27, Appendix). This is consistent with previous reports, as Xiao et al. also observed a yellow film using MeOH as the antisolvent [85].

When EtOH, the second most soluble solution for MAI and FAI, is applied slowly to the wet film in the spin coater, it stays in contact longer with the wet film. As a

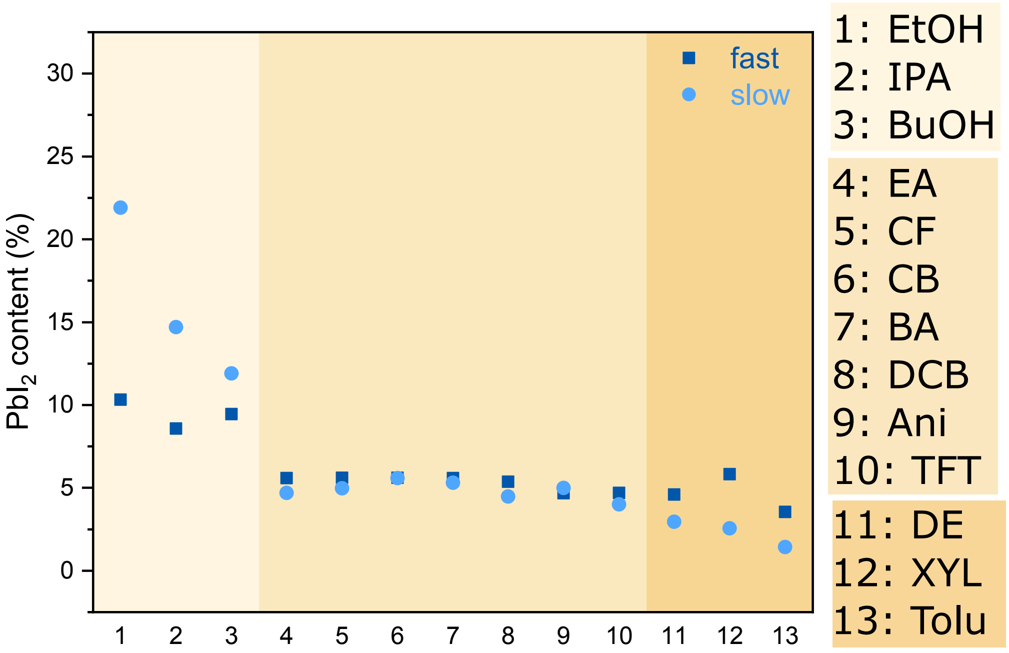

Figure 6.7: The PbI_2 content of the CsMAFA perovskite films fabricated using 13 antisolvents with fast (dark blue) and slow (light blue) dripping speeds on ITO/PTAA/PFN-P_2 substrates. The used antisolvents are EtOH, IPA, BuOH, EA, CF, CB, BA, DCB, Ani, TFT, DE, XYL and Tolu, from 1 to 13. The PbI_2 content is obtained by calculating the ratio of the white PbI_2 phases to the sampled area from the corresponding SEM images. Details are explained in the Appendix C.

consequence, it washes away more organic precursors, similar to the situation with MeOH. This explains the large PbI_2 content in the SEM images, the extremely low I/Pb ratio in the XPS results, and the poor PV performance (PCE below 5 %). Fast dripping of EtOH alleviates this problem by reducing the time in contact with the wet film, as indicated by the reduction of the PbI_2 amount from 22 % to 10 %, but a best PCE above 18 % is still never achieved.

IPA and BuOH exhibit a relatively lower solubility of MAI and FAI. Therefore, the differences in the PbI_2 content and device performance are still present between the fast and slow dripping speeds, but are much reduced in comparison to the EtOH case.

Perovskite films fabricated using type I antisolvents exhibit the largest PbI_2 content on the surface in comparison to the other two types, regardless of dripping speed, as a result of the soluble nature of MAI and FAI in the type I antisolvents. It is also important to note that when the type I antisolvents are dripped fast, the samples contain less PbI_2 content and have much improved device performance with narrower distributions.

Type II

The organic precursors are moderately soluble in the type II antisolvents when compared to type I. Unfortunately, the test with FAI with the same molar concentration and antisolvent volume as the MAI test is inconclusive, as shown in Figure A28 in the Appendix. For the MAI test, the white precipitants at the bottom of vials in Figure 6.6 suggest that the type II antisolvents extract the DMF/DMSO from the precursor solution, rather than dissolving the organic precursors, which helps to maintain the correct stoichiometry and facilitate the rapid formation of a high-quality perovskite film. As a result, the period that the antisolvent is in contact with the wet film on the spin coater is not critical. This explains the excellent device performances, regardless of dripping speed. It is also consistent with the much reduced PbI_2 content in comparison to the type I.

However, there is a slight variation among device performances using different antisolvents. For example, the devices using EA as the antisolvent obtain noticeably different PV parameters between fast and slow dripping speeds. This can be attributed to the fact that EA has the highest solubility for the organic precursors among all the type II antisolvents, as indicated by the smallest amount of the white precipitants in the EA mixture in Figure 6.6. In order to further investigate this issue, we fabricated perovskite devices using EA at six gradually changing dripping speeds. As presented in Figure A29 in the Appendix, the evolution in the V_{OC}, J_{SC}, FF and PCE from fast to slow is quite abrupt, rather than gradual. It seems that there is a critical point in the dripping speed; dripping slower than this will result in devices with reduced PV performances. Therefore, the difference in the device performance between the fast and slow dripping speeds for EA is probably due to the fact that our ‘slow’ speed is below this critical value. In contrast, the addition of TFT to the MAI solution leads to the formation of the largest amount of the white precipitants, which is consistent with the narrowest distribution in the device performance, regardless of dripping speed. Therefore, using an antisolvent that possesses a low solubility of MAI (such as TFT) will further expand the processing window of the dripping speed and increase the device reproducibility.

Type III

For the type III antisolvents, we observe a colour change and phase separation as shown in Figure 6.6 and A28 (Appendix). To further explore, we performed UV-vis measurements on these two phases (Figure A30 in the Appendix). An absorption onset in the bottom phase starting at around 500 nm is observed for all three solvents. This onset resembles the iodine (I_2) absorption spectrum [207], which suggests that a considerable amount of iodine is extracted by the antisolvent. The top phase of the Tolu mixture shows a similar onset as in the iodine, while the top phases of DE and XYL mixtures exhibit the two peaks, which are observed in the I_3^- absorption spectrum [207] as well, with I_3^- formed by combining iodine and iodide (I^-).

Here we propose that the relatively low PbI_2 amount in the slow samples is the result of longer contact duration with the antisolvent during spin coating, as the antisolvent extracts a significant amount of iodine, resulting in perovskite films with less PbI_2 content. This is consistent with the slightly enrichment in the I/Pb ratio in Figure 6.2 for the samples prepared using a fast dripping.

The poor coverage of perovskite films using a fast dripping of type III antisolvents is probably due to the phase separation of the organic precursor solution and the antisolvent, as shown in Figure 6.6 and A28 (Appendix). This phase separation suggests that the type III antisolvents are poor at extracting the DMF/DMSO from the organic precursor solution, which further impedes the formation of a high-quality perovskite film. When the antisolvent is applied fast to the spinning sample, it hits the centre area with a considerable amount of vertical force and is able to penetrate into the wet film and initiate crystallization of the perovskite. However, it then leaves the sample rapidly, without enough contact time with the outside regions to effectively extract the DMF/DMSO, yielding a film with poor uniformity. Consequently, a photoactive black perovskite is only formed in the middle of the substrate. In contrast to the type I antisolvents, where slow application prolongs contact and leads to the extraction of the organic compounds, for the type III antisolvents this leads to longer contact between the immiscible DMF:DMSO:perovskite and antisolvent phases, allowing for more complete extraction of the DMF/DMSO. This is supported by the formation of a uniform, compact perovskite film for the slow antisolvent application, and an inhomogeneous, pinhole-possessing film for fast application.

6.5 Conclusions

In this chapter, we systematically investigate the relationship between antisolvent type and dripping speed, and their effects on PV performance. Using PV, XPS, SEM and solubility measurements, we demonstrate that the organic precursors' solubility in the antisolvent has a tremendous effect on the perovskite formation, microstructure, and consequently, the final device performance. Our study shows that the antisolvents which exhibit a low solubility of organic precursors have an extended processing window, which is not limited to certain dripping speed. Furthermore, antisolvents which phase separate (type III) can lead to poor film formation with inappropriate dripping speed. Therefore, the solubility test serves as a good indicator of which application speed is required to obtain a good device for a new antisolvent. Although it is possible to obtain high-functioning devices with appropriate dripping speed for every antisolvent, the use of certain types of antisolvents eases the fabrication process and improves device reproducibility. We demonstrate that the devices fabricated using TFT as the antisolvent exhibit the best PV performance with the highest reproducibility.

7 Conclusions and Future Work

This thesis focuses on investigating two of the biggest challenges of perovskite solar cells: stability and reproducibility. Chapter 4 studies the role of microstructure on the oxygen and light induced degradation of perovskite films. Chapter 5 and 6 investigate the reproducibility issue from two different aspects: large-scale inhomogeneities of perovskite films, and how device performance is influenced by antisolvent type and dripping speed during film fabrication.

In Chapter 4, we investigate the degradation of $CH_3NH_3PbI_3$ films in controlled oxygen atmospheres under continuous illumination, using UV-vis, PDS, XPS, PV and SEM measurements. We reveal the dominant role of the microstructure on the oxygen and light induced degradation: perovskite films with small, irregular grains and high defect density degrade much faster and more severely than films with large uniform grains and better electronic properties. Therefore, by improving the perovskite film quality one could enhance the stability of perovskite films and devices under exposure to oxygen and light. In addition, we demonstrate that this degradation occurs even at low oxygen levels under illumination. This points out the importance of avoiding unnecessary light exposure during device fabrication in non-inert atmospheres, in order to reduce the degradation occurring during the production phase and further degradation caused by incorporated oxygen.

Chapter 5 presents the large-scale chemical compositional and electronic inhomogeneities of the $CH_3NH_3PbI_3$ perovskite films observed by XPS and UPS mapping experiments. We demonstrate that these inhomogeneities are not limited to certain fabrication methods, and are therefore likely present in films produced by other research groups. Furthermore, we find that the extent of the variation in photovoltaic performance across the entire sample is related to the extent of the observed inhomogeneities, which explains the wide spread of device performance reported in the literature. It suggests that a plausible way to produce devices with reliable and constant performance is to focus on improving the perovskite fabrication process in order to obtain an active layer with a uniform surface composition and electronic properties. Additionally, our results highlight the importance of studying the surface properties of perovskite layers, instead of simply focusing on bulk properties such as microstructure and absorption, which do not provide any information about surface inhomogeneities.

In Chapter 6, we turn our attention to improving device reproducibility by optimizing the antisolvent treatment procedure using PV, XPS and SEM measurements. We focus on the relationship between antisolvent type and dripping speed, and their effects on PV performance of triple cation perovskite $(Cs_{0.05}(MA_{0.17}FA_{0.83})_{0.95}Pb(I_{0.9}Br_{0.1})_3)$ devices. We find that the solubility of organic precursors in the antisolvent has a tremendous influence on the perovskite formation, microstructure, and consequently, the final device performance. We demonstrate that using certain antisolvents (such as anisole or trifluorotoluene) which possess a low solubility of organic precursors improves device reproducibility by widening the dripping speed ‘window’, the dripping speeds at which a high-quality perovskite film is formed. In contrast, antisolvents which easily dissolve the organic precursors (such as alcohols) will extract these organics during film formation, significantly damaging the perovskite composition and microstructure. Lastly, we find that antisolvents (such as diethyl ether) which phase separate with the host solvents can lead to incomplete coverage. This suggests that the solubility test is an indicator of which application speed is required to obtain a good device for a new antisolvent. Moreover, our finding shows that these drawbacks can be mitigated by using the appropriate dripping speed, and that for every antisolvent it is possible to produce high-functioning devices by considering this factor.

With more attention attracted to the mixed cation perovskites, and initial performance approaching the records of conventional silicon photovoltaics, future studies should focus more on investigating the stability and reproducibility of these perovskites. For instance, the degradation processes of the triple or quadruple cation perovskite films and devices should be thoroughly investigated under various operating conditions. Furthermore, one can explore the role of different cations on the degradation process, since various cations such as Rb^+, K^+ and GA^+ have been incorporated in the perovskite material system and have been shown to dramatically alter the device stability. Moreover, it would be interesting to study the chemical compositional and electronic inhomogeneities of various mixed cation perovskites, and investigate which perovskite material system yields the most homogenous film and device.

Appendices

A Figures

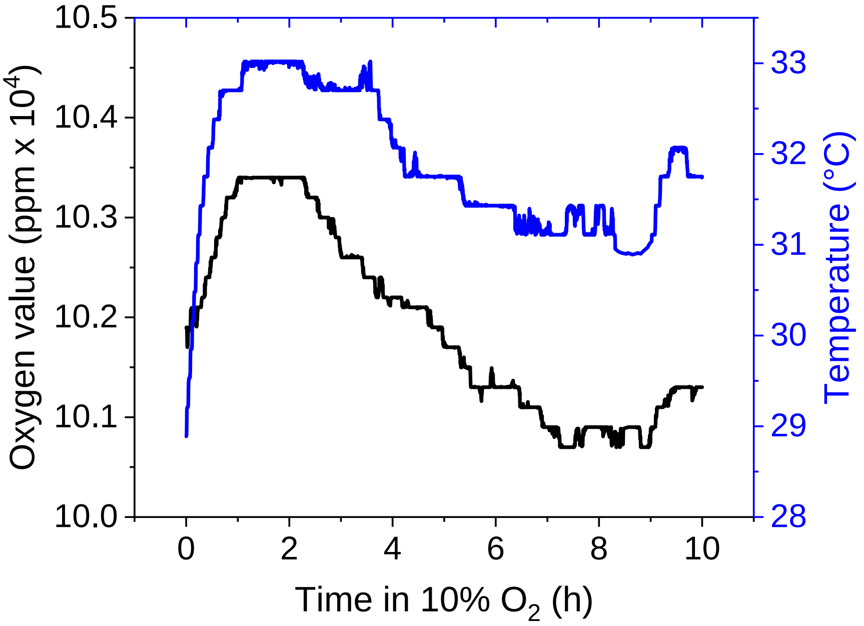

Figure A1: Oxygen level (left axis) and temperature (right axis) of the environmental box monitored throughout the 10 % oxygen degradation experiment. Adapted with permission from [58]. Copyright 2017, Wiley-VCH.

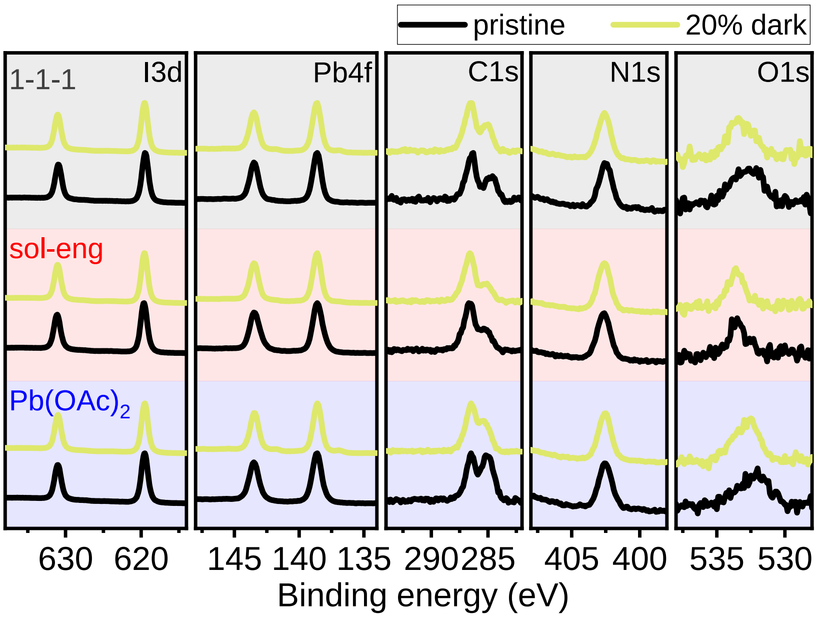

Figure A2: X-ray photoemission spectroscopy measurements on pristine perovskite layers (dark lines) and degraded films for 48 h under 20 % oxygen in dark. Perovskite films were fabricated using the $Pb(OAc)_2$, sol-eng and 1-1-1 recipes on PEDOT:PSS coated ITO substrates.

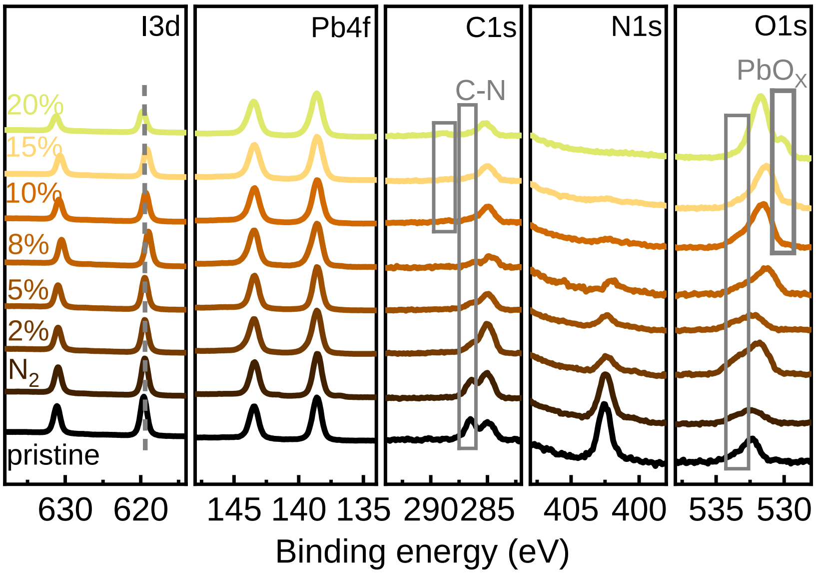

Figure A3: X-ray photoemission spectroscopy measurements on pristine and degraded (10 h under various oxygen levels at 1 sun illumination) perovskite layers fabricated using the $Pb(OAc)_2$ recipe on ITO substrates.

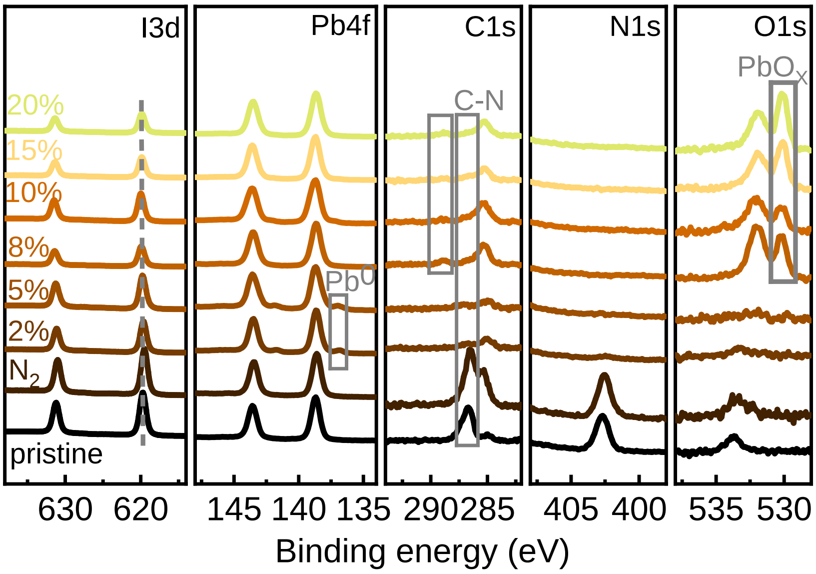

Figure A4: X-ray photoemission spectroscopy measurements on pristine and degraded (10 h under various oxygen levels at 1 sun illumination) perovskite layers fabricated using the sol-eng recipe on ITO substrates.

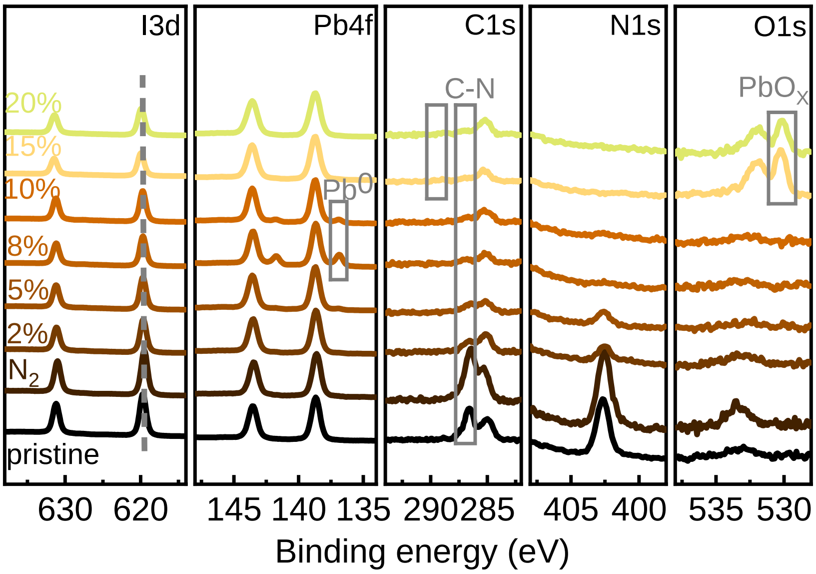

Figure A5: X-ray photoemission spectroscopy measurements on pristine and degraded (10 h under various oxygen levels at 1 sun illumination) perovskite layers fabricated using the 1-1-1 recipe on ITO substrates.

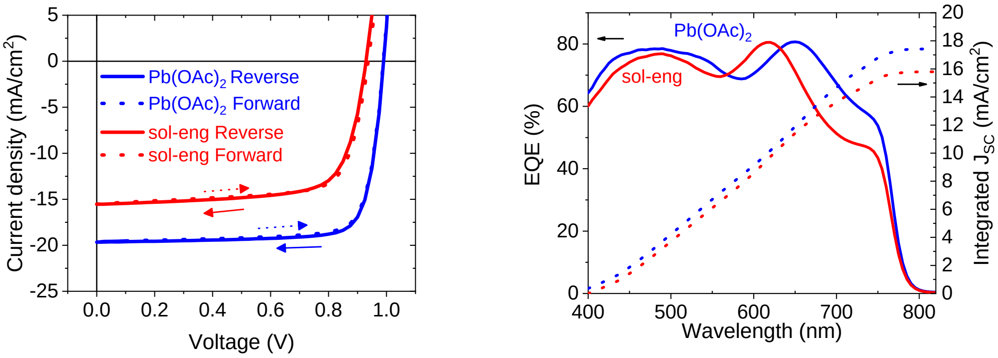

Figure A6: Current-voltage curves of champion devices with the structure ITO/PEDOT:PSS/$CH_3NH_3PbI_3$/$PC_{61}BM$/BCP/Ag with perovskite active layers prepared by the $Pb(OAc)_2$ and sol-eng recipes (left) as well as corresponding EQE spectra and integrated J_{SC} (right). Adapted with permission from [58]. Copyright 2017, Wiley-VCH.

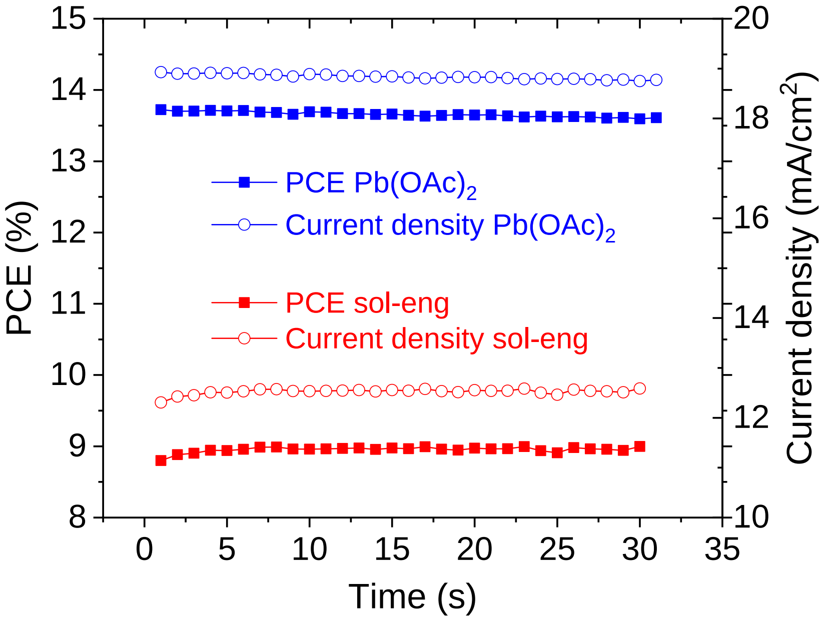

Figure A7: Power conversion efficiency and current density of solar cells fabricated by the $Pb(OAc)_2$ and sol-eng recipes over 30 s continuous illumination at maximum power point (0.78 V and 0.7 V for $Pb(OAc)_2$ and sol-eng, respectively.) Adapted with permission from [58]. Copyright 2017, Wiley-VCH.

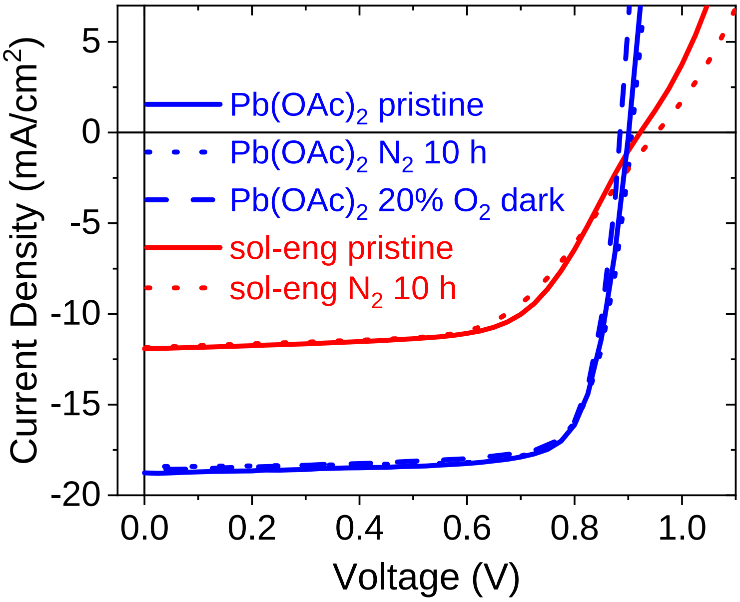

Figure A8: Current-voltage curves of ITO/PEDOT:PSS/$CH_3NH_3PbI_3$/$PC_{61}BM$/BCP/Ag solar cells, with perovskite active layers stored in glovebox (pristine), degraded in nitrogen for 10 h and in 20 % oxygen for 72 h, for both the $Pb(OAc)_2$ and sol-eng recipes. Adapted with permission from [58]. Copyright 2017, Wiley-VCH.

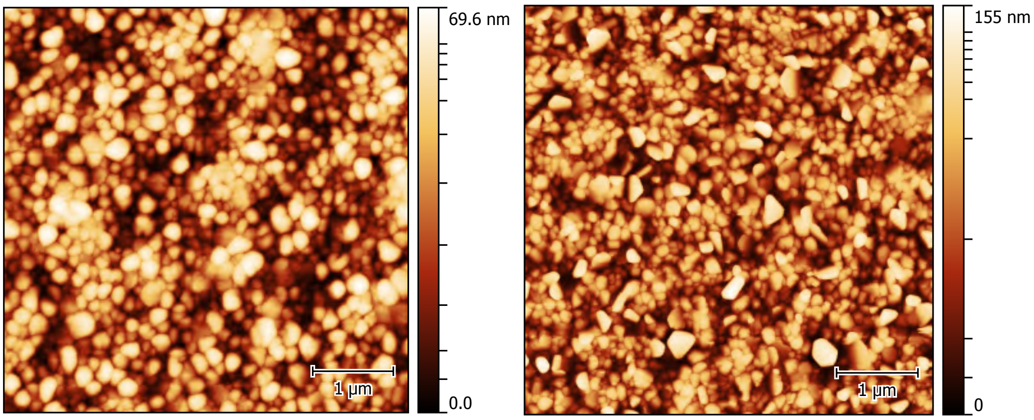

Figure A9: Atomic force microscopy picture of pristine perovskite films prepared by the $Pb(OAc)_2$ (left) and sol-eng recipes (right). Adapted with permission from [58]. Copyright 2017, Wiley-VCH.

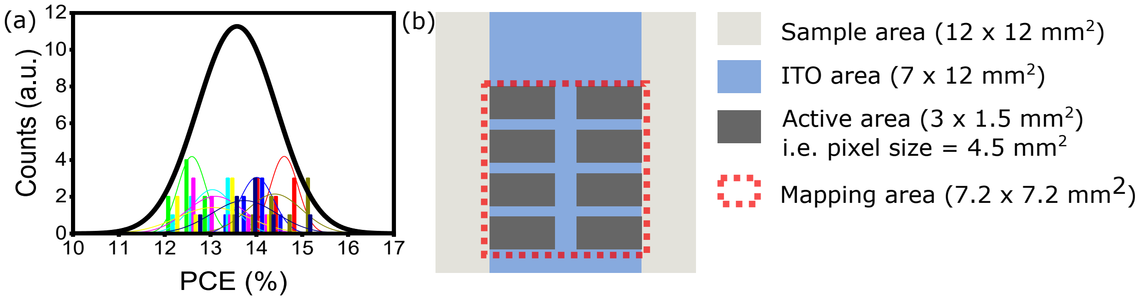

Figure A10: (a) The real histogram of Figure 5.1, which only shows the fitted Gaussian curves to each device (8 pixels, in total 8 devices, i.e., 64 pixels) histogram. (b) Illustration of the substrate area, pixel area and also the mapping area. Detailed numbers are given on the right. Adapted with permission from [140]. Copyright 2018, American Chemical Society.

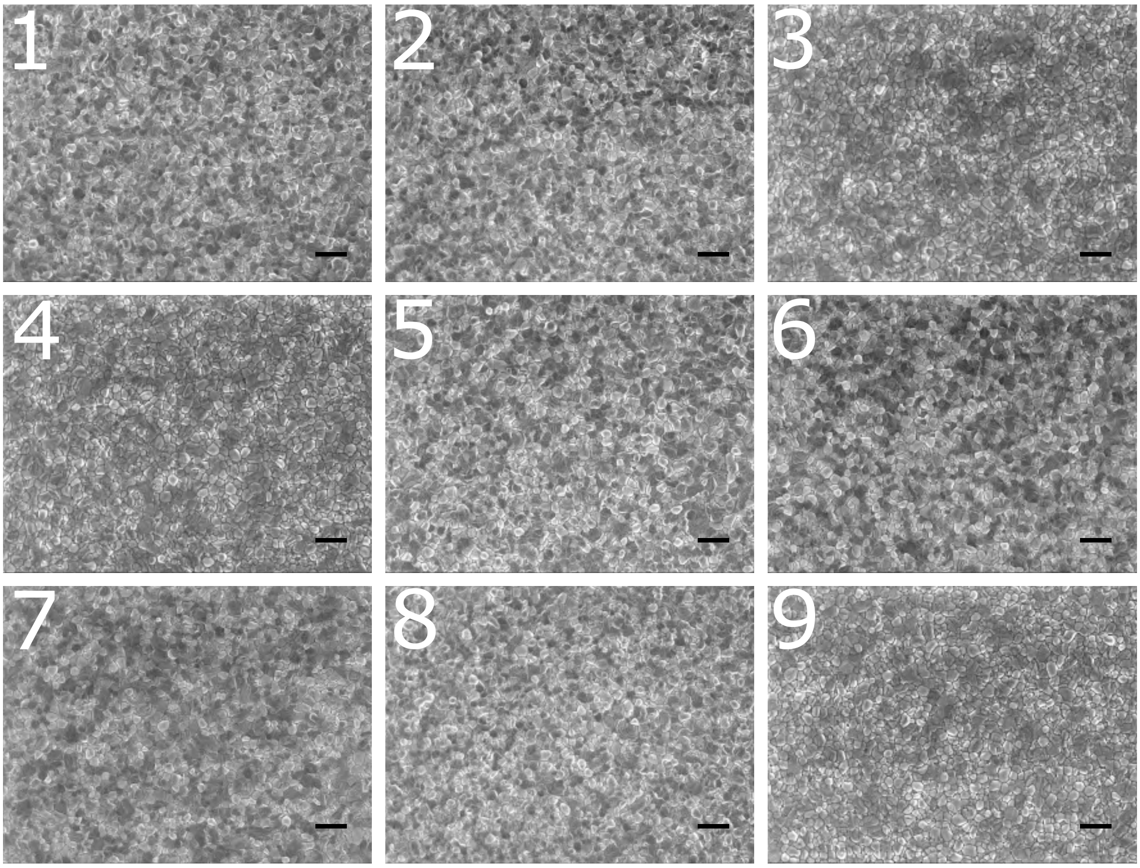

Figure A11: SEM images taken across different sample areas (1-9) on the film prepared by the $Pb(OAc)_2$ recipe. Scale bar is 1 µm. No strong variations in microstructure were observed. The measurements were carried out by Dr. Paul Fassl. Adapted with permission from [140]. Copyright 2018, American Chemical Society.

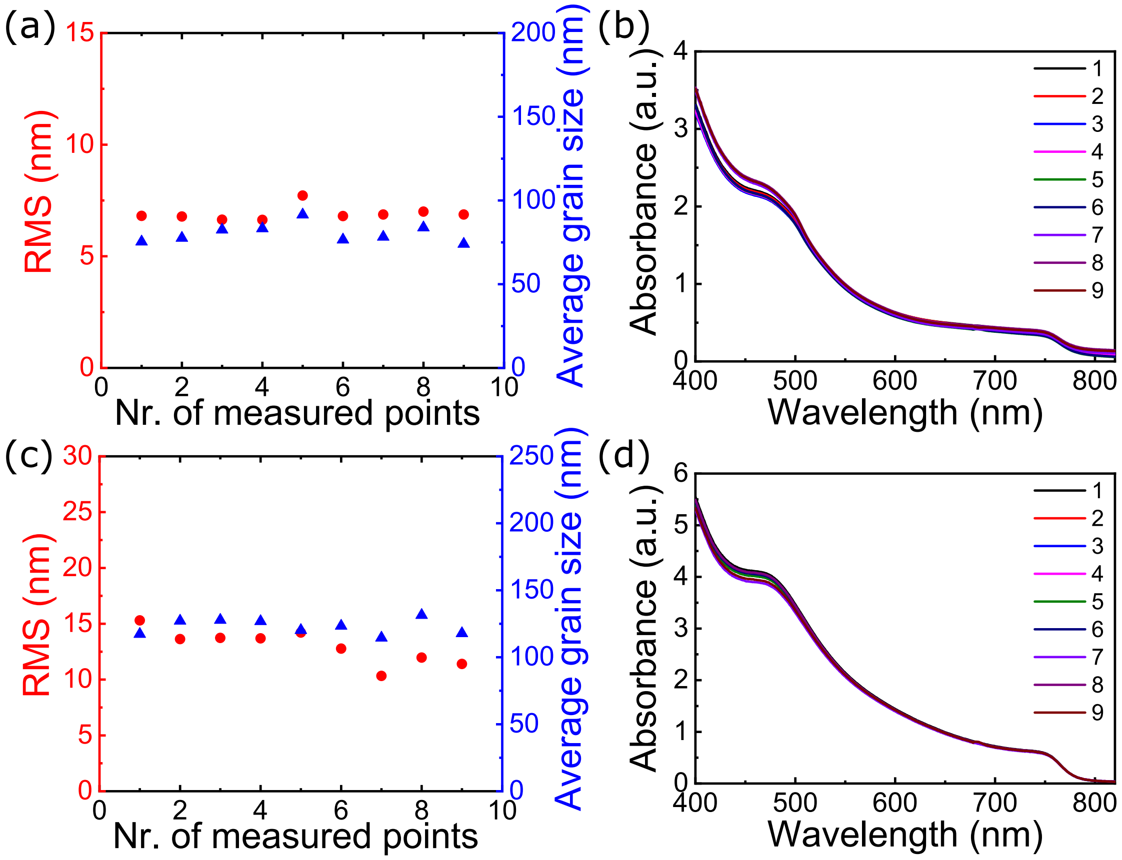

Figure A12: Roughness and average grain size of an inhomogeneous perovskite film produced by (a) sol-eng and (c) 1-1-1 recipes measured at various spots, calculated from AFM measurements. Absorbance spectra of an inhomogeneous perovskite film produced by (b) sol-eng and (d) 1-1-1 recipes measured at various spots. Adapted with permission from [140]. Copyright 2018, American Chemical Society.

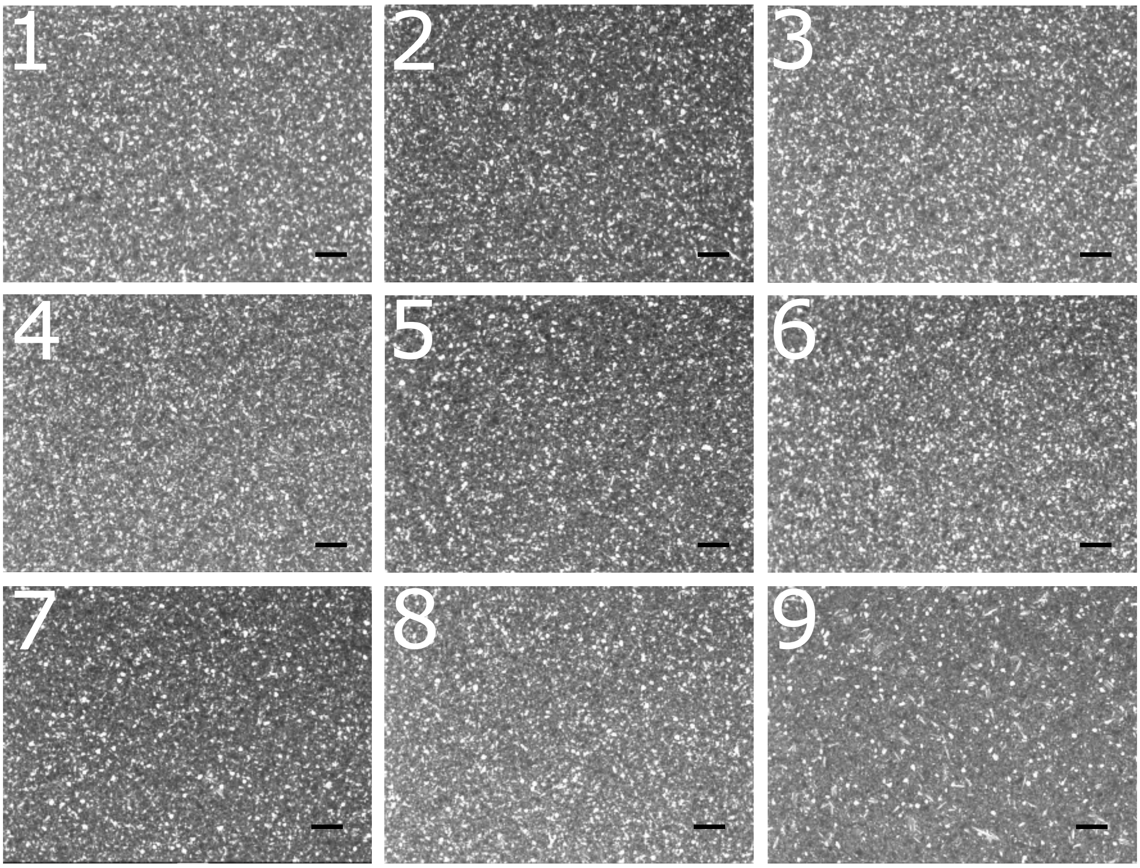

Figure A13: SEM images taken across different sample areas (1-9) on the film prepared by the sol-eng recipe. Scale bar is 1 µm. No strong variations in microstructure were observed. The measurements were carried out by Dr. Paul Fassl. Adapted with permission from [140]. Copyright 2018, American Chemical Society.

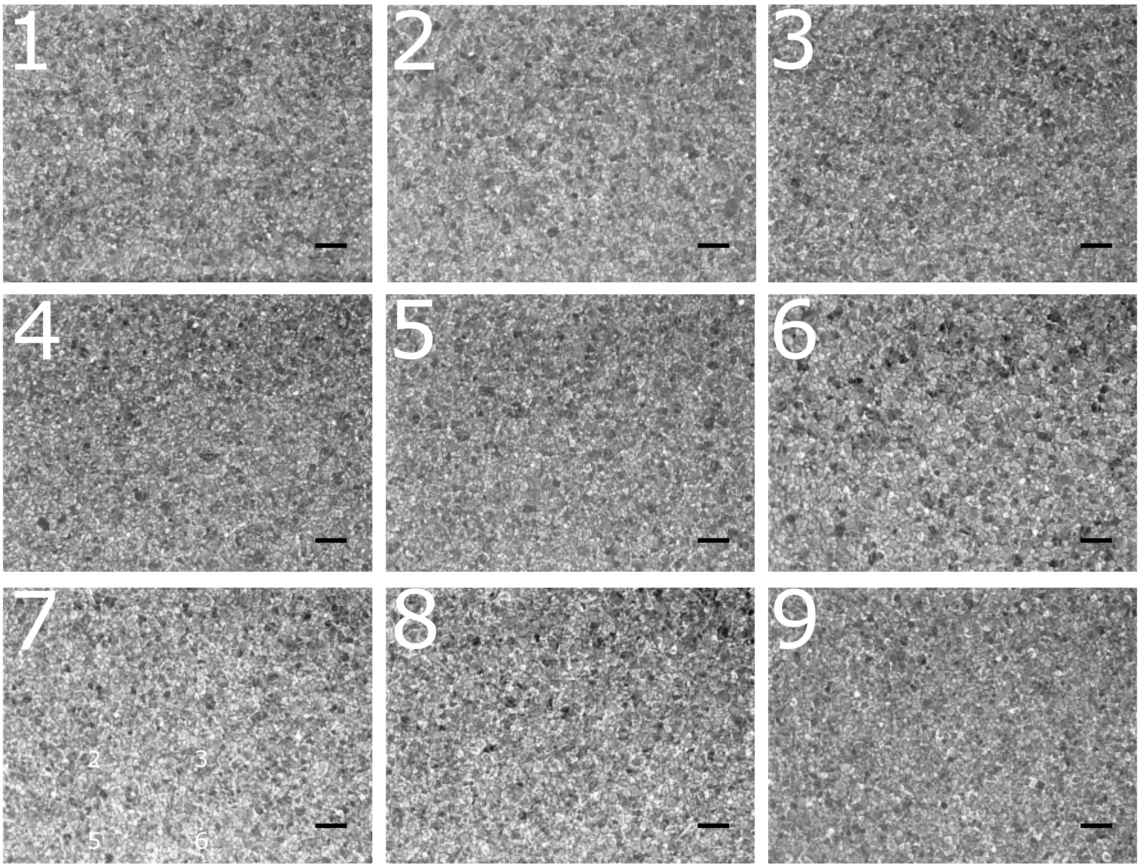

Figure A14: SEM images taken across different sample areas (1-9) on the film prepared by the 1-1-1 recipe. Scale bar is 1 µm. No strong variations in microstructure were observed. The measurements were carried out by Dr. Paul Fassl. Adapted with permission from [140]. Copyright 2018, American Chemical Society.

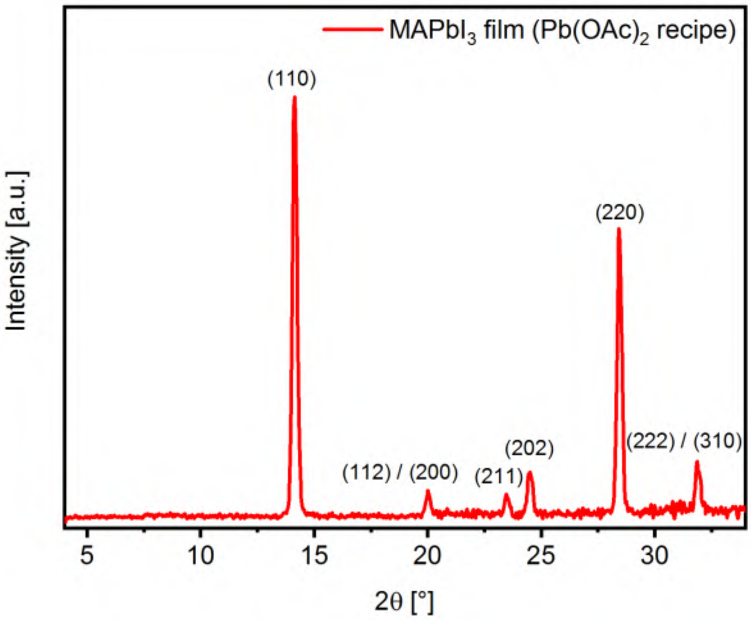

Figure A15: X-ray diffraction spectrum of the perovskite film prepared by the Pb(OAc)$_2$ recipe. The measurements were conducted by Bruker, Karlsruhe as part of demonstration measurements on a D8 ADVANCE DaVinci diffractometer equipped with a PILATUS3-100K detector. Reproduced with permission from [140]. Copyright 2018, American Chemical Society.

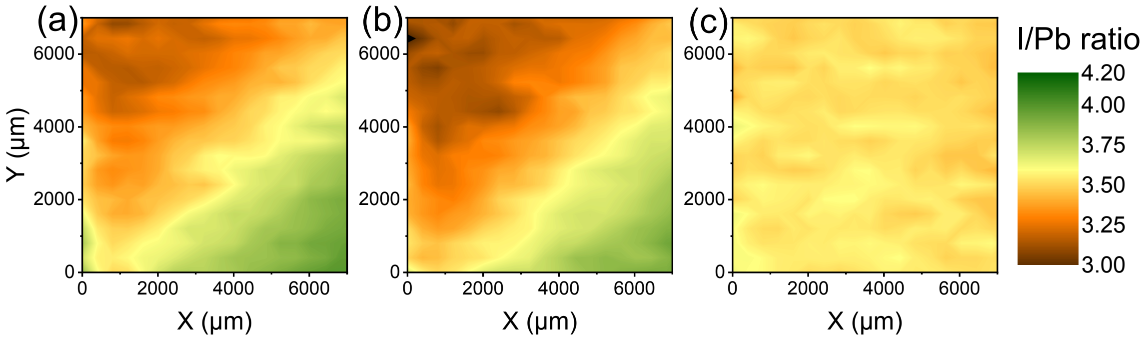

Figure A16: I/Pb maps of perovskite films produced by the Pb(OAc)$_2$ recipe after storing in (a) a N$_2$-glovebox, (b) a dry air filled glovebox and (c) vacuum for 50 hours. Reproduced with permission from [140]. Copyright 2018, American Chemical Society.

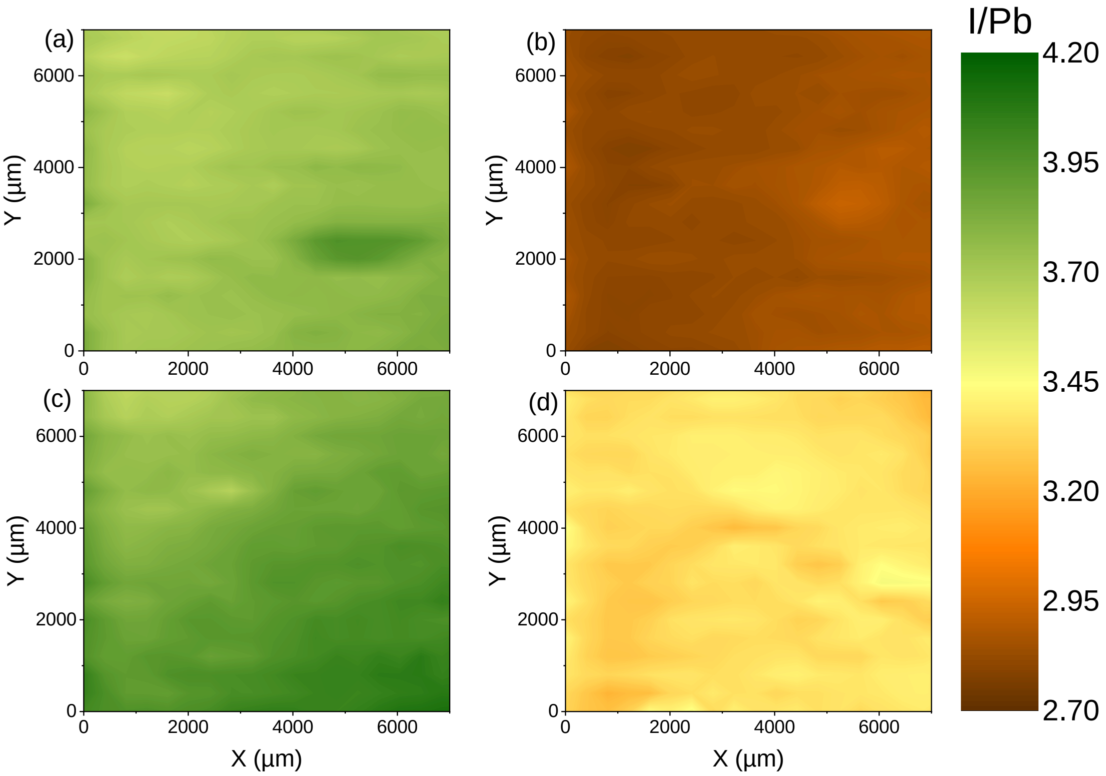

Figure A17: I/Pb maps of perovskite films produced by the sol-eng recipe after storing in (a) a dry air filled glovebox and (b) vacuum for 50 hours. I/Pb maps of perovskite films produced by the 1-1-1 recipe after storing in (a) a dry air filled glovebox and (b) vacuum for 50 hours.

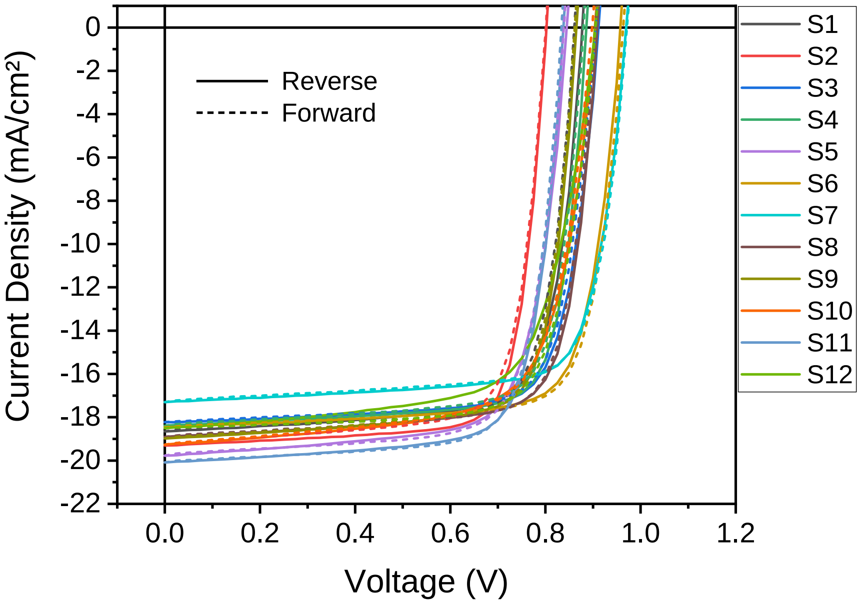

Figure A18: J-V curves of the champion pixels from the twelve solar cells in Figure 5.7. Solid line and dashed line indicates the reverse (open-circuit to short-circuit) and forward (short-circuit to open-circuit) scan directions, respectively. Reproduced with permission from [140]. Copyright 2018, American Chemical Society.

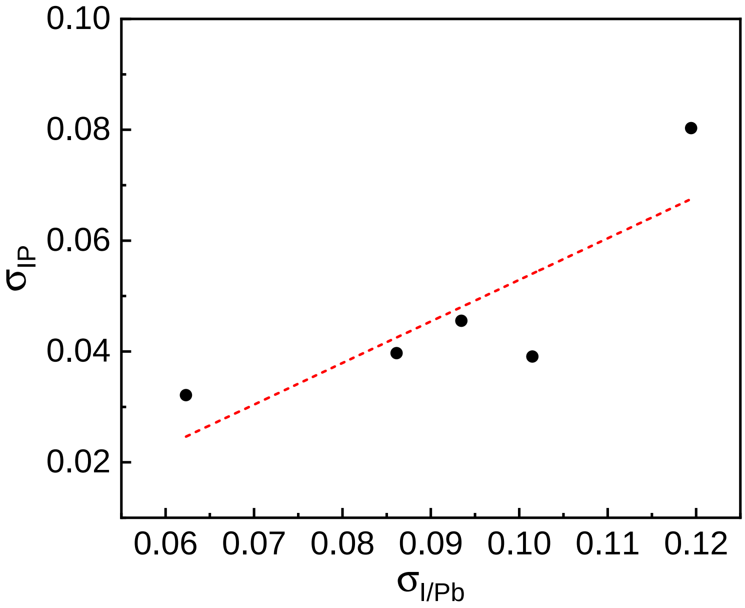

Figure A19: Standard deviation of IP (σ_{IP}) compared to the standard deviation of I/Pb ($\sigma_{\mathrm{I/Pb}}$) of five perovskite films prepared by the $Pb(OAc)_2$ method, where the XPS and UPS mapping were performed to the same region of the same sample. Only five samples were measured due to the doubling of exposure time to vacuum which changes the surface properties of perovskite films. Reproduced with permission from [140]. Copyright 2018, American Chemical Society.

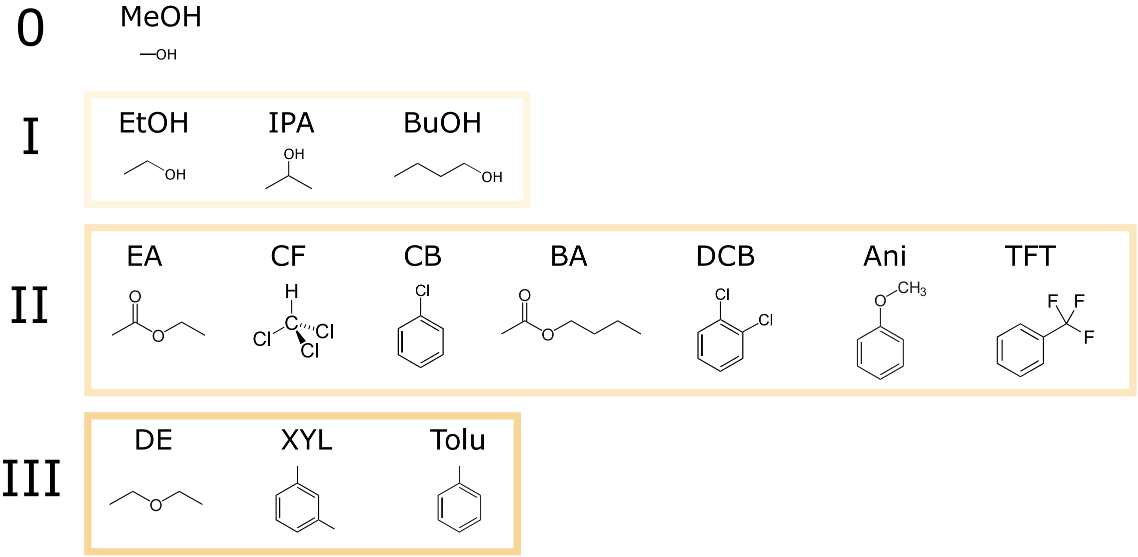

Figure A20: Chemical structures of all solvents used in Chapter 6 as the antisolvent. 0: methanol (MeOH). I: ethanol (EtOH), 2-propanol (IPA) and 1-butanol (BuOH). II: ethyl acetate (EA), chloroform (CF), chlorobenzene (CB), butyl acetate (BA), 1,2-dichlorobenzene (DCB), anisole (Ani) and trifluorotoluene (TFT). III: diethyl ether (DE), m-xylene (XYL) and toluene (Tolu).

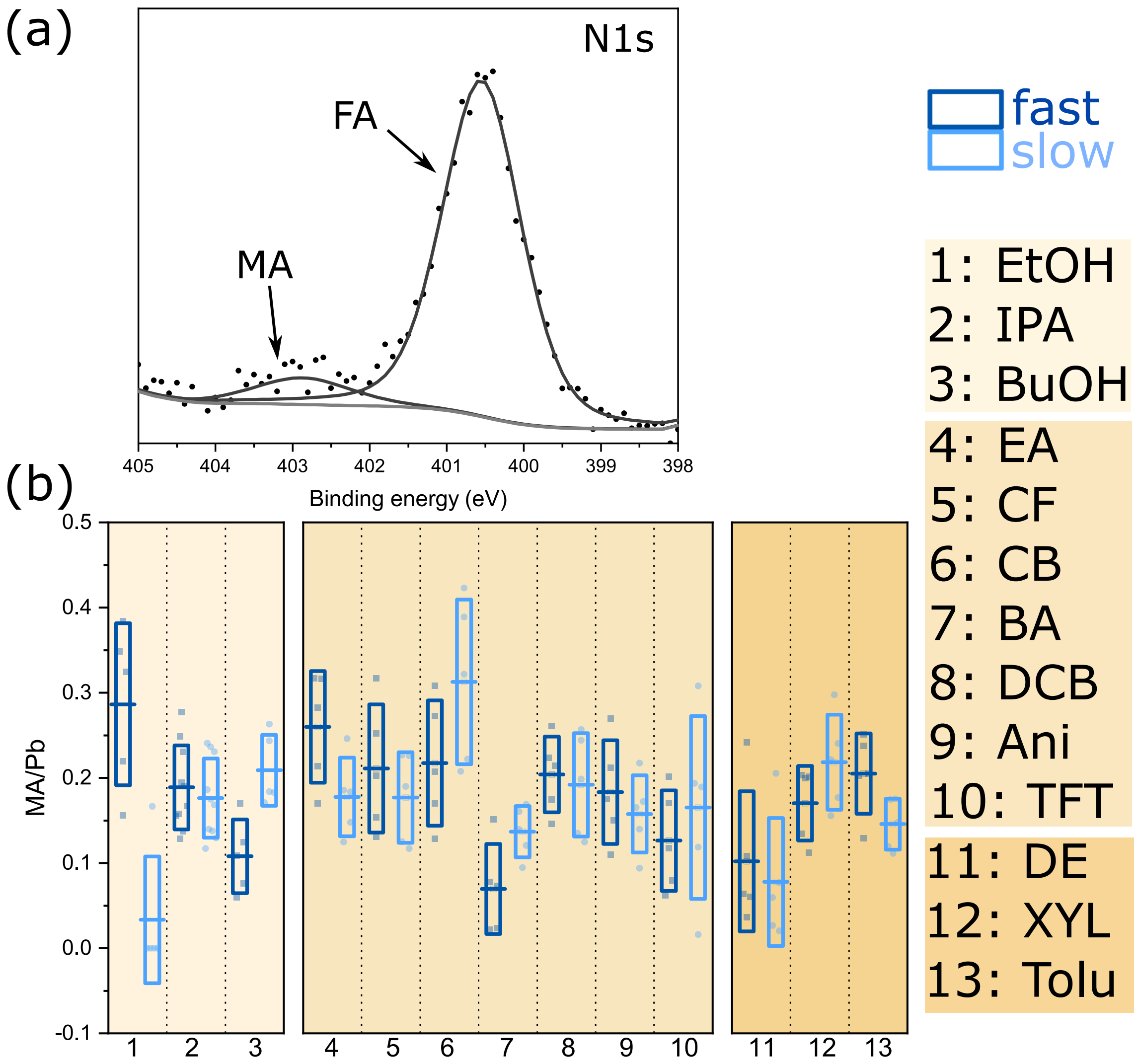

Figure A21: (a) N1s spectrum of the CsMAFA perovskite film coated on ITO/PTAA/PFN-P_2 substrate using TFT as the antisolvent. (b) The MA/Pb ratio of the CsMAFA perovskite films fabricated using 13 antisolvents with fast (dark blue) and slow (light blue) dripping speeds on ITO/PTAA/PFN-P_2 substrates. The used antisolvents are EtOH, IPA, BuOH, EA, CF, CB, BA, DCB, Ani, TFT, DE, XYL and Tolu, from 1 to 13.

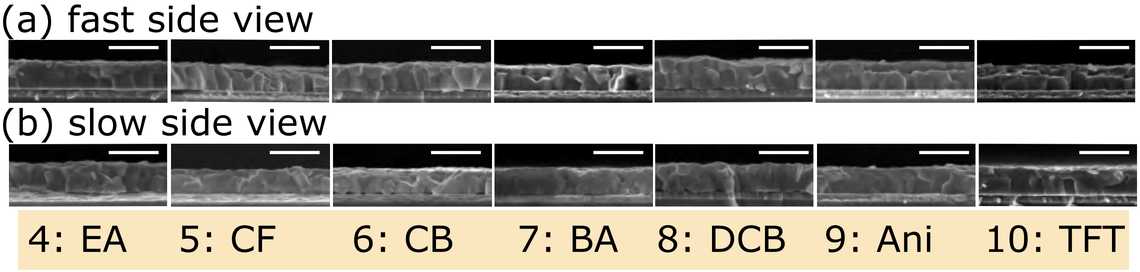

Figure A22: Scanning electron microscopy cross-section images of the CsMAFA perovskite films fabricated by dripping the antisolvent fast (a) and slow (b). The antisolvents used are EA, CF, CB, BA, DCB, Ani and TFT, from left to right. Scale bars represent 1 μm. The measurements were carried out by Dr. Fabian Paulus.

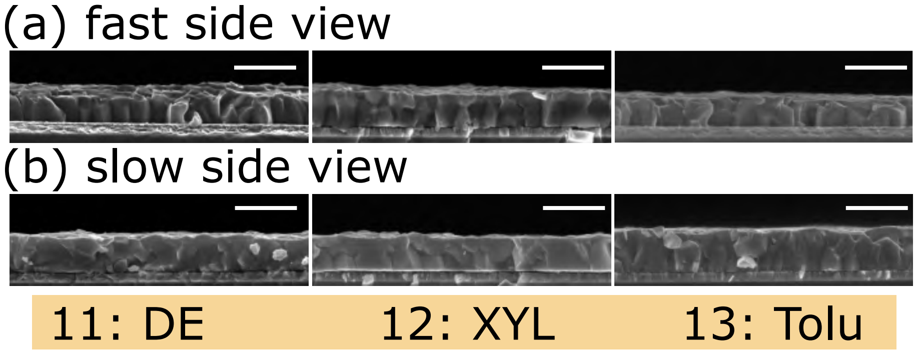

Figure A23: Scanning electron microscopy cross-section images of the CsMAFA perovskite films fabricated by dripping the antisolvent fast (a) and slow (b). The antisolvents used are DE, XYL and Tolu, from left to right. Scale bars represent 1 μm. The measurements were carried out by Dr. Fabian Paulus.

(a) fast top view

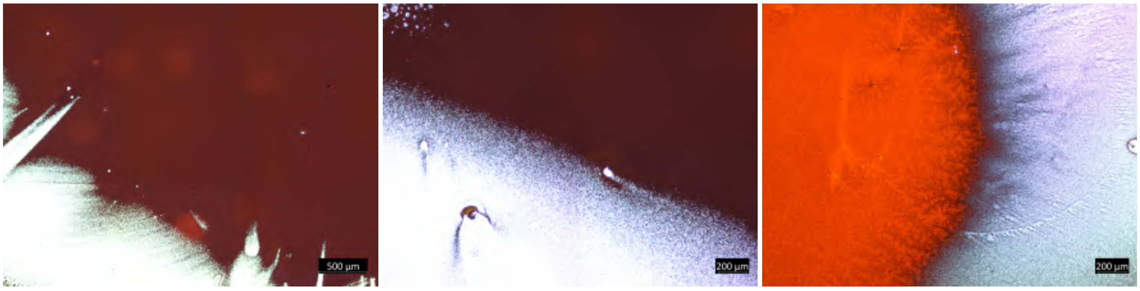

(b) slow top view

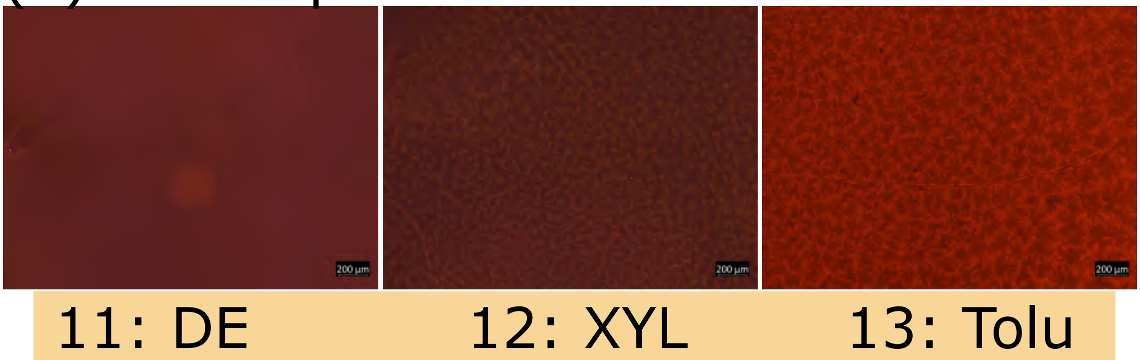

Figure A24: Optical microscopy images (transmission mode) of the CsMAFA perovskite films fabricated by dripping the antisolvent fast (a) and slow (b). The antisolvents used are DE, XYL and Tolu, from left to right. The measurements were carried out by Maximilian Litterst.

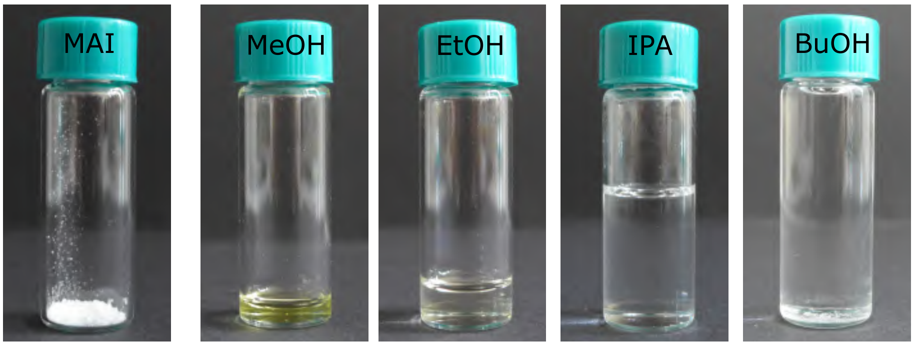

Figure A25: Pictures of 100 mg MAI powder, 100 mg MAI dissolved in 230 μl MeOH, 100 mg MAI dissolved in 510 μl EtOH, 100 mg MAI dissolved in 1540 μl IPA and 100 mg MAI in 4240 μl BuOH. Note that only the MAI in BuOH solution is not fully dissolved.

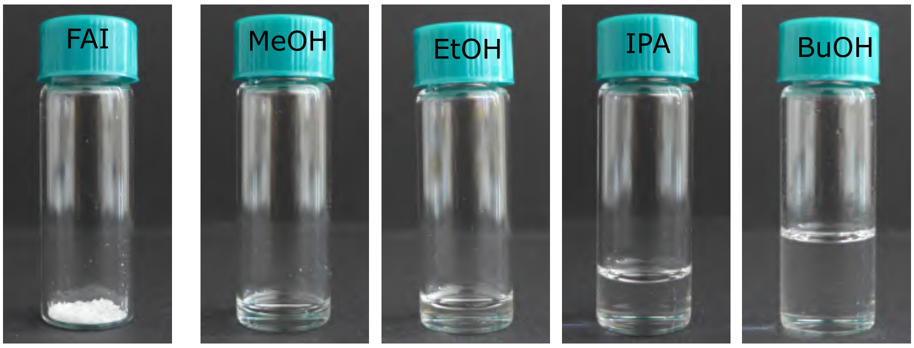

Figure A26: Pictures of 100 mg FAI powder, 100 mg FAI dissolved in 170 μl MeOH, 100 mg FAI dissolved in 350 μl EtOH, 100 mg FAI dissolved in 820 μl IPA and 100 mg FAI in 1640 μl BuOH.

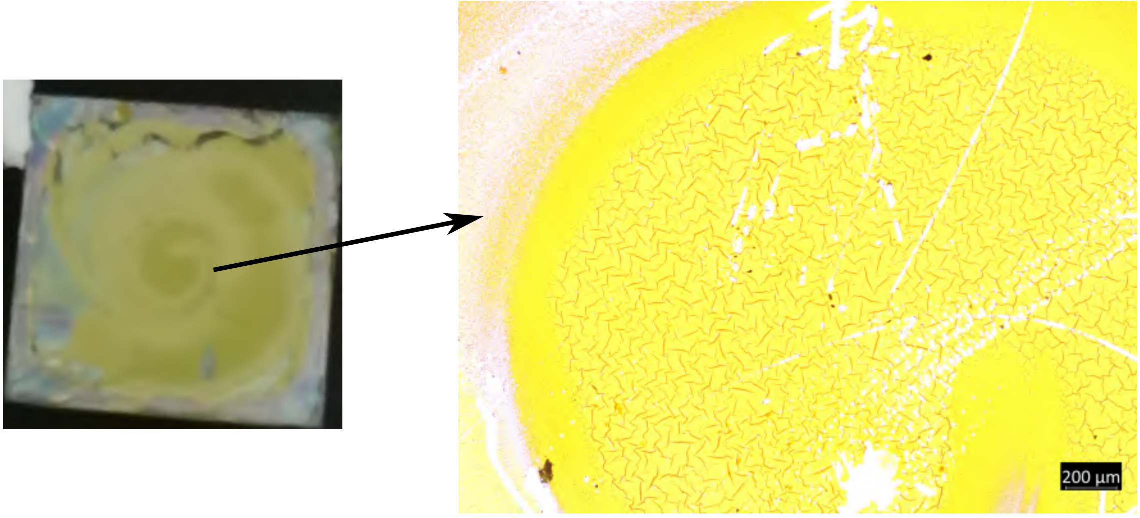

Figure A27: Picture (left) and optical microscopy image (transmission mode) (right) of the 'perovskite' fabricated using MeOH as the antisolvent. The measurements were carried out by Maximilian Litterst.

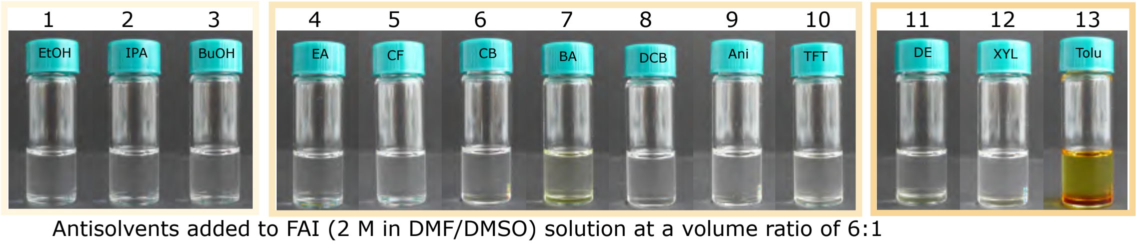

Figure A28: Pictures of different solution mixtures, where 13 antisolvents were added to the FAI solution (2M in DMF/DMSO) at a volume ratio of 6:1. The used antisolvents are EtOH, IPA, BuOH, EA, CF, CB, BA, DCB, Ani, TFT, DE, XYL and Tolu, from 1 to 13. 1-10: Clear and transparent solution. 11-13: Solution with two different phases.

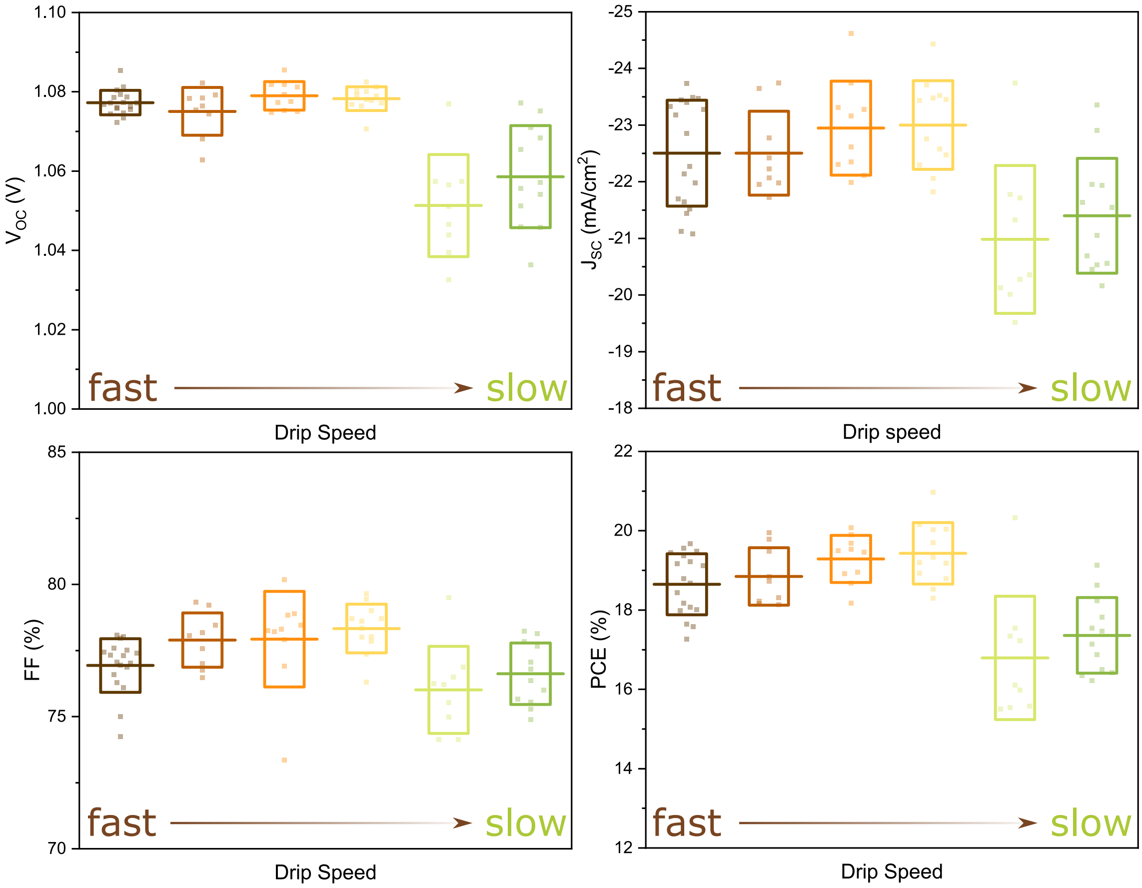

Figure A29: Solar cell characteristics of ITO/PTAA/PFN-P$_2$/CsMAFA/PC$_{61}$BM/BCP/Ag solar cells, with the perovskite films fabricated using EA with six different dripping speeds, which gradually change from left, fast, to right, slow. The measurements were carried out by Dr. Alex Taylor.

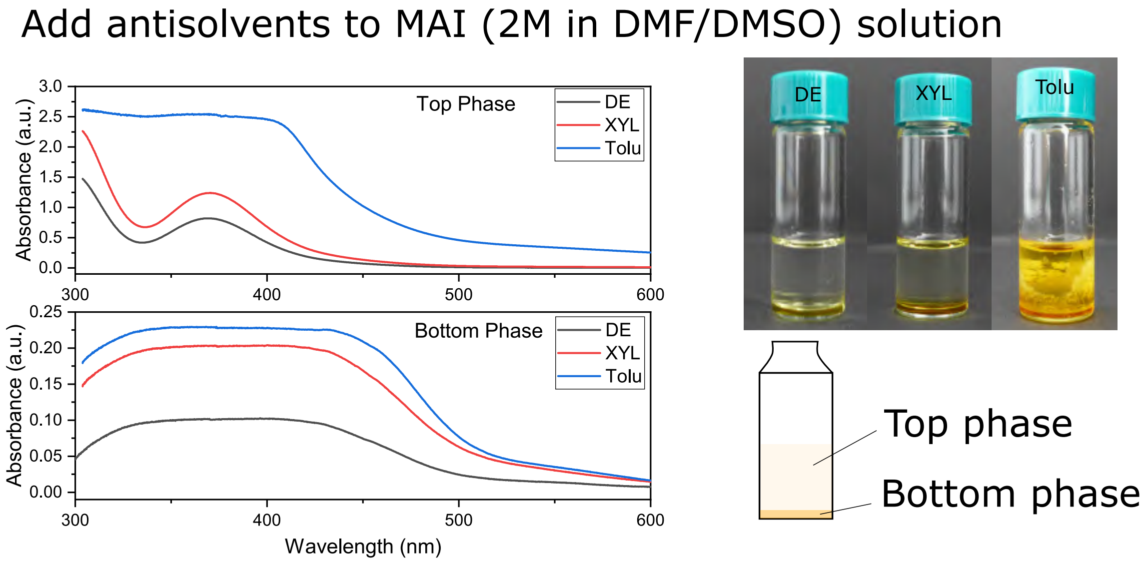

Figure A30: Absorbance spectra of the top and bottom phases of the solution mixtures of the antisolvents (i.e., DE, XYL and Tolu) and MAI solution (2M in DMF/DMSO) at a volume ratio of 6:1. The right panel shows the pictures of these solution mixtures and also an illustrate of the phase separation.

B Tables

Table B1: Densities, molarities and volume factors of the examples of stock solutions.

solution	moles per L	density (g/mL)	molarity (mol/L)	volume factor (γ_V)
FAI in DMF/DMSO	2.5	1.190 ± 0.001	2.117	1.181
MAI in DMF/DMSO	2.5	1.158 ± 0.001	2.109	1.185

Table B2: Statistics of PV parameters for $Pb(OAc)_2$ (158 devices) and sol-eng (130 devices) solar cells with the structure ITO/PEDOT:PSS/$CH_3NH_3PbI_3$/$PC_{61}BM$/BCP/Ag. Adapted with permission from [58]. Copyright 2017, Wiley-VCH.

	$Pb(OAc)_2$ (reverse)	$Pb(OAc)_2$ (forward)	sol-eng (reverse)	sol-eng (forward)
V_{OC} (V)	0.91 ± 0.04	0.90 ± 0.04	0.93 ± 0.06	0.92 ± 0.06
J_{SC} (mA/cm^2)	19.3 ± 0.9	19.3 ± 0.9	14.0 ± 1.1	14.0 ± 1.1
FF (%)	78.1 ± 2.5	77.0 ± 2.6	64.0 ± 10.9	63.3 ± 11.7
PCE (%)	13.68 ± 0.70	13.41 ± 0.77	8.24 ± 0.87	8.05 ± 0.96

Table B3: List of references from 2013 to 2017 from which the values for the spread in PCE was extracted to obtain Figure 5.1 (left). Adapted with permission from [140]. Copyright 2018, American Chemical Society.

Year	Reference	PCE range (max-min)(%)
2013	W. A. Laban, L. Etgar, Energy Environ. Sci. 2013, 6, 3249.	6 - 8.04
2014	J. Cui, F. Meng, H. Zhang, K. Cao, H. Yuan, Y. Cheng, F. Huang, M. Wang, ACS Appl. Mater. Interfaces 2014, 6, 22862.	7 - 9.84
2014	H. Zhou, Y. Shi, Q. Dong, H. Zhang, Y. Xing, K. Wang, Y. Du, T. Ma, J. Phys. Chem. Lett. 2014, 5, 3241.	4.5 - 9.08
2014	W. Yan, Y. Li, W. Sun, H. Peng, S. Ye, Z. Liu, Z. Bian, C. Huang, RSC Adv. 2014, 4, 33039.	8.75 - 11.8
2014	Y. S. Kwon, J. Lim, H.-J. Yun, Y.-H. Kim, T. Park, Energy Environ. Sci. 2014, 7, 1454.	6.8 - 9.2
2014	W. H. Nguyen, C. D. Bailie, E. L. Unger, M. D. McGehee, J. Am. Chem. Soc. 2014, 136, 10996.	3.9 - 4.7
2014	J. W. Lee, S. Park, M. J. Ko, H. J. Son, N. G. Park, ChemPhysChem 2014, 15, 2595.	6.75 - 8.7
2014	S. Aharon, S. Gamliel, B. El Cohen, L. Etgar, Phys. Chem. Chem. Phys. 2014, 16, 10512.	5 - 10.85
2014	J. Shi, J. Dong, S. Lv, Y. Xu, L. Zhu, J. Xiao, X. Xu, H. Wu, D. Li, Y. Luo, Q. Meng, Appl. Phys. Lett. 2014, 104, 63901.	7.5 - 10.49
2014	J. Shi, Y. Luo, H. Wei, J. Luo, J. Dong, S. Lv, J. Xiao, Y. Xu, L. Zhu, X. Xu, H. Wu, D. Li, Q. Meng, ACS Appl. Mater. Interfaces 2014, 6, 9711.	9 - 10.47
2015	G. Li, K. L. Ching, J. Y. L. Ho, M. Wong, H. S. Kwok, Adv. Energy Mater. 2015, 5, 1401775.	11.2 -15.2
2015	K. Wang, C. Liu, P. Du, H. L. Zhang, X. Gong, Small 2015, 11, 3369.	6.25 - 11.45
2015	X. Bao, Q. Zhu, M. Qiu, A. Yang, Y. Wang, D. Zhu, J. Wang, R. Yang, J. Mater. Chem. A 2015, 3, 19294.	8.25 - 12.78
2015	J. Yin, J. Cao, X. He, S. Yuan, S. Sun, J. Li, N. Zheng, L. Lin, J. Mater. Chem. A 2015, 3, 16860.	11.25 - 13.76
2015	C. Y. Chang, Y. C. Chang, W. K. Huang, K. T. Lee, A. C. Cho, C. C. Hsu, Chem. Mater. 2015, 27, 7119.	14.6 -16.5
2015	Y. C. Shih, L. Y. Wang, H. C. Hsieh, K. F. Lin, J. Mater. Chem. A 2015, 3, 9133.	8 - 12.02
2015	S. Li, K. Jiang, M. Su, X. Cui, J. Huang, Q. Zhang, X. Zhou, L. Yang, Y. Song, J. Mater. Chem. A 2015, 3, 9092.	9.8 - 12.3
2015	D. Forgács, M. Sessolo, H. J. Bolink, J. Mater. Chem. A 2015, 3, 14121.	10.5 - 12.5

2015	H. Wei, J. Xiao, Y. Yang, S. Lv, J. Shi, X. Xu, J. Dong, Y. Luo, D. Li, Q. Meng, Carbon N. Y. 2015, 93, 861.	10.5 - 13.53
2015	H. A. Abbas, R. Kottokkaran, B. Ganapathy, M. Samiee, L. Zhang, A. Kitahara, M. Noack, V. L. Dalal, APL Mater. 2015, 3, 016105.	10.5 - 13.7
2015	Y. Li, Y. Zhao, Q. Chen, Y. Yang, Y. Liu, Z. Hong, Z. Liu, Y. T. Hsieh, L. Meng, Y. Li, Y. Yang, J. Am. Chem. Soc. 2015, 137, 15540.	14.25 - 17.35
2015	S. Das, B. Yang, G. Gu, P. C. Joshi, I. N. Ivanov, C. M. Rouleau, T. Aytug, D. B. Geohegan, K. Xiao, ACS Photonics 2015, 2, 680.	8.75 - 13
2015	L. Zhu, J. Xiao, J. Shi, J. Wang, S. Lv, Y. Xu, Y. Luo, Y. Xiao, S. Wang, Q. Meng, X. Li, D. Li, Nano Res. 2015, 8, 1116.	9.25 - 12.96
2015	C. Bi, Q. Wang, Y. Shao, Y. Yuan, Z. Xiao, J. Huang, Nat. Commun. 2015, 6, 7747.	13.8 - 17.8
2015	L. Zuo, Z. Gu, T. Ye, W. Fu, G. Wu, H. Li, H. Chen, J. Am. Chem. Soc. 2015, 137, 2674.	13.05 - 15.67
2015	J. Zhang, F. Li, K. Yang, C. P. Veeramalai, T. Guo, Appl. Surf. Sci. 2016, 369, 308.	8 - 9.21
2016	J. Huang, X. Yu, J. Xie, D. Xu, Z. Tang, C. Cui, D. Yang, ACS Appl. Mater. Interfaces 2016, 8, 21505.	11.3 - 14.55
2016	A. Dubey, N. Kantack, N. Adhikari, K. M. Reza, S. Venkatesan, M. Kumar, D. Khatiwada, S. Darling, Q. Qiao, J. Mater. Chem. A 2016, 4, 10231.	12.4 - 16.83
2016	M. Qin, J. Ma, W. Ke, P. Qin, H. Lei, H. Tao, X. Zheng, L. Xiong, Q. Liu, Z. Chen, J. Lu, G. Yang, G. Fang, ACS Appl. Mater. Interfaces 2016, 8, 8460.	11.75 - 14.83
2016	Y. Guo, W. Sato, K. Shoyama, E. Nakamura, J. Am. Chem. Soc. 2016, 138, 5410.	15.4 - 16.02
2016	T. Singh, T. Miyasaka, Chem. Commun. 2016, 52, 4784.	15.5 - 18.5
2016	C. Y. Chang, W. K. Huang, J. L. Wu, Y. C. Chang, K. T. Lee, C. T. Chen, Chem. Mater. 2016, 28, 242.	13.85 - 15.85
2016	L. Zhao, D. Luo, J. Wu, Q. Hu, W. Zhang, K. Chen, T. Liu, Y. Liu, Y. Zhang, F. Liu, T. P. Russell, H. J. Snaith, R. Zhu, Q. Gong, Adv. Funct. Mater. 2016, 26, 3508.	15.3 - 18.3
2016	T. P. Gujar, M. Thelakkat, Energy Technol. 2016, 4, 449.	12 - 14.84
2016	X. Zhao, H. Shen, Y. Zhang, X. Li, X. Zhao, M. Tai, J. Li, J. Li, X. Li, H. Lin, ACS Appl. Mater. Interfaces 2016, 8, 7826.	10.25 -12.6
2016	S. Chatterjee, A. J. Pal, J. Phys. Chem. C 2016, 120, 1428.	3.5 - 8.23
2016	D. Yang, X. Zhou, R. Yang, Z. Yang, W. Yu, X. Wang, C. Li, S. Liu, R. P. H. Chang, Energy Environ. Sci. 2016, 9, 3071.	17.25 - 19.62
2016	H. Zhang, J. Cheng, F. Lin, H. He, J. Mao, K. S. Wong, A. K.-Y. Jen, W. C. H. Choy, ACS Nano 2016, 10, 1503.	11.25 - 14.53
2016	H. Kim, H. Ohkita, H. Benten, S. Ito, Adv. Mater. 2016, 28, 917.	16.5 - 19.4

2017	X. Ren, D. Yang, Z. Yang, J. Feng, X. Zhu, J. Niu, Y. Liu, W. Zhao, S. F. Liu, ACS Appl. Mater. Interfaces 2017, 9, 2421.	15.13 - 17.57
2017	Q. An, P. Fassl, Y. J. Hofstetter, D. Becker-Koch, A. Bausch, P. E. Hopkinson, Y. Vaynzof, Nano Energy 2017, 39, 400.	11.5 - 18.02
2017	J. Ye, X. Zhang, L. Zhu, H. Zheng, G. Liu, H. Wang, T. Hayat, X. Pan, S. Dai, Sustain. Energy Fuels 2017, 1, 907.	15 -19.21
2017	X. Zhang, Z. Li, Y. Ding, L. Hu, J. Ye, X. Pan, S. Dai, Sustain. Energy Fuels 2017, 1, 1056.	17.5 - 19.19
2017	Y. Wang, S. Xu, J. Deng, L. Gao, R. Soc. Open Sci. 2017, 4, 170980.	10 - 15.79
2017	M. A. Mahmud, N. K. Elumalai, M. B. Upama, D. Wang, K. H. Chan, M. Wright, C. Xu, F. Haque, A. Uddin, Sol. Energy Mater. Sol. Cells 2017, 159, 251.	4 - 8.77
2017	S. You, S. Bi, J. Huang, Q. Jia, Y. Yuan, Y. Xia, Z. Xiao, Z. Sun, J. Liu, S. Sun, Z. Zhao, Chem. - A Eur. J. 2017, 23, 18140.	16 - 19.7
2017	C. Liang, P. Li, Y. Zhang, H. Gu, Q. Cai, X. Liu, J. Wang, H. Wen, G. Shao, J. Power Sources 2017, 372, 235.	13.5 - 16.12
2017	D. Liu, Y. Li, J. Yuan, Q. Hong, G. Shi, D. Yuan, J. Wei, C. Huang, J. Tang, M. Fung, J. Mater. Chem. A 2017, 5, 5701.	13.75 - 17.22
2017	Q. Sun, P. Fassl, D. Becker-Koch, A. Bausch, B. Rivkin, S. Bai, P. E. Hopkinson, H. J. Snaith, Y. Vaynzof, Adv. Energy Mater. 2017, 7, 1700977.	9.5 - 15.5
2017	S. Li, P. Zhang, Y. Wang, H. Sarvari, D. Liu, J. Wu, Y. Yang, Z. Wang, Z. D. Chen, Nano Res. 2017, 10, 1092.	14 - 16.08

Table B4: Average device parameters and standard deviations of the twelve solar cells analysed in Figure 5.7. The active layers of these devices have been exposure to vacuum during the UPS mapping measurements (around 1.5 h) and therefore have slightly lower efficiency than the devices, which were fabricated without exposure to vacuum like in Figure 5.1 (right). Adapted with permission from [140]. Copyright 2018, American Chemical Society.

Sample number	V_{OC} (V)	J_{SC} (mA/cm^2)	FF (%)	PCE (%)
1	0.91 ± 0.04	16.7 ± 1.3	73.8 ± 2.6	11.2 ± 0.9
2	0.79 ± 0.01	17.8 ± 1.0	77.3 ± 1.1	10.9 ± 0.7
3	0.91 ± 0.05	17.3 ± 1.3	75.8 ± 2.1	11.9 ± 0.7
4	0.86 ± 0.02	17.6 ± 1.2	75.3 ± 5.3	11.4 ± 1.4
5	0.88 ± 0.02	17.6 ± 1.9	71.7 ± 1.7	11.1 ± 1.3
6	0.92 ± 0.05	17.8 ± 1.3	73.5 ± 4.3	12.0 ± 1.1
7	0.92 ± 0.04	17.3 ± 1.0	73.8 ± 2.0	11.8 ± 1.2
8	0.91 ± 0.02	18.1 ± 0.9	76.0 ± 0.7	12.6 ± 0.7
9	0.86 ± 0.01	18.1 ± 0.9	77.7 ± 0.7	12.0 ± 0.5
10	0.85 ± 0.07	18.1 ± 1.0	59.9 ± 11.4	9.3 ± 2.4
11	0.80 ± 0.15	18.7 ± 2.7	63.6 ± 14.4	10.1 ± 3.8
12	0.78 ± 0.24	15.6 ± 5.8	60.6 ± 12.4	8.7 ± 5.0

Table B5: Physiochemical properties of all solvents used in Chapter 6 as the antisolvent. 0-13: methanol (MeOH), ethanol (EtOH), 2-propanol (IPA), 1-butanol (BuOH), ethyl acetate (EA), chloroform (CF), chlorobenzene (CB), butyl acetate (BA), 1,2-dichlorobenzene (DCB), anisole (Ani), trifluorotoluene (TFT), diethyl ether (DE), m-xylene (XYL) and toluene (Tolu). Values for density, boiling point and dipole moment are reproduced from PubChem and Wikipedia.

Nr.	Solvent	Density (g/mL)	Boiling point (℃)	Dipole moment
0	MeOH	0.79	65	1.69 D
1	EtOH	0.79	78	1.69 D
2	IPA	0.79	83	1.66 D
3	BuOH	0.81	118	1.66 D
4	EA	0.90	77	1.78 D
5	CF	1.49	61	1.15 D
6	CB	1.11	131	1.69 D
7	BA	0.88	126	1.87 D
8	DCB	1.30	180	2.50 D
9	Ani	1.00	154	2.30 D
10	TFT	1.19	103	2.86 D
11	DE	0.71	35	1.15 D
12	XYL	0.86	139	0.33-0.37 D
13	Tolu	0.87	111	0.36 D

Table B6: The volume that requires to dissolve 100 mg of MAI.

MAI (mg)	MeOH (μl)	EtOH (μl)	IPA (μl)	BuOH (μl)
100	230	510	1540	>4240

Table B7: The volume that requires to dissolve 100 mg of FAI.

FAI (mg)	MeOH (μl)	EtOH (μl)	IPA (μl)	BuOH (μl)
100	170	350	820	1640

C Calculate the PbI_2 Amount from SEM Images

To calculate the PbI_2 content on the surface of the perovskite film, we choose the SEM top view images with a magnification of 10,000, as presented in the a and c panels in the Figure C1, C2 and C3. Then, the SEM images are converted to the binary images using the ImageJ software. The binary images of the corresponding SEM images are shown in the b and d panels in the Figure C1, C2 and C3, where the black pixels represent the PbI_2 phases in the SEM. The PbI_2 content is obtained by dividing the number of the black pixels to the total pixels. The SEM measurements were carried out by Dr. Fabian Paulus.

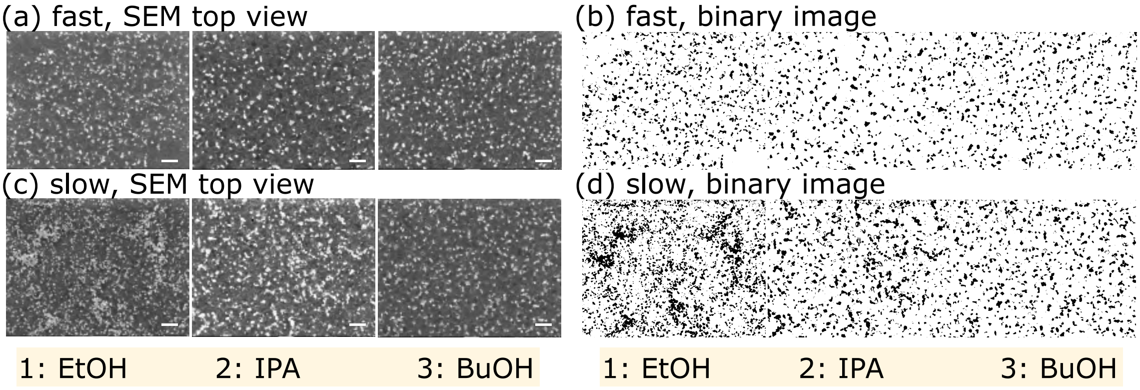

Figure C1: Scanning electron microscopy top view images of the CsMAFA perovskite films fabricated by dripping the antisolvent fast (a) and slow (c). The antisolvents used are EtOH, IPA and BuOH, from left to right. Scale bars represent 1 μm. (b) Binary images of the corresponding SEM images in (a). (d) Binary images of the corresponding SEM images in (c).

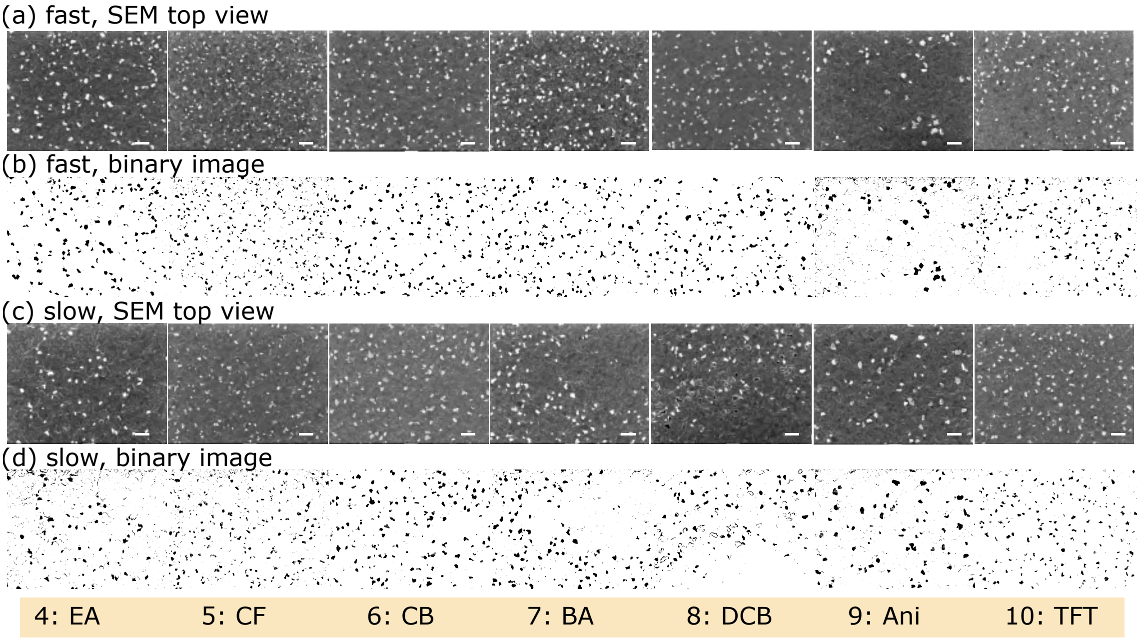

Figure C2: Scanning electron microscopy top view images of the CsMAFA perovskite films fabricated by dripping the antisolvent fast (a) and slow (c). The antisolvents used are EA, CF, CB, BA, DCB, Ani and TFT, from left to right. Scale bars represent 1 μm. (b) Binary images of the corresponding SEM images in (a). (d) Binary images of the corresponding SEM images in (c).

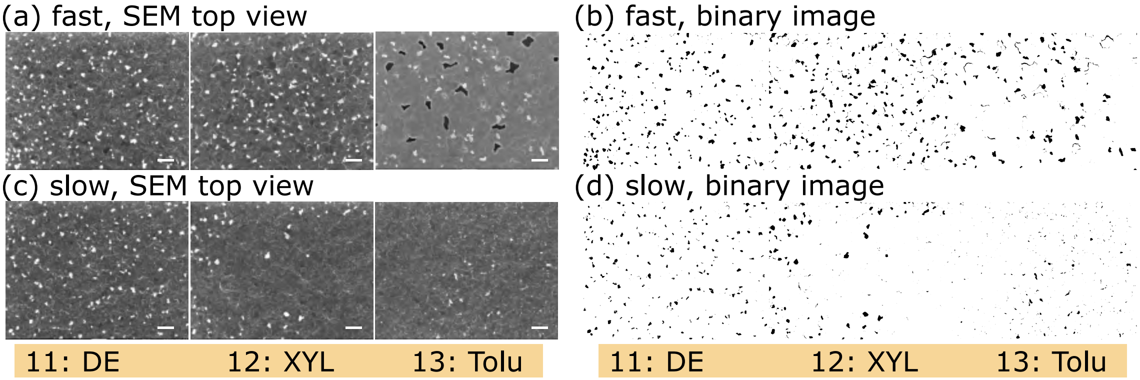

Figure C3: Scanning electron microscopy top view images of the CsMAFA perovskite films fabricated by dripping the antisolvent fast (a) and slow (c). The antisolvents used are DE, XYL and Tolu, from left to right. Scale bars represent 1 μm. (b) Binary images of the corresponding SEM images in (a). (d) Binary images of the corresponding SEM images in (c).

D Abbreviations

Ani	anisole
AFM	atomic force microscopy
BCP	bathocuproine
BA	butyl acetate
BuOH	1-butanol
CB	chlorobenzene
CBM	conduction band minimum
CF	chloroform
CsI	caesium iodide
CsMAFA	triple cation perovskite $Cs_{0.05}(MA_{0.17}FA_{0.83})_{0.95}Pb(I_{0.9}Br_{0.1})_3$ or $Cs_{0.05}(MA_{0.17}FA_{0.83})_{0.95}Pb(I_{0.83}Br_{0.17})_3$
DE	diethyl ether
DCB	1,2-dichlorobenzene
DMF	dimethylformamide
DMSO	dimethyl sulfoxide
DMF/DMSO	a solution mixture of DMF and DMSO at a volume ratio of 4:1
EA	ethyl acetate
ETL	electron transport layer
EtOH	ethanol
FAI	formamidinium iodide, $CH(NH_2)_2I$
FF	fill factor
GBL	γ-butyrolactone
HBL	hole blocking layer
HPA	hypophosporous acid solution
HTL	hole transport layer
IPA	2-propanol (also called isopropanol)
ITO	indium tin oxide
IP	ionization potential
J_{SC}	short-circuit current density
Li-TFSI	lithium bis(trifluoromethylsulfonyl)imide
MAI	methylammonium iodide, $CHNH_3I$
$MAPbI_3$	methylammonium lead triiodide, $CH_3NH_3PbI_3$
MeOH	methanol
OPVs	organic photovoltaics
TFT	trifluorotoluene
Tolu	toluene
$Pb(OAc)_2{\cdot}3H_2O$	lead acetate trihydrate

PbI_2	lead iodide
$PbBr_2$	lead bromide
$PC_{61}BM$	[6,6]-phenyl C61 butyric acid methyl ester
PCE	power conversion efficiency
PDS	photothermal deflection spectroscopy
PEDOT:PSS	poly (3, 4-ethylenedioxythiopene)-poly (styrenesulfonate)
PFN-P_2	[(9,9-bis(3'-(N,N-dimethylamino)propyl)-2,7-fluorene)-alt-2,7-(9,9–dioctylfluorene)]
PLQE	photoluminescence Quantum Efficiency
PTAA	poly(triaryl amine), poly[bis(4-phenyl)(2,4,6-trimethyl-phenyl)amine]
PV	photovoltaic
RbCsMAFA	quadruple cation perovskite
SEM	scanning Electron Microscopy
Spiro-OMeTAD	2,20,7,70-Tetrakis[N,N-di(4-methoxyphenyl)amino]-9,90-spirobifluorene
VBM	valence band maximum
UV	ultra-violet
UV-vis	ultra-violet and visible spectroscopy
UPS	ultra-violet photoemission spectroscopy
V_{OC}	open-circuit voltage
WF	work function
w.r.t.	write with respect to
XPS	X-ray photoemission spectroscopy
XRD	X-ray diffraction
XYL	p-xylene

References

[1] Siemens, W. (1885). on the electromotive action of illuminated selenium, discovered by Mr. Fritts of New York. *The London, Edinburgh, and Dublin Philosophical Magazine and Journal of Science*, 19, 315–316.

[2] NREL (2019). Best Research-Cell Efficiencies Chart by NREL (accessed on August 2019). URL: `https://www.nrel.gov/pv/assets/pdfs/pv-efficiency-chart.20190802.pdf`.

[3] Kojima, A., Teshima, K., Shirai, Y., and Miyasaka, T. (2009). Organometal Halide Perovskites as Visible-Light Sensitizers for Photovoltaic Cells. *Journal of the American Chemical Society*, 131, 6050–6051.

[4] Kim, H. S., Lee, C. R., Im, J. H., Lee, K. B., Moehl, T., Marchioro, A., Moon, S. J., Humphry-Baker, R., Yum, J. H., Moser, J. E., Grätzel, M., and Park, N. G. (2012). Lead iodide perovskite sensitized all-solid-state submicron thin film mesoscopic solar cell with efficiency exceeding 9%. *Scientific Reports*, 2.

[5] Lee, M. M., Teuscher, J., Miyasaka, T., Murakami, T. N., and Snaith, H. J. (2012). Efficient Hybrid Solar Cells Based on Meso-Superstructured Organometal Halide Perovskites. *Science*, 338, 643–647.

[6] Yang, W. S., Noh, J. H., Jeon, N. J., Kim, Y. C., Ryu, S., Seo, J., and Seok, S. I. (2015). High-performance photovoltaic perovskite layers fabricated through intramolecular exchange. *Science*, 348, 1234–1237.

[7] Jeon, N. J., Noh, J. H., Yang, W. S., Kim, Y. C., Ryu, S., Seo, J., and Seok, S. I. (2015). Compositional engineering of perovskite materials for high-performance solar cells. *Nature*, 517, 476–480.

[8] Saliba, M., Matsui, T., Seo, J.-Y., Domanski, K., Correa-Baena, J.-P., Nazeeruddin, M. K., Zakeeruddin, S. M., Tress, W., Abate, A., Hagfeldt, A., and Grätzel, M. (2016). Cesium-containing triple cation perovskite solar cells: improved stability, reproducibility and high efficiency. *Energy & Environmental Science*, 9, 1989–1997.

[9] TheNoise (2007). A p-n junction in thermal equilibrium with zero bias voltage applied. Electron and holes concentration are reported respectively with blue and red lines. Gray regions are charge neutral. Light red zone is positively charged. Light blue zone is negatively charged. URL: `https://en.wikipedia.org/wiki/File:Pn-junction-equilibrium.png`.

[10] Noh, J. H., Im, S. H., Heo, J. H., Mandal, T. N., and Seok, S. I. (2013). Chemical Management for Colorful, Efficient, and Stable Inorganic–Organic Hybrid Nanostructured Solar Cells. *Nano Letters*, 13, 1764–1769.

[11] Eperon, G. E., Stranks, S. D., Menelaou, C., Johnston, M. B., Herz, L. M., and Snaith, H. J. (2014). Formamidinium lead trihalide: a broadly tunable

perovskite for efficient planar heterojunction solar cells. *Energy & Environmental Science*, 7, 982.

[12] Stranks, S. D., Eperon, G. E., Grancini, G., Menelaou, C., Alcocer, M. J. P., Leijtens, T., Herz, L. M., Petrozza, A., and Snaith, H. J. (2013). Electron-Hole Diffusion Lengths Exceeding 1 Micrometer in an Organometal Trihalide Perovskite Absorber. *Science*, 342, 341–344.

[13] D'Innocenzo, V., Grancini, G., Alcocer, M. J. P., Kandada, A. R. S., Stranks, S. D., Lee, M. M., Lanzani, G., Snaith, H. J., and Petrozza, A. (2014). Excitons versus free charges in organo-lead tri-halide perovskites. *Nature Communications*, 5, 3586.

[14] Understanding the Outstanding Power Conversion Efficiency of Perovskite-Based Solar Cells (2015). *Angewandte Chemie International Edition*, 54, 9757–9759.

[15] Rühle, S. (2016). Tabulated values of the Shockley–Queisser limit for single junction solar cells. *Solar Energy*, 130, 139–147.

[16] Shockley, W. (1949). The Theory of p-n Junctions in Semiconductors and p-n Junction Transistors. *Bell System Technical Journal*, 28, 435–489.

[17] Leibold, D. (2017). New Acceptor Molecules for Bulk Heterojunction Organic Solar Cells. Master Thesis. Heidelberg University.

[18] Seaman, C. H. (1982). Calibration of solar cells by the reference cell method—The spectral mismatch problem. *Solar Energy*, 29, 291–298.

[19] Bisquert, J. (2018). The physics of solar cells : perovskites, organics, and photovoltaic fundamentals. 1st ed. Castello, Spain: CRC Press.

[20] Hirst, L. C. and Ekins-Daukes, N. J. (2011). Fundamental losses in solar cells. *Progress in Photovoltaics: Research and Applications*, 19, 286–293.

[21] Shockley, W. and Queisser, H. J. (1961). Detailed Balance Limit of Efficiency of p-n Junction Solar Cells. *Journal of Applied Physics*, 32, 510–519.

[22] Fu, Q., Tang, X., Huang, B., Hu, T., Tan, L., Chen, L., and Chen, Y. (2018). Recent Progress on the Long-Term Stability of Perovskite Solar Cells. *Advanced Science*, 5, 1700387.

[23] Im, J. H., Lee, C. R., Lee, J. W., Park, S. W., and Park, N. G. (2011). 6.5% efficient perovskite quantum-dot-sensitized solar cell. *Nanoscale*, 3, 4088–4093.

[24] Liu, M., Johnston, M. B., and Snaith, H. J. (2013). Efficient planar heterojunction perovskite solar cells by vapour deposition. *Nature*, 501, 395–398.

[25] Eperon, G. E., Burlakov, V. M., Docampo, P., Goriely, A., and Snaith, H. J. (2014). Morphological Control for High Performance, Solution-Processed Planar Heterojunction Perovskite Solar Cells. *Advanced Functional Materials*, 24, 151–157.

[26] Jeng, J.-Y., Chiang, Y.-F., Lee, M.-H., Peng, S.-R., Guo, T.-F., Chen, P., and Wen, T.-C. (2013). CH 3 NH 3 PbI 3 Perovskite/Fullerene Planar-Heterojunction Hybrid Solar Cells. *Advanced Materials*, 25, 3727–3732.

[27] You, J., Yang, Y. (, Hong, Z., Song, T.-B., Meng, L., Liu, Y., Jiang, C., Zhou, H., Chang, W.-H., Li, G., and Yang, Y. (2014). Moisture assisted perovskite

film growth for high performance solar cells. *Applied Physics Letters*, 105, 183902.

[28] Wu, C.-G., Chiang, C.-H., Tseng, Z.-L., Nazeeruddin, M. K., Hagfeldt, A., and Grätzel, M. (2015). High efficiency stable inverted perovskite solar cells without current hysteresis. *Energy & Environmental Science*, 8, 2725–2733.

[29] Nie, W., Tsai, H., Asadpour, R., Blancon, J.-C., Neukirch, A. J., Gupta, G., Crochet, J. J., Chhowalla, M., Tretiak, S., Alam, M. A., Wang, H.-L., and Mohite, A. D. (2015). High-efficiency solution-processed perovskite solar cells with millimeter-scale grains. *Science*, 347, 522–525.

[30] Meloni, S., Palermo, G., Ashari-Astani, N., Grätzel, M., and Rothlisberger, U. (2016). Valence and conduction band tuning in halide perovskites for solar cell applications. *Journal of Materials Chemistry A*, 4, 15997–16002.

[31] Hao, F., Stoumpos, C. C., Cao, D. H., Chang, R. P. H., and Kanatzidis, M. G. (2014). Lead-free solid-state organic–inorganic halide perovskite solar cells. *Nature Photonics*, 8, 489–494.

[32] Pellet, N., Gao, P., Gregori, G., Yang, T.-Y., Nazeeruddin, M. K., Maier, J., and Grätzel, M. (2014). Mixed-Organic-Cation Perovskite Photovoltaics for Enhanced Solar-Light Harvesting. *Angewandte Chemie International Edition*, 53, 3151–3157.

[33] Stoumpos, C. C., Malliakas, C. D., and Kanatzidis, M. G. (2013). Semiconducting Tin and Lead Iodide Perovskites with Organic Cations: Phase Transitions, High Mobilities, and Near-Infrared Photoluminescent Properties. *Inorganic Chemistry*, 52, 9019–9038.

[34] Leguy, A. M. A., Azarhoosh, P., Alonso, M. I., Campoy-Quiles, M., Weber, O. J., Yao, J., Bryant, D., Weller, M. T., Nelson, J., Walsh, A., Schilfgaarde, M. van, and Barnes, P. R. F. (2016). Experimental and theoretical optical properties of methylammonium lead halide perovskites. *Nanoscale*, 8, 6317–6327.

[35] Miyata, A., Mitioglu, A., Plochocka, P., Portugall, O., Wang, J. T.-W., Stranks, S. D., Snaith, H. J., and Nicholas, R. J. (2015). Direct measurement of the exciton binding energy and effective masses for charge carriers in organic–inorganic tri-halide perovskites. *Nature Physics*, 11, 582–587.

[36] Lin, Q., Armin, A., Nagiri, R. C. R., Burn, P. L., and Meredith, P. (2015). Electro-optics of perovskite solar cells. *Nature Photonics*, 9, 106–112.

[37] Hu, M., Bi, C., Yuan, Y., Xiao, Z., Dong, Q., Shao, Y., and Huang, J. (2015). Distinct Exciton Dissociation Behavior of Organolead Trihalide Perovskite and Excitonic Semiconductors Studied in the Same System. *Small*, 11, 2164–2169.

[38] Xing, G., Mathews, N., Sun, S., Lim, S. S., Lam, Y. M., Gratzel, M., Mhaisalkar, S., and Sum, T. C. (2013). Long-Range Balanced Electron- and Hole-Transport Lengths in Organic-Inorganic CH3NH3PbI3. *Science*, 342, 344–347.

[39] Wehrenfennig, C., Eperon, G. E., Johnston, M. B., Snaith, H. J., and Herz, L. M. (2014). High Charge Carrier Mobilities and Lifetimes in Organolead Trihalide Perovskites. *Advanced Materials*, 26, 1584–1589.

[40] Colella, S., Mosconi, E., Fedeli, P., Listorti, A., Gazza, F., Orlandi, F., Ferro, P., Besagni, T., Rizzo, A., Calestani, G., Gigli, G., De Angelis, F., and Mosca, R. (2013). MAPbI 3-x Cl x Mixed Halide Perovskite for Hybrid Solar Cells: The Role of Chloride as Dopant on the Transport and Structural Properties. *Chemistry of Materials*, 25, 4613–4618.

[41] Jacobsson, T. J., Svanström, S., Andrei, V., Rivett, J. P. H., Kornienko, N., Philippe, B., Cappel, U. B., Rensmo, H., Deschler, F., and Boschloo, G. (2018). Extending the Compositional Space of Mixed Lead Halide Perovskites by Cs, Rb, K, and Na Doping. *The Journal of Physical Chemistry C*, 122, 13548–13557.

[42] Goldschmidt, V. M. (1929). Crystal structure and chemical constitution. *Transactions of the Faraday Society*, 25, 253.

[43] Filip, M. R., Eperon, G. E., Snaith, H. J., and Giustino, F. (2014). Steric engineering of metal-halide perovskites with tunable optical band gaps. *Nature Communications*, 5, 5757.

[44] Kieslich, G., Sun, S., and Cheetham, A. K. (2014). Solid-state principles applied to organic–inorganic perovskites: new tricks for an old dog. *Chem. Sci.*, 5, 4712–4715.

[45] Travis, W., Glover, E. N. K., Bronstein, H., Scanlon, D. O., and Palgrave, R. G. (2016). On the application of the tolerance factor to inorganic and hybrid halide perovskites: a revised system. *Chemical Science*, 7, 4548–4556.

[46] Whitfield, P. S., Herron, N., Guise, W. E., Page, K., Cheng, Y. Q., Milas, I., and Crawford, M. K. (2016). Structures, Phase Transitions and Tricritical Behavior of the Hybrid Perovskite Methyl Ammonium Lead Iodide. *Scientific Reports*, 6, 35685.

[47] Leijtens, T., Bush, K., Cheacharoen, R., Beal, R., Bowring, A., and McGehee, M. D. (2017). Towards enabling stable lead halide perovskite solar cells; interplay between structural, environmental, and thermal stability. *Journal of Materials Chemistry A*, 5, 11483–11500.

[48] Conings, B., Drijkoningen, J., Gauquelin, N., Babayigit, A., D'Haen, J., D'Olieslaeger, L., Ethirajan, A., Verbeeck, J., Manca, J., Mosconi, E., Angelis, F. D., and Boyen, H.-G. (2015). Intrinsic Thermal Instability of Methylammonium Lead Trihalide Perovskite. *Advanced Energy Materials*, 5, 1500477.

[49] Kim, N.-K., Min, Y. H., Noh, S., Cho, E., Jeong, G., Joo, M., Ahn, S.-W., Lee, J. S., Kim, S., Ihm, K., Ahn, H., Kang, Y., Lee, H.-S., and Kim, D. (2017). Investigation of Thermally Induced Degradation in CH3NH3PbI3 Perovskite Solar Cells using In-situ Synchrotron Radiation Analysis. *Scientific Reports*, 7, 4645.

[50] Habisreutinger, S. N., Leijtens, T., Eperon, G. E., Stranks, S. D., Nicholas, R. J., and Snaith, H. J. (2014). Carbon Nanotube/Polymer Composites as a Highly Stable Hole Collection Layer in Perovskite Solar Cells. *Nano Letters*, 14, 5561–5568.

[51] Li, B., Li, Y., Zheng, C., Gao, D., and Huang, W. (2016). Advancements in the stability of perovskite solar cells: degradation mechanisms and improvement approaches. *RSC Advances*, 6, 38079–38091.

[52] Wang, D., Wright, M., Elumalai, N. K., and Uddin, A. (2016). Stability of perovskite solar cells. *Solar Energy Materials and Solar Cells*, 147, 255–275.

[53] Aristidou, N., Sanchez-Molina, I., Chotchuangchutchaval, T., Brown, M., Martinez, L., Rath, T., and Haque, S. A. (2015). The Role of Oxygen in the Degradation of Methylammonium Lead Trihalide Perovskite Photoactive Layers. *Angewandte Chemie International Edition*, 54, 8208–8212.

[54] Pearson, A. J., Eperon, G. E., Hopkinson, P. E., Habisreutinger, S. N., Wang, J. T.-W., Snaith, H. J., and Greenham, N. C. (2016). Oxygen Degradation in Mesoporous Al 2 O 3 /CH 3 NH 3 PbI 3- x Cl x Perovskite Solar Cells: Kinetics and Mechanisms. *Advanced Energy Materials*, 6, 1600014.

[55] Bryant, D., Aristidou, N., Pont, S., Sanchez-Molina, I., Chotchunangatchaval, T., Wheeler, S., Durrant, J. R., and Haque, S. A. (2016). Light and oxygen induced degradation limits the operational stability of methylammonium lead triiodide perovskite solar cells. *Energy & Environmental Science*, 9, 1655–1660.

[56] Pont, S., Bryant, D., Lin, C.-T., Aristidou, N., Wheeler, S., Ma, X., Godin, R., Haque, S. A., and Durrant, J. R. (n.d.). Materials Chemistry A Materials for energy and sustainability Tuning CH 3 NH 3 Pb(I 1Àx Br x) 3 perovskite oxygen stability in thin films and solar cells †. 5 (), 9423–10050.

[57] Abdelmageed, G., Jewell, L., Hellier, K., Seymour, L., Luo, B., Bridges, F., Zhang, J. Z., and Carter, S. (2016). Mechanisms for light induced degradation in MAPbI3 perovskite thin films and solar cells. *Citation: Applied Physics Letters*, 109, 185901.

[58] Sun, Q., Fassl, P., Becker-Koch, D., Bausch, A., Rivkin, B., Bai, S., Hopkinson, P. E., Snaith, H. J., and Vaynzof, Y. (2017). Role of Microstructure in Oxygen Induced Photodegradation of Methylammonium Lead Triiodide Perovskite Films. *Advanced Energy Materials*, 7, 1700977.

[59] Koh, T. M., Fu, K., Fang, Y., Chen, S., Sum, T. C., Mathews, N., Mhaisalkar, S. G., Boix, P. P., and Baikie, T. (2014). Formamidinium-Containing Metal-Halide: An Alternative Material for Near-IR Absorption Perovskite Solar Cells. *The Journal of Physical Chemistry C*, 118, 16458–16462.

[60] MØLLER, C. K. (1958). Crystal Structure and Photoconductivity of Cæsium Plumbohalides. *Nature*, 182, 1436–1436.

[61] Binek, A., Hanusch, F. C., Docampo, P., and Bein, T. (2015). Stabilization of the Trigonal High-Temperature Phase of Formamidinium Lead Iodide. *The Journal of Physical Chemistry Letters*, 6, 1249–1253.

[62] Lee, J.-W., Kim, D.-H., Kim, H.-S., Seo, S.-W., Cho, S. M., and Park, N.-G. (2015). Formamidinium and Cesium Hybridization for Photo- and Moisture-Stable Perovskite Solar Cell. *Advanced Energy Materials*, 5, 1501310.

[63] Yi, C., Luo, J., Meloni, S., Boziki, A., Ashari-Astani, N., Grätzel, C., Zakeeruddin, S. M., Röthlisberger, U., and Grätzel, M. (2016). Entropic stabi-

lization of mixed A-cation ABX 3 metal halide perovskites for high performance perovskite solar cells. *Energy & Environmental Science*, 9, 656–662.

[64] Choi, H., Jeong, J., Kim, H.-B., Kim, S., Walker, B., Kim, G.-H., and Kim, J. Y. (2014). Cesium-doped methylammonium lead iodide perovskite light absorber for hybrid solar cells. *Nano Energy*, 7, 80–85.

[65] Saliba, M., Matsui, T., Domanski, K., Seo, J.-Y., Ummadisingu, A., Zakeeruddin, S. M., Correa-Baena, J.-P., Tress, W. R., Abate, A., Hagfeldt, A., and Gratzel, M. (2016). Incorporation of rubidium cations into perovskite solar cells improves photovoltaic performance. *Science*, 354, 206–209.

[66] Nam, J. K., Chai, S. U., Cha, W., Choi, Y. J., Kim, W., Jung, M. S., Kwon, J., Kim, D., and Park, J. H. (2017). Potassium Incorporation for Enhanced Performance and Stability of Fully Inorganic Cesium Lead Halide Perovskite Solar Cells. *Nano Letters*, 17, 2028–2033.

[67] De Marco, N., Zhou, H., Chen, Q., Sun, P., Liu, Z., Meng, L., Yao, E.-P., Liu, Y., Schiffer, A., and Yang, Y. (2016). Guanidinium: A Route to Enhanced Carrier Lifetime and Open-Circuit Voltage in Hybrid Perovskite Solar Cells. *Nano Letters*, 16, 1009–1016.

[68] Burschka, J., Pellet, N., Moon, S.-J., Humphry-Baker, R., Gao, P., Nazeeruddin, M. K., and Grätzel, M. (2013). Sequential deposition as a route to high-performance perovskite-sensitized solar cells. *Nature*, 499, 316–319.

[69] Yang, Z., Chueh, C.-C., Zuo, F., Kim, J. H., Liang, P.-W., and Jen, A. K.-Y. (2015). High-Performance Fully Printable Perovskite Solar Cells via Blade-Coating Technique under the Ambient Condition. *Advanced Energy Materials*, 5, 1500328.

[70] Hwang, K., Jung, Y.-S., Heo, Y.-J., Scholes, F. H., Watkins, S. E., Subbiah, J., Jones, D. J., Kim, D.-Y., and Vak, D. (2015). Toward Large Scale Roll-to-Roll Production of Fully Printed Perovskite Solar Cells. *Advanced Materials*, 27, 1241–1247.

[71] Li, S.-G., Jiang, K.-J., Su, M.-J., Cui, X.-P., Huang, J.-H., Zhang, Q.-Q., Zhou, X.-Q., Yang, L.-M., and Song, Y.-L. (2015). Inkjet printing of CH 3 NH 3 PbI 3 on a mesoscopic TiO 2 film for highly efficient perovskite solar cells. *Journal of Materials Chemistry A*, 3, 9092–9097.

[72] Razza, S., Castro-Hermosa, S., Di Carlo, A., and Brown, T. M. (2016). Research Update: Large-area deposition, coating, printing, and processing techniques for the upscaling of perovskite solar cell technology. *APL Materials*, 4, 091508.

[73] Chen, Y., He, M., Peng, J., Sun, Y., and Liang, Z. (2016). Structure and Growth Control of Organic-Inorganic Halide Perovskites for Optoelectronics: From Polycrystalline Films to Single Crystals. *Advanced Science*, 3, 1500392.

[74] Jeon, N. J., Noh, J. H., Kim, Y. C., Yang, W. S., Ryu, S., and Seok, S. I. (2014). Solvent engineering for high-performance inorganic-organic hybrid perovskite solar cells. *Nature Materials*, 13, 897–903.

[75] Ahn, N., Son, D.-Y., Jang, I.-H., Kang, S. M., Choi, M., and Park, N.-G. (2015). Highly Reproducible Perovskite Solar Cells with Average Efficiency

of 18.3% and Best Efficiency of 19.7% Fabricated via Lewis Base Adduct of Lead(II) Iodide. *Journal of the American Chemical Society*, 137, 8696–8699.

[76] Heo, J. H., Im, S. H., Noh, J. H., Mandal, T. N., Lim, C.-S., Chang, J. A., Lee, Y. H., Kim, H.-j., Sarkar, A., Nazeeruddin, M. K., Grätzel, M., and Seok, S. I. (2013). Efficient inorganic–organic hybrid heterojunction solar cells containing perovskite compound and polymeric hole conductors. *Nature Photonics*, 7, 486–491.

[77] Yan, K., Long, M., Zhang, T., Wei, Z., Chen, H., Yang, S., and Xu, J. (2015). Hybrid Halide Perovskite Solar Cell Precursors: Colloidal Chemistry and Coordination Engineering behind Device Processing for High Efficiency. *Journal of the American Chemical Society*, 137, 4460–4468.

[78] Petrov, A. A., Sokolova, I. P., Belich, N. A., Peters, G. S., Dorovatovskii, P. V., Zubavichus, Y. V., Khrustalev, V. N., Petrov, A. V., Grätzel, M., Goodilin, E. A., and Tarasov, A. B. (2017). Crystal Structure of DMF-Intermediate Phases Uncovers the Link Between CH 3 NH 3 PbI 3 Morphology and Precursor Stoichiometry. *The Journal of Physical Chemistry C*, 121, 20739–20743.

[79] Aldibaja, F. K., Badia, L., Mas-Marzá, E., Sánchez, R. S., Barea, E. M., and Mora-Sero, I. (2015). Effect of different lead precursors on perovskite solar cell performance and stability. *Journal of Materials Chemistry A*, 3, 9194–9200.

[80] Moore, D. T., Sai, H., Tan, K. W., Smilgies, D.-M., Zhang, W., Snaith, H. J., Wiesner, U., and Estroff, L. A. (2015). Crystallization Kinetics of Organic–Inorganic Trihalide Perovskites and the Role of the Lead Anion in Crystal Growth. *Journal of the American Chemical Society*, 137, 2350–2358.

[81] Dualeh, A., Gao, P., Seok, S. I., Nazeeruddin, M. K., and Grätzel, M. (2014). Thermal Behavior of Methylammonium Lead-Trihalide Perovskite Photovoltaic Light Harvesters. *Chemistry of Materials*, 26, 6160–6164.

[82] Zhang, W., Saliba, M., Moore, D. T., Pathak, S. K., Hörantner, M. T., Stergiopoulos, T., Stranks, S. D., Eperon, G. E., Alexander-Webber, J. A., Abate, A., Sadhanala, A., Yao, S., Chen, Y., Friend, R. H., Estroff, L. A., Wiesner, U., and Snaith, H. J. (2015). Ultrasmooth organic–inorganic perovskite thin-film formation and crystallization for efficient planar heterojunction solar cells. *Nature Communications*, 6, 6142.

[83] Ling, L., Yuan, S., Wang, P., Zhang, H., Tu, L., Wang, J., Zhan, Y., and Zheng, L. (2016). Precisely Controlled Hydration Water for Performance Improvement of Organic-Inorganic Perovskite Solar Cells. *Advanced Functional Materials*, 26, 5028–5034.

[84] Zhang, W., Pathak, S., Sakai, N., Stergiopoulos, T., Nayak, P. K., Noel, N. K., Haghighirad, A. A., Burlakov, V. M., DeQuilettes, D. W., Sadhanala, A., Li, W., Wang, L., Ginger, D. S., Friend, R. H., and Snaith, H. J. (2015). Enhanced optoelectronic quality of perovskite thin films with hypophosphorous acid for planar heterojunction solar cells. *Nature Communications*, 6, 10030.

[85] Xiao, M., Huang, F., Huang, W., Dkhissi, Y., Zhu, Y., Etheridge, J., Gray-Weale, A., Bach, U., Cheng, Y.-B., and Spiccia, L. (2014). A Fast Deposition-

Crystallization Procedure for Highly Efficient Lead Iodide Perovskite Thin-Film Solar Cells. *Angewandte Chemie International Edition*, 53, 9898–9903.

[86] Wharf, I., Gramstad, T., Makhija, R., and Onyszchuk, M. (1976). Synthesis and vibrational spectra of some lead(II) halide adducts with O-, S-, and N-donor atom ligands. *Canadian Journal of Chemistry*, 54, 3430–3438.

[87] Bi, D., Tress, W., Dar, M. I., Gao, P., Luo, J., Renevier, C., Schenk, K., Abate, A., Giordano, F., Correa Baena, J.-P., Decoppet, J.-d., Zakeeruddin, S. M., Nazeeruddin, M. K., Grätzel, M., and Hagfeldt, A. (2016). Efficient luminescent solar cells based on tailored mixed-cation perovskites. *Science Advances*, 2, e1501170.

[88] Bu, T., Wu, L., Liu, X., Yang, X., Zhou, P., Yu, X., Qin, T., Shi, J., Wang, S., Li, S., Ku, Z., Peng, Y., Huang, F., Meng, Q., Cheng, Y.-B., and Zhong, J. (2017). Synergic Interface Optimization with Green Solvent Engineering in Mixed Perovskite Solar Cells. *Advanced Energy Materials*, 7, 1700576.

[89] Paek, S., Schouwink, P., Athanasopoulou, E. N., Cho, K. T., Grancini, G., Lee, Y., Zhang, Y., Stellacci, F., Nazeeruddin, M. K., and Gao, P. (2017). From Nano- to Micrometer Scale: The Role of Antisolvent Treatment on High Performance Perovskite Solar Cells. *Chemistry of Materials*, 29, 3490–3498.

[90] Zhao, P., Kim, B. J., Ren, X., Lee, D. G., Bang, G. J., Jeon, J. B., Kim, W. B., and Jung, H. S. (2018). Antisolvent with an Ultrawide Processing Window for the One-Step Fabrication of Efficient and Large-Area Perovskite Solar Cells. *Advanced Materials*, 30, 1802763.

[91] Wang, Y., Wu, J., Zhang, P., Liu, D., Zhang, T., Ji, L., Gu, X., David Chen, Z., and Li, S. (2017). Stitching triple cation perovskite by a mixed anti-solvent process for high performance perovskite solar cells. *Nano Energy*, 39, 616–625.

[92] Liu, X., Wang, C., Lyu, L., Wang, C., Xiao, Z., Bi, C., Huang, J., and Gao, Y. (2015). Electronic structures at the interface between Au and CH 3 NH 3 PbI 3. *Physical Chemistry Chemical Physics*, 17, 896–902.

[93] Miller, E. M., Zhao, Y., Mercado, C. C., Saha, S. K., Luther, J. M., Zhu, K., Stevanović, V., Perkins, C. L., and Lagemaat, J. van de (2014). Substrate-controlled band positions in CH 3 NH 3 PbI 3 perovskite films. *Phys. Chem. Chem. Phys.*, 16, 22122–22130.

[94] Schulz, P., Edri, E., Kirmayer, S., Hodes, G., Cahen, D., and Kahn, A. (2014). Interface energetics in organo-metal halide perovskite-based photovoltaic cells. *Energy & Environmental Science*, 7, 1377.

[95] Wang, Q., Shao, Y., Xie, H., Lyu, L., Liu, X., Gao, Y., and Huang, J. (2014). Qualifying composition dependent p and n self-doping in CH 3 NH 3 PbI 3. *Applied Physics Letters*, 105, 163508.

[96] Lindblad, R., Bi, D., Park, B. W., Oscarsson, J., Gorgoi, M., Siegbahn, H., Odelius, M., Johansson, E. M., and Rensmo, H. (2014). Electronic structure of TiO2/CH3NH 3PbI3 perovskite solar cell interfaces. *Journal of Physical Chemistry Letters*, 5, 648–653.

[97] Lo, M.-F., Guan, Z.-Q., Ng, T.-W., Chan, C.-Y., and Lee, C.-S. (2015). Electronic Structures and Photoconversion Mechanism in Perovskite/Fullerene Heterojunctions. *Advanced Functional Materials*, 25, 1213–1218.

[98] An, Q., Sun, Q., Weu, A., Becker-Koch, D., Paulus, F., Arndt, S., Stuck, F., Hashmi, A. S. K., Tessler, N., and Vaynzof, Y. (2019). Enhancing the Open-Circuit Voltage of Perovskite Solar Cells by up to 120 mV Using π-Extended Phosphoniumfluorene Electrolytes as Hole Blocking Layers. *Advanced Energy Materials*, 1901257.

[99] Jung, H. S. and Park, N. G. (2015). Perovskite solar cells: From materials to devices. *Small*, 11, 10–25.

[100] Liu, T., Chen, K., Hu, Q., Zhu, R., and Gong, Q. (2016). Inverted Perovskite Solar Cells: Progresses and Perspectives. *Advanced Energy Materials*, 6, 1600457.

[101] Hu, H., Wang, D., Zhou, Y., Zhang, J., Lv, S., Pang, S., Chen, X., Liu, Z., Padture, N. P., and Cui, G. (2014). Vapour-based processing of hole-conductor-free CH 3 NH 3 PbI 3 perovskite/C 60 fullerene planar solar cells. *RSC Adv.*, 4, 28964–28967.

[102] Shi, J., Xu, X., Li, D., and Meng, Q. (2015). Interfaces in Perovskite Solar Cells. *Small*, 11, 2472–2486.

[103] Lim, K.-G., Kim, H.-B., Jeong, J., Kim, H., Kim, J. Y., and Lee, T.-W. (2014). Boosting the Power Conversion Efficiency of Perovskite Solar Cells Using Self-Organized Polymeric Hole Extraction Layers with High Work Function. *Advanced Materials*, 26, 6461–6466.

[104] Jeng, J.-Y., Chen, K.-C., Chiang, T.-Y., Lin, P.-Y., Tsai, T.-D., Chang, Y.-C., Guo, T.-F., Chen, P., Wen, T.-C., and Hsu, Y.-J. (2014). Nickel Oxide Electrode Interlayer in CH 3 NH 3 PbI 3 Perovskite/PCBM Planar-Heterojunction Hybrid Solar Cells. *Advanced Materials*, 26, 4107–4113.

[105] Hou, Y., Chen, W., Baran, D., Stubhan, T., Luechinger, N. A., Hartmeier, B., Richter, M., Min, J., Chen, S., Quiroz, C. O. R., Li, N., Zhang, H., Heumueller, T., Matt, G. J., Osvet, A., Forberich, K., Zhang, Z.-G., Li, Y., Winter, B., Schweizer, P., Spiecker, E., and Brabec, C. J. (2016). Overcoming the Interface Losses in Planar Heterojunction Perovskite-Based Solar Cells. *Advanced Materials*, 28, 5112–5120.

[106] Tvingstedt, K., Gil-Escrig, L., Momblona, C., Rieder, P., Kiermasch, D., Sessolo, M., Baumann, A., Bolink, H. J., and Dyakonov, V. (2017). Removing Leakage and Surface Recombination in Planar Perovskite Solar Cells. *ACS Energy Letters*, 2, 424–430.

[107] Jong, M. P. de, IJzendoorn, L. J. van, and Voigt, M. J. A. de (2000). Stability of the interface between indium-tin-oxide and poly(3,4-ethylenedioxythiophene): poly(styrenesulfonate) in polymer light-emitting diodes. *Applied Physics Letters*, 77, 2255–2257.

[108] Jørgensen, M., Norrman, K., and Krebs, F. C. (2008). Stability/degradation of polymer solar cells. *Solar Energy Materials and Solar Cells*, 92, 686–714.

[109] Fan, X., Fang, G., Cheng, F., Qin, P., Huang, H., and Li, Y. (2013). Enhanced performance and stability in PBDTTT-C-T : PC 70 BM polymer solar cells by optimizing thickness of NiO x buffer layers. *Journal of Physics D: Applied Physics*, 46, 305106.

[110] Manders, J. R., Tsang, S.-W., Hartel, M. J., Lai, T.-H., Chen, S., Amb, C. M., Reynolds, J. R., and So, F. (2013). Solution-Processed Nickel Oxide Hole Transport Layers in High Efficiency Polymer Photovoltaic Cells. *Advanced Functional Materials*, 23, 2993–3001.

[111] Zuo, C. and Ding, L. (2017). Modified PEDOT Layer Makes a 1.52 V V oc for Perovskite/PCBM Solar Cells. *Advanced Energy Materials*, 7, 1601193.

[112] Kim, J. H., Liang, P.-W., Williams, S. T., Cho, N., Chueh, C.-C., Glaz, M. S., Ginger, D. S., and Jen, A. K.-Y. (2015). High-Performance and Environmentally Stable Planar Heterojunction Perovskite Solar Cells Based on a Solution-Processed Copper-Doped Nickel Oxide Hole-Transporting Layer. *Advanced Materials*, 27, 695–701.

[113] Zhao, D., Sexton, M., Park, H.-Y., Baure, G., Nino, J. C., and So, F. (2015). High-Efficiency Solution-Processed Planar Perovskite Solar Cells with a Polymer Hole Transport Layer. *Advanced Energy Materials*, 5, n/a–n/a.

[114] Bi, C., Wang, Q., Shao, Y., Yuan, Y., Xiao, Z., and Huang, J. (2015). Non-wetting surface-driven high-aspect-ratio crystalline grain growth for efficient hybrid perovskite solar cells. *Nature Communications*, 6, 7747.

[115] Dong, Q., Yuan, Y., Shao, Y., Fang, Y., Wang, Q., and Huang, J. (2015). Abnormal crystal growth in CH 3 NH 3 PbI 3Àx Cl x using a multi-cycle solution coating process †. *Energy Environ. Sci*, 8, 2464.

[116] Lee, J., Kang, H., Kim, G., Back, H., Kim, J., Hong, S., Park, B., Lee, E., and Lee, K. (2017). Achieving Large-Area Planar Perovskite Solar Cells by Introducing an Interfacial Compatibilizer. *Advanced Materials*, 29, 1606363.

[117] Docampo, P., Ball, J. M., Darwich, M., Eperon, G. E., and Snaith, H. J. (2013). Efficient organometal trihalide perovskite planar-heterojunction solar cells on flexible polymer substrates. *Nature Communications*, 4, 2761.

[118] Shao, Y., Xiao, Z., Bi, C., Yuan, Y., and Huang, J. (2014). Origin and elimination of photocurrent hysteresis by fullerene passivation in CH3NH3PbI3 planar heterojunction solar cells. *Nature Communications*, 5, 5784.

[119] Xu, J., Buin, A., Ip, A. H., Li, W., Voznyy, O., Comin, R., Yuan, M., Jeon, S., Ning, Z., McDowell, J. J., Kanjanaboos, P., Sun, J.-P., Lan, X., Quan, L. N., Kim, D. H., Hill, I. G., Maksymovych, P., and Sargent, E. H. (2015). Perovskite–fullerene hybrid materials suppress hysteresis in planar diodes. *Nature Communications*, 6, 7081.

[120] Heo, J. H., Han, H. J., Kim, D., Ahn, T. K., and Im, S. H. (2015). Hysteresis-less inverted CH 3 NH 3 PbI 3 planar perovskite hybrid solar cells with 18.1% power conversion efficiency. *Energy & Environmental Science*, 8, 1602–1608.

[121] Zhao, Y., Zhou, W., Ma, W., Meng, S., Li, H., Wei, J., Fu, R., Liu, K., Yu, D., and Zhao, Q. (2016). Correlations between Immobilizing Ions and

Suppressing Hysteresis in Perovskite Solar Cells. *ACS Energy Letters*, 1, 266–272.

[122] Park, C., Ko, H., Sin, D. H., Song, K. C., and Cho, K. (2017). Organometal Halide Perovskite Solar Cells with Improved Thermal Stability via Grain Boundary Passivation Using a Molecular Additive. *Advanced Functional Materials*, 27, 1703546.

[123] De Bastiani, M., Dell'Erba, G., Gandini, M., D'Innocenzo, V., Neutzner, S., Kandada, A. R. S., Grancini, G., Binda, M., Prato, M., Ball, J. M., Caironi, M., and Petrozza, A. (2016). Ion Migration and the Role of Preconditioning Cycles in the Stabilization of the J - V Characteristics of Inverted Hybrid Perovskite Solar Cells. *Advanced Energy Materials*, 6, 1501453.

[124] Yuan, D.-X., Yuan, X.-D., Xu, Q.-Y., Xu, M.-F., Shi, X.-B., Wang, Z.-K., and Liao, L.-S. (2015). A solution-processed bathocuproine cathode interfacial layer for high-performance bromine–iodine perovskite solar cells. *Physical Chemistry Chemical Physics*, 17, 26653–26658.

[125] Rivkin, B., Fassl, P., Sun, Q., Taylor, A. D., Chen, Z., and Vaynzof, Y. (2018). Effect of Ion Migration-Induced Electrode Degradation on the Operational Stability of Perovskite Solar Cells. *ACS Omega*, 3, 10042–10047.

[126] Mei, A., Li, X., Liu, L., Ku, Z., Liu, T., Rong, Y., Xu, M., Hu, M., Chen, J., Yang, Y., Gratzel, M., and Han, H. (2014). A hole-conductor-free, fully printable mesoscopic perovskite solar cell with high stability. *Science*, 345, 295–298.

[127] Zhou, H., Chen, Q., Li, G., Luo, S., Song, T.-b., Duan, H.-S., Hong, Z., You, J., Liu, Y., and Yang, Y. (2014). Interface engineering of highly efficient perovskite solar cells. *Science*, 345, 542–546.

[128] Eperon, G. E., Habisreutinger, S. N., Leijtens, T., Bruijnaers, B. J., Franeker, J. J. van, DeQuilettes, D. W., Pathak, S., Sutton, R. J., Grancini, G., Ginger, D. S., Janssen, R. A. J., Petrozza, A., and Snaith, H. J. (2015). The Importance of Moisture in Hybrid Lead Halide Perovskite Thin Film Fabrication. *ACS Nano*, 9, 9380–9393.

[129] Alagona, G., Ghio, C., and Kollman, P. (1986). Monte Carlo simulation studies of the solvation of ions. 1. Acetate anion and methylammonium cation. *Journal of the American Chemical Society*, 108, 185–191.

[130] Leguy, A. M. A., Hu, Y., Campoy-Quiles, M., Alonso, M. I., Weber, O. J., Azarhoosh, P., Schilfgaarde, M. van, Weller, M. T., Bein, T., Nelson, J., Docampo, P., and Barnes, P. R. F. (2015). Reversible Hydration of CH 3 NH 3 PbI 3 in Films, Single Crystals, and Solar Cells. *Chemistry of Materials*, 27, 3397–3407.

[131] Yang, J., Siempelkamp, B. D., Liu, D., and Kelly, T. L. (2015). Investigation of CH 3 NH 3 PbI 3 Degradation Rates and Mechanisms in Controlled Humidity Environments Using in Situ Techniques. *ACS Nano*, 9, 1955–1963.

[132] Song, Z., Abate, A., Watthage, S. C., Liyanage, G. K., Phillips, A. B., Steiner, U., Graetzel, M., and Heben, M. J. (2016). Perovskite Solar Cell Stability in

Humid Air: Partially Reversible Phase Transitions in the PbI 2 -CH 3 NH 3 I-H 2 O System. *Advanced Energy Materials*, 6, 1600846.

[133] Leijtens, T., Giovenzana, T., Habisreutinger, S. N., Tinkham, J. S., Noel, N. K., Kamino, B. A., Sadoughi, G., Sellinger, A., and Snaith, H. J. (2016). Hydrophobic Organic Hole Transporters for Improved Moisture Resistance in Metal Halide Perovskite Solar Cells. *ACS Applied Materials & Interfaces*, 8, 5981–5989.

[134] Aristidou, N., Eames, C., Sanchez-Molina, I., Bu, X., Kosco, J., Islam, M. S., and Haque, S. A. (2017). Fast oxygen diffusion and iodide defects mediate oxygen-induced degradation of perovskite solar cells. *Nature Communications*, 8, 15218.

[135] O'Mahony, F. T. F., Lee, Y. H., Jellett, C., Dmitrov, S., Bryant, D. T. J., Durrant, J. R., O'Regan, B. C., Graetzel, M., Nazeeruddin, M. K., and Haque, S. a. (2015). Improved environmental stability of organic lead trihalide perovskite-based photoactive-layers in the presence of mesoporous TiO 2. *Journal of Materials Chemistry A*, 3, 7219–7223.

[136] GregorioW (2011). Schematic of an atomic force microscope with optical detection of the deflection of the microcantilever. URL: `https://commons.wikimedia.org/wiki/File:AFM_schematic_(EN).svg`.

[137] Steff, A. and MarcoTolo (2010). Diagram of a scanning electron microscope with English captions. URL: `https://en.wikipedia.org/wiki/File:Schema_MEB_(en).svg`.

[138] Lannig, S. (2016). Photothermal Deflection Spectroscopy. Bachelor Thesis. Heidelberg University.

[139] Becker-Koch, D. (2017). Exploring sub-bandgap states in organic and hybrid photovoltaic materials using photothermal deflection spectroscopy. Master Thesis. Heidelberg University.

[140] Sun, Q., Fassl, P., and Vaynzof, Y. (2018). Large-Scale Compositional and Electronic Inhomogeneities in CH 3 NH 3 PbI 3 Perovskites and Their Effect on Device Performance. *ACS Applied Energy Materials*, 1, 2410–2416.

[141] Mello, J. C. de, Wittmann, H. F., and Friend, R. H. (1997). An improved experimental determination of external photoluminescence quantum efficiency. *Advanced Materials*, 9, 230–232.

[142] Negele, S. (2016). Photoluminescence Quantum Efficiency of Organic-Inorganic Lead Halide Perovskite under Different Environmental Influences. Bachelor Thesis. Heidelberg University.

[143] Sevinchan, Y. (2014). Analysis of the Effects of Caesium Doping on the Properties of Zinc Oxide Layers and Inverted Hybrid Photovoltaic Devices. Bachelor Thesis. Heidelberg University.

[144] Weu, A. (2016). Identifying Degradation Mechanisms in P3HT:PCBM Organic Solar Cells. Master Thesis. Heidelberg University.

[145] Leijtens, T., Eperon, G. E., Noel, N. K., Habisreutinger, S. N., Petrozza, A., and Snaith, H. J. (2015). Stability of Metal Halide Perovskite Solar Cells. *Advanced Energy Materials*, 5, 1500963.

[146] Christians, J. A., Miranda Herrera, P. A., and Kamat, P. V. (2015). Transformation of the Excited State and Photovoltaic Efficiency of CH 3 NH 3 PbI 3 Perovskite upon Controlled Exposure to Humidified Air. *Journal of the American Chemical Society*, 137, 1530–1538.

[147] Han, Y., Meyer, S., Dkhissi, Y., Weber, K., Pringle, J. M., Bach, U., Spiccia, L., and Cheng, Y.-B. (2015). Degradation observations of encapsulated planar CH 3 NH 3 PbI 3 perovskite solar cells at high temperatures and humidity. *Journal of Materials Chemistry A*, 3, 8139–8147.

[148] Li, D., Bretschneider, S. A., Bergmann, V. W., Hermes, I. M., Mars, J., Klasen, A., Lu, H., Tremel, W., Mezger, M., Butt, H.-J., Weber, S. A. L., and Berger, R. (2016). Humidity-Induced Grain Boundaries in MAPbI 3 Perovskite Films. *The Journal of Physical Chemistry C*, 120, 6363–6368.

[149] Tong, C.-J., Geng, W., Tang, Z.-K., Yam, C.-Y., Fan, X.-L., Liu, J., Lau, W.-M., and Liu, L.-M. (2015). Uncovering the Veil of the Degradation in Perovskite CH 3 NH 3 PbI 3 upon Humidity Exposure: A First-Principles Study. *The Journal of Physical Chemistry Letters*, 6, 3289–3295.

[150] Mosconi, E., Azpiroz, J. M., and De Angelis, F. (2015). Ab Initio Molecular Dynamics Simulations of Methylammonium Lead Iodide Perovskite Degradation by Water. *Chemistry of Materials*, 27, 4885–4892.

[151] Wang, Q., Chen, B., Liu, Y., Deng, Y., Bai, Y., Dong, Q., and Huang, J. (2017). Scaling behavior of moisture-induced grain degradation in polycrystalline hybrid perovskite thin films †. *516 | Energy Environ. Sci*, 10, 516.

[152] Lin, C.-T., Pont, S., Kim, J., Du, T., Xu, S., Li, X., Bryant, D., Mclachlan, M. A., and Durrant, J. R. (2018). Passivation against oxygen and light induced degradation by the PCBM electron transport layer in planar perovskite solar cells. *Sustainable Energy & Fuels*, 2, 1686–1692.

[153] Brinkmann, K., Zhao, J., Pourdavoud, N., Becker, T., Hu, T., Olthof, S., Meerholz, K., Hoffmann, L., Gahlmann, T., Heiderhoff, R., Oszajca, M. F., Luechinger, N. A., Rogalla, D., Chen, Y., Cheng, B., and Riedl, T. (2017). Suppressed decomposition of organometal halide perovskites by impermeable electron-extraction layers in inverted solar cells. *Nature Communications*, 8, 13938.

[154] Li, J., Dong, Q., Li, N., and Wang, L. (2017). Direct Evidence of Ion Diffusion for the Silver-Electrode-Induced Thermal Degradation of Inverted Perovskite Solar Cells. *Advanced Energy Materials*, 7, 1602922.

[155] Hoke, E. T., Slotcavage, D. J., Dohner, E. R., Bowring, A. R., Karunadasa, H. I., and McGehee, M. D. (2015). Reversible photo-induced trap formation in mixed-halide hybrid perovskites for photovoltaics. *Chemical Science*, 6, 613–617.

[156] Sadhanala, A., Deschler, F., Thomas, T. H., Dutton, S. E., Goedel, K. C., Hanusch, F. C., Lai, M. L., Steiner, U., Bein, T., Docampo, P., Cahen, D., and Friend, R. H. (2014). Preparation of Single-Phase Films of CH 3 NH 3 Pb(I 1– x Br x) 3 with Sharp Optical Band Edges. *The Journal of Physical Chemistry Letters*, 5, 2501–2505.

[157] De Wolf, S., Holovsky, J., Moon, S.-J., Löper, P., Niesen, B., Ledinsky, M., Haug, F.-j., Yum, J.-h., and Ballif, C. (2014). Organometallic Halide Perovskites: Sharp Optical Absorption Edge and Its Relation to Photovoltaic Performance. *The Journal of Physical Chemistry Letters*, 5, 1035–1039.

[158] Yin, W.-J., Chen, H., Shi, T., Wei, S.-H., and Yan, Y. (2015). Origin of High Electronic Quality in Structurally Disordered CH 3 NH 3 PbI 3 and the Passivation Effect of Cl and O at Grain Boundaries. *Advanced Electronic Materials*, 1, 1500044.

[159] Urbach, F. (1953). The Long-Wavelength Edge of Photographic Sensitivity and of the Electronic Absorption of Solids. *Physical Review*, 92, 1324–1324.

[160] Sadoughi, G., Starr, D. E., Handick, E., Stranks, S. D., Gorgoi, M., Wilks, R. G., Bär, M., and Snaith, H. J. (2015). Observation and Mediation of the Presence of Metallic Lead in Organic–Inorganic Perovskite Films. *ACS Applied Materials & Interfaces*, 7, 13440–13444.

[161] Veluchamy, P. and Minoura, H. (1998). Surface analysis of anodic lead oxide films prepared in hot alkaline solutions. *Applied Surface Science*, 126, 241–245.

[162] Thomas, J. M. and Tricker, M. J. (1975). Electronic structure of the oxides of lead. Part 2.—An XPS study of bulk rhombic PbO, tetragonal PbO, β-PbO 2 and Pb 3 O 4. *J. Chem. Soc., Faraday Trans. 2*, 71, 329–336.

[163] Zhang, L. and Sit, P. H.-L. (2017). Ab initio study of the role of oxygen and excess electrons in the degradation of CH 3 NH 3 PbI 3. *Journal of Materials Chemistry A*, 5, 9042–9049.

[164] Ouyang, Y., Li, Y., Zhu, P., Li, Q., Gao, Y., Tong, J., Shi, L., Zhou, Q., Ling, C., Chen, Q., Deng, Z., Tan, H., Deng, W., and Wang, J. (2019). Photo-oxidative degradation of methylammonium lead iodide perovskite: mechanism and protection. *Journal of Materials Chemistry A*, 7, 2275–2282.

[165] Tang, X., Brandl, M., May, B., Levchuk, I., Hou, Y., Richter, M., Chen, H., Chen, S., Kahmann, S., Osvet, A., Maier, F., Steinrück, H.-P., Hock, R., Matt, G. J., and Brabec, C. J. (2016). Photoinduced degradation of methylammonium lead triiodide perovskite semiconductors. *Journal of Materials Chemistry A*, 4, 15896–15903.

[166] Prochowicz, D., Tavakoli, M. M., Solanki, A., Goh, T. W., Pandey, K., Sum, T. C., Saliba, M., and Yadav, P. (2018). Understanding the effect of chlorobenzene and isopropanol anti-solvent treatments on the recombination and interfacial charge accumulation in efficient planar perovskite solar cells. *Journal of Materials Chemistry A*, 6, 14307–14314.

[167] Tavakoli, M. M., Yadav, P., Prochowicz, D., Sponseller, M., Osherov, A., Bulović, V., and Kong, J. (2019). Controllable Perovskite Crystallization via Antisolvent Technique Using Chloride Additives for Highly Efficient Planar Perovskite Solar Cells. *Advanced Energy Materials*, 9, 1803587.

[168] Noel, N. K., Abate, A., Stranks, S. D., Parrott, E. S., Burlakov, V. M., Goriely, A., and Snaith, H. J. (2014). Enhanced Photoluminescence and So-

lar Cell Performance via Lewis Base Passivation of Organic–Inorganic Lead Halide Perovskites. *ACS Nano*, 8, 9815–9821.

[169] DeQuilettes, D. W., Vorpahl, S. M., Stranks, S. D., Nagaoka, H., Eperon, G. E., Ziffer, M. E., Snaith, H. J., and Ginger, D. S. (2015). Impact of microstructure on local carrier lifetime in perovskite solar cells. *Science*, 348, 683–686.

[170] Stewart, R. J., Grieco, C., Larsen, A. V., Doucette, G. S., and Asbury, J. B. (2016). Molecular Origins of Defects in Organohalide Perovskites and Their Influence on Charge Carrier Dynamics. *The Journal of Physical Chemistry C*, 120, 12392–12402.

[171] DeQuilettes, D. W., Koch, S., Burke, S., Paranji, R. K., Shropshire, A. J., Ziffer, M. E., and Ginger, D. S. (2016). Photoluminescence Lifetimes Exceeding 8 μs and Quantum Yields Exceeding 30% in Hybrid Perovskite Thin Films by Ligand Passivation. *ACS Energy Letters*, 1, 438–444.

[172] Wu, B., Nguyen, H. T., Ku, Z., Han, G., Giovanni, D., Mathews, N., Fan, H. J., and Sum, T. C. (2016). Discerning the Surface and Bulk Recombination Kinetics of Organic-Inorganic Halide Perovskite Single Crystals. *Advanced Energy Materials*, 6, 1600551.

[173] Munson, K. T., Grieco, C., Kennehan, E. R., Stewart, R. J., and Asbury, J. B. (2017). Time-Resolved Infrared Spectroscopy Directly Probes Free and Trapped Carriers in Organo-Halide Perovskites. *ACS Energy Letters*, 2, 651–658.

[174] Sharenko, A. and Toney, M. F. (2016). Relationships between Lead Halide Perovskite Thin-Film Fabrication, Morphology, and Performance in Solar Cells. *Journal of the American Chemical Society*, 138, 463–470.

[175] Kutes, Y., Zhou, Y., Bosse, J. L., Steffes, J., Padture, N. P., and Huey, B. D. (2016). Mapping the Photoresponse of CH 3 NH 3 PbI 3 Hybrid Perovskite Thin Films at the Nanoscale. *Nano Letters*, 16, 3434–3441.

[176] Wetzelaer, G.-J. A. H., Scheepers, M., Sempere, A. M., Momblona, C., Ávila, J., and Bolink, H. J. (2015). Trap-Assisted Non-Radiative Recombination in Organic-Inorganic Perovskite Solar Cells. *Advanced Materials*, 27, 1837–1841.

[177] Blancon, J.-C., Nie, W., Neukirch, A. J., Gupta, G., Tretiak, S., Cognet, L., Mohite, A. D., and Crochet, J. J. (2016). The Effects of Electronic Impurities and Electron-Hole Recombination Dynamics on Large-Grain Organic-Inorganic Perovskite Photovoltaic Efficiencies. *Advanced Functional Materials*, 26, 4283–4292.

[178] DeQuilettes, D. W., Zhang, W., Burlakov, V. M., Graham, D. J., Leijtens, T., Osherov, A., Bulović, V., Snaith, H. J., Ginger, D. S., and Stranks, S. D. (2016). Photo-induced halide redistribution in organic–inorganic perovskite films. *Nature Communications*, 7, 11683.

[179] Bischak, C. G., Sanehira, E. M., Precht, J. T., Luther, J. M., and Ginsberg, N. S. (2015). Heterogeneous Charge Carrier Dynamics in Organic–Inorganic Hybrid Materials: Nanoscale Lateral and Depth-Dependent Variation of Re-

combination Rates in Methylammonium Lead Halide Perovskite Thin Films. *Nano Letters*, 15, 4799–4807.

[180] Li, C., Zhong, Y., Luna, C., Unger, T., Deichsel, K., Gräser, A., Köhler, J., Köhler, A., Hildner, R., and Huettner, S. (2016). Emission Enhancement and Intermittency in Polycrystalline Organolead Halide Perovskite Films. *Molecules*, 21, 1081.

[181] Roldán-Carmona, C., Gratia, P., Zimmermann, I., Grancini, G., Gao, P., Graetzel, M., and Nazeeruddin, M. K. (2015). High efficiency methylammonium lead triiodide perovskite solar cells: the relevance of non-stoichiometric precursors. *Energy & Environmental Science*, 8, 3550–3556.

[182] Son, D.-Y., Lee, J.-W., Choi, Y. J., Jang, I.-H., Lee, S., Yoo, P. J., Shin, H., Ahn, N., Choi, M., Kim, D., and Park, N.-G. (2016). Self-formed grain boundary healing layer for highly efficient CH3NH3PbI3 perovskite solar cells. *Nature Energy*, 1, 16081.

[183] Yang, W. S., Park, B.-W., Jung, E. H., Jeon, N. J., Kim, Y. C., Lee, D. U., Shin, S. S., Seo, J., Kim, E. K., Noh, J. H., and Seok, S. I. (2017). Iodide management in formamidinium-lead-halide–based perovskite layers for efficient solar cells. *Science*, 356, 1376–1379.

[184] Green, M. A., Ho-Baillie, A., and Snaith, H. J. (2014). The emergence of perovskite solar cells. *Nature Photonics*, 8, 506–514.

[185] An, Q., Fassl, P., Hofstetter, Y. J., Becker-Koch, D., Bausch, A., Hopkinson, P. E., and Vaynzof, Y. (2017). High performance planar perovskite solar cells by ZnO electron transport layer engineering. *Nano Energy*, 39, 400–408.

[186] Xiao, Z., Dong, Q., Bi, C., Shao, Y., Yuan, Y., and Huang, J. (2014). Solvent Annealing of Perovskite-Induced Crystal Growth for Photovoltaic-Device Efficiency Enhancement. *Advanced Materials*, 26, 6503–6509.

[187] Chen, L.-C., Chen, J.-C., Chen, C.-C., and Wu, C.-G. (2015). Fabrication and Properties of High-Efficiency Perovskite/PCBM Organic Solar Cells. *Nanoscale Research Letters*, 10, 312.

[188] Hu, M., Bi, C., Yuan, Y., Bai, Y., and Huang, J. (2016). Stabilized Wide Bandgap MAPbBr x I 3- x Perovskite by Enhanced Grain Size and Improved Crystallinity. *Advanced Science*, 3, 1500301.

[189] Wang, Q., Bi, C., and Huang, J. (2015). Doped hole transport layer for efficiency enhancement in planar heterojunction organolead trihalide perovskite solar cells. *Nano Energy*, 15, 275–280.

[190] Kim, B.-S., Kim, T.-M., Choi, M.-S., Shim, H.-S., and Kim, J.-J. (2015). Fully vacuum–processed perovskite solar cells with high open circuit voltage using MoO3/NPB as hole extraction layers. *Organic Electronics*, 17, 102–106.

[191] Zhao, Y. and Zhu, K. (2014). Solution Chemistry Engineering toward High-Efficiency Perovskite Solar Cells. *The Journal of Physical Chemistry Letters*, 5, 4175–4186.

[192] Pathak, S., Sepe, A., Sadhanala, A., Deschler, F., Haghighirad, A., Sakai, N., Goedel, K. C., Stranks, S. D., Noel, N., Price, M., Hüttner, S., Hawkins, N. A., Friend, R. H., Steiner, U., and Snaith, H. J. (2015). Atmospheric

Influence upon Crystallization and Electronic Disorder and Its Impact on the Photophysical Properties of Organic–Inorganic Perovskite Solar Cells. *ACS Nano*, 9, 2311–2320.

[193] Sheikh, A. D., Bera, A., Haque, M. A., Rakhi, R. B., Gobbo, S. D., Alshareef, H. N., and Wu, T. (2015). Atmospheric effects on the photovoltaic performance of hybrid perovskite solar cells. *Solar Energy Materials and Solar Cells*, 137, 6–14.

[194] Emara, J., Schnier, T., Pourdavoud, N., Riedl, T., Meerholz, K., and Olthof, S. (2016). Impact of Film Stoichiometry on the Ionization Energy and Electronic Structure of CH 3 NH 3 PbI 3 Perovskites. *Advanced Materials*, 28, 553–559.

[195] Schulz, P., Whittaker-Brooks, L. L., MacLeod, B. A., Olson, D. C., Loo, Y.-L., and Kahn, A. (2015). Electronic Level Alignment in Inverted Organometal Perovskite Solar Cells. *Advanced Materials Interfaces*, 2, 1400532.

[196] Yang, G., Wang, C., Lei, H., Zheng, X., Qin, P., Xiong, L., Zhao, X., Yan, Y., and Fang, G. (2017). Interface engineering in planar perovskite solar cells: energy level alignment, perovskite morphology control and high performance achievement. *Journal of Materials Chemistry A*, 5, 1658–1666.

[197] Lim, K.-G., Ahn, S., Kim, Y.-H., Qi, Y., and Lee, T.-W. (2016). Universal energy level tailoring of self-organized hole extraction layers in organic solar cells and organic–inorganic hybrid perovskite solar cells. *Energy & Environmental Science*, 9, 932–939.

[198] Fakharuddin, A., Schmidt-Mende, L., Garcia-Belmonte, G., Jose, R., and Mora-Sero, I. (2017). Interfaces in Perovskite Solar Cells. *Advanced Energy Materials*, 7, 1700623.

[199] Motoki, K., Miyazawa, Y., Kobayashi, D., Ikegami, M., Miyasaka, T., Yamamoto, T., and Hirose, K. (2017). Degradation of CH 3 NH 3 PbI 3 perovskite due to soft x-ray irradiation as analyzed by an x-ray photoelectron spectroscopy time-dependent measurement method. *Journal of Applied Physics*, 121, 085501.

[200] Tosun, B. S. and Hillhouse, H. W. (2015). Enhanced Carrier Lifetimes of Pure Iodide Hybrid Perovskite via Vapor-Equilibrated Re-Growth (VERG). *The Journal of Physical Chemistry Letters*, 6, 2503–2508.

[201] Wolff, C. M., Zu, F., Paulke, A., Toro, L. P., Koch, N., and Neher, D. (2017). Reduced Interface-Mediated Recombination for High Open-Circuit Voltages in CH 3 NH 3 PbI 3 Solar Cells. *Advanced Materials*, 29, 1700159.

[202] Krogmeier, B., Staub, F., Grabowski, D., Rau, U., and Kirchartz, T. (2018). Quantitative analysis of the transient photoluminescence of CH 3 NH 3 PbI 3 /PC 61 BM heterojunctions by numerical simulations. *Sustainable Energy & Fuels*, 2, 1027–1034.

[203] Li, Y., Wang, J., Yuan, Y., Dong, X., and Wang, P. (2017). Anti-solvent dependent device performance in CH 3 NH 3 PbI 3 solar cells: the role of intermediate phase content in the as-prepared thin films. *Sustainable Energy & Fuels*, 1, 1041–1048.

[204] Bruening, K. and Tassone, C. J. (2018). Antisolvent processing of lead halide perovskite thin films studied by in situ X-ray diffraction. *Journal of Materials Chemistry A*, 6, 18865–18870.

[205] Philippe, B., Saliba, M., Correa-Baena, J.-P., Cappel, U. B., Turren-Cruz, S.-H., Grätzel, M., Hagfeldt, A., and Rensmo, H. (2017). Chemical Distribution of Multiple Cation (Rb + , Cs + , MA + , and FA +) Perovskite Materials by Photoelectron Spectroscopy. *Chemistry of Materials*, 29, 3589–3596.

[206] Jiang, Q., Chu, Z., Wang, P., Yang, X., Liu, H., Wang, Y., Yin, Z., Wu, J., Zhang, X., and You, J. (2017). Planar-Structure Perovskite Solar Cells with Efficiency beyond 21%. *Advanced Materials*, 29, 1703852.

[207] Awtrey, A. D. and Connick, R. E. (1951). The Absorption Spectra of I 2 , I 3 - , I - , IO 3 - , S 4 O 6 = and S 2 O 3 = . Heat of the Reaction I 3 - = I 2 + I -. *Journal of the American Chemical Society*, 73, 1842–1843.

List of my Publications

Main Publications:

[1] Q. Sun*, P. Fassl*, D. Becker-Koch, A. Bausch, B. Rivkin, S. Bai, P. E. Hopkinson, H. J. Snaith, Y. Vaynzof, Adv. Energy Mater. 2017, 7, 1700977. *These authors contributed equally.

[2] Q. Sun, P. Fassl, Y. Vaynzof, ACS Appl. Energy Mater. 2018, 1, 2410.

[3] Q. Sun*, A. D. Taylor*, F. Paulus, Y. Vaynzof. Under preparation. *These authors contributed equally.

Additional Publications:

[1] B. Rivkin, P. Fassl, Q. Sun, A. D. Taylor, Z. Chen, Y. Vaynzof, ACS Omega 2018, 3, 10042.

[2] Q. An, Q. Sun, A. Weu, D. Becker-Koch, F. Paulus, S. Arndt, F. Stuck, A. S. K. Hashmi, N. Tessler, Y. Vaynzof, Adv. Energy Mater. 2019, 1901257.

[3] Z. Li, A. Ottmann, Q. Sun, A. K. Kast, K. Wang, T. Zhang, H.-P. Meyer, C. Backes, C. Kübel, R. R. Schröder, J. Xiang, Y. Vaynzof, R. Klingeler, J. Mater. Chem. A 2019, 7, 7553.

[4] Z. Li, A. Ottmann, E. Thauer, C. Neef, H. Sai, Q. Sun, K. Cendrowski, H.-P. Meyer, Y. Vaynzof, E. Mijowska, J. Xiang, R. Klingeler, RSC Adv. 2016, 6, 76084.

[5] Z. Li, A. Ottmann, T. Zhang, Q. Sun, H.-P. Meyer, Y. Vaynzof, J. Xiang, R. Klingeler, J. Mater. Chem. A 2017, 5, 3987.

[6] H. Eggers, F. Schackmar, T. Abzieher, Q. Sun, U. Lemmer, Y. Vaynzof, B. S. Richards, G. Hernandez-Sosa, U. Paetzold, Adv. Energy Mater. Submitted.

[7] M. A. Siguan, D. Becker-Koch, A. D. Taylor, Q. Sun, V. Lami, P. G. Oppenheimer, F. Paulus, Y. Vaynzof, ACS Nano. Submitted.

[8] J. F. Butscher, Q. Sun, Y. Wu, F. Stuck, M. Hoffmann, A. Dreuw, A. S. K. Hashmi, N. Tessler, Y. Vaynzof, JPhys Materials. Under preparation.

Acknowledgements

I would first like to thank my supervisor, Prof. Dr. Yana Vaynzof. Thank you for your invaluable guidance and advices, for all the opportunities I was given to conduct my researches and continuous support throughout my work and writing of the thesis.

I would like to thank Prof. Dr. Giulia Grancini for being my second referee, for the time you spend reading my thesis and for the effort you take to come to Heidelberg for my oral exam.

I would like to express my gratitude to Prof. Dr. Annemarie Pucci and Prof. Dr. Ulrich Schwarz for being my examiners of the oral exam.

I would like to thank Prof. Dr. Uwe Bunz for providing access to the device fabrication facilities. I am also grateful to Prof. Dr. Annemarie Pucci and Prof. Dr. Rasmus Schröder for the access to AFM and SEM, respectively. I would like to thank Prof. Dr. Jana Zaumseil for the acess to AFM and SEM.

I am very grateful to the financial support by HGSFP for covering most of the travel expenses of international conferences and the bridging funding.

I am very happy to spend four years with my colleagues in the AG Vaynzof group. I want to thank Dr. Paul Hopkinson for his excellent advices and for setting up lab facilities at the beginning of my PhD. I would like to thank Dr. Paul Fassl and Dr. Fabian Paulus for the SEM measurements, David Becker-Koch and Alexandra Bausch for measuring PDS, and Dr. Fabian Paulus again for the XRD measurements. I would particularly like to thank Dr. Alex Taylor. Thank you for your excellent ideas, for the wonderful collaborations, and especially for your time and effort proofreading and correcting my thesis. I would also like to thank Qingzhi An. I appreciate your support for giving your helpful hand whenever perovskite behaves abnormally. I am grateful to all group members. Thank you for the great time and pleasant working atmosphere.

I would like to thank all my friends, here and back in China, for lending a sympathetic ear when I need it.

I would like to thank my parents for being supportive throughout my whole study. Thank you for believing in me, and for your patience and encouragement.

Finally, I want to thank my boyfriend, David, for always being there for me.